Politecnico di Torino

Master's Degree in Aerospace Engineering

Academic Year 2025/2026

Graduation session March/April 2026

Multi-Body Dynamic Modeling and Robust Sliding Mode Control of Flexible Satellites

Supervisors

Mauro Mancini, Politecnico di Torino

Francesco Sanfedino, Isae-Supaero

Candidate

Pietro Colletti

Ringraziamenti

Sono trascorsi cinque anni lunghi e intensi, volati via così in fretta che quasi non me ne sono reso conto. In questi anni sono successe innumerevoli cose. Ho vissuto momenti fantastici, mi sono appassionato sempre di più a ciò che studiavo, lezione dopo lezione, e ho incontrato docenti il cui impegno è stato fondamentale per la mia crescita accademica e professionale.

Il mio primo pensiero va alla Prof.ssa Battipede, per i preziosi consigli che mi ha saputo dare. Vorrei poi ringraziare di cuore la Prof.ssa Elisa Capello, fondamentale per avermi messo in contatto con il Prof. Mauro Mancini. A quest'ultimo, diventato il mio relatore, va un ringraziamento speciale per avermi concesso la possibilità di svolgere il lavoro di tesi all'estero, un'esperienza che desideravo profondamente e che ha avuto per me un valore formativo inestimabile. Un ringraziamento anche al Prof. Francesco Sanfedino e a Umberto Zucchelli, per avermi seguito durante il progetto in Francia. Umberto, in particolare, è stato un punto di riferimento straordinario, dall'inizio alla fine del percorso; spero un giorno, se dovessi trovarmi al suo posto, di sapermi comportare esattamente come lui ha fatto con me.

Un pensiero affettuoso va ai compagni conosciuti in questo lungo viaggio, che hanno reso più dolce la vita universitaria. Grazie a Federico C., Alessio e ai ragazzi della "prima fila": Flavio, Michele e Lorenzo G. Un grande abbraccio a Umberto C., Umberto G., Sara, Matteo, Luca, Gabriele, Lorenzo A. e Lorenzo Crippa. Quest'ultimo, in particolare, è molto più di un collega ed è stata una delle presenze che più mi è mancata durante i miei mesi a Tolosa. Grazie anche ad Alessandra, Simone, Angelo, Bruna, Ferdi e Sara per il bellissimo gruppo che abbiamo creato e i momenti trascorsi insieme. Grazie ai ragazzi del Team Icarus per i bei pomeriggi trascorsi a costruire il velivolo, tra analisi FEM e intense pause caffè. Grazie ai ragazzi di Tolosa, in particolare Gabriele, Davide, Lorenzo e Tommaso. Senza di voi, questa esperienza non sarebbe stata la stessa.

Un ringraziamento anche a Edoardo e a Marta, che conosco fin dai tempi della scuola materna, con i quali ho intrapreso lo stesso cammino, inseguendo le passioni che ci accomunano.

Grazie a Fede, Rick, Vitto, Nico, Betta e Anto. Nonostante i nostri interessi siano così diversi, siete stati sempre pronti a supportarmi e la mia valvola di sfogo quando i ritmi dell'università diventavano troppo pesanti. Avervi accanto nel mio tempo libero e sapere di poter contare sul vostro ascolto nei miei 'momenti no' è stato un dono immenso.

Infine, vorrei ringraziare Mauro, Matteo, Daniela e Sergio per il supporto e per la loro presenza durante questi anni. Ringrazio Roby e Ale per i preziosi consigli dispensati durante quest'ultimo anno molto intenso. Ringrazio Papà. So bene quanto tu sia fiero del mio percorso di studi e ho sempre percepito la tua fiducia. Ringrazio Mamma. Il tuo modo di fare, la tua infinita disponibilità verso le altre persone, la tua caparbietà e il tuo spirito di sacrificio mi hanno guidato durante questi anni. Mi hai insegnato che bisogna sempre dire cosa si pensa e fare ciò che si vuole, e questi sono gli insegnamenti che porterò per sempre con me.

Grazie, Sofi, per essere stata al mio fianco durante l'ultimo anno. La tua presenza costante è stata per me un rifugio sicuro nei mesi trascorsi in Francia, mentre la tua gentilezza, i tuoi modi di fare e il tuo impegno instancabile sono una continua fonte di ispirazione. Scrivere questa tesi non sarebbe stata la stessa cosa senza la tua compagnia, ed è bellissimo poter condividere questo traguardo proprio con te.

Questo mio piccolo ma tanto desiderato traguardo, lo dedico a voi.

Acknowledgements

Five long and intense years have passed, flying by so quickly that I barely even noticed. Countless things have happened during these years. I have experienced fantastic moments, I grew increasingly passionate about what I was studying, lecture after lecture, and I met professors whose dedication was fundamental to my academic and professional growth.

My first thought goes to Prof. Battipede, for the invaluable advice she was able to give me. I would then like to sincerely thank Prof. Elisa Capello, who was instrumental in putting me in touch with Prof. Mauro Mancini. To the latter, who became my thesis supervisor, goes a special thanks for granting me the opportunity to carry out my thesis work abroad—an experience I deeply desired and which has had an inestimable educational value for me. A thank you also to Prof. Francesco Sanfedino and Umberto Zucchelli for guiding me during the project in France. Umberto, in particular, was an extraordinary point of reference from the beginning to the end of the journey; I hope one day, if I were to find myself in his position, to be able to conduct myself exactly as he did with me.

A fond thought goes to the classmates I met on this long journey, who made university life sweeter. Thank you to Federico C., Alessio, and the guys from the "front row": Flavio, Michele, and Lorenzo G. A big hug to Umberto C., Umberto G., Sara, Matteo, Luca, Gabriele, Lorenzo A., and Lorenzo Crippa. The latter, in particular, is much more than a colleague and was one of the presences I missed the most during my months in Toulouse. Thanks also to Alessandra, Simone, Angelo, Bruna, Ferdi, and Sara for the wonderful group we created and the moments we spent together. Thank you to the guys from Team Icarus for the beautiful afternoons spent building the aircraft, between FEM analyses and intense coffee breaks. Thank you to the guys from Toulouse, in particular Gabriele, Davide, Lorenzo, and Tommaso. Without you, this experience would not have been the same.

A thank you also to Edoardo and Marta, whom I have known since I was a child, with whom I embarked on the same path, pursuing the passions that unite us.

Thank you to Fede, Rick, Vitto, Nico, Betta, and Anto. Even though our interests are so different, you were always ready to support me and served as my much-needed escape when the pace of university became too overwhelming. Having you by my side in my free time and knowing I could count on you to listen during my hard times has been an immense gift.

Finally, I would like to thank Mauro, Matteo, Daniela, and Sergio for their support and their presence over these years. I thank Roby and Ale for the invaluable advice they gave me during this last, very intense year. Thank you, Dad. I know well how proud you are of my academic journey, and I have always felt your belief in me. Thank you, Mom. Your way of doing things, your infinite willingness to help others, your tenacity, and your spirit of sacrifice have guided me throughout these years. You taught me that one must always speak their mind and do what they want, and these are the lessons I will carry with me forever.

Thank you, Sofi, for being by my side during this last year. Your constant presence was a safe haven for me during the months spent in France, while your kindness, your warm demeanor, and your tireless dedication are a continuous source of inspiration. Writing this thesis would not have been the same without your company, and it is beautiful to be able to share this milestone with you.

I dedicate this small but long-awaited milestone of mine to you.

Abstract

The evolution of space missions toward large, low-mass platforms has made the interaction between the attitude control system and structural dynamics —commonly referred to as Control-Structure Interaction (CSI)— a critical issue during the design phase. Although control law synthesis typically relies on rigid-body models, performance validation based solely on such assumptions is insufficient to capture potential instability risks and pointing degradation arising from structural flexibility.

The first contribution of this work focuses on the development and validation of a non-linear, fully parametric multi-body dynamic model capable of accurately representing the coupling between a rigid central hub and flexible appendages. Open-loop validation confirms the physical consistency of the proposed model, which proves to be a versatile and reliable tool for the preliminary analysis of different mission configurations.

The second contribution introduces a methodological framework for the synthesis of a Robust Adaptive Sliding Mode Control law, specifically conceived to operate in the presence of significant parametric uncertainties, external disturbances, and stringent actuation constraints. Rather than aiming at a unique or definitive control solution, the proposed approach provides a flexible parametric architecture suitable for systematically exploring the coupled dynamics of the system.

Finally, the validation of the overall framework is carried out through a multi-phase numerical simulation campaign. Starting from verification on the nominal model, the analysis is progressively extended to include external disturbances, structural parameter uncertainties, and different operational scenarios characterized by varying initial conditions. The results allow for quantifying the impact of Control-Structure Interaction on dynamic performance and for identifying stability boundaries, thereby offering useful guidelines for the preliminary design of future space missions.

Contents

Abstract **vi**

List of Figures **xvi**

List of Tables **xvii**

List of Acronyms **xix**

1 Introduction **1**

1.1 Context and motivations 1

1.2 Research Objectives and Methodology 3

1.3 Thesis Outline 4

2 Mathematical Model of the Flexible Satellite **5**

2.1 Model Architecture and Assumptions 6

2.1.1 Definition of Reference Frames 7

2.1.2 System State Definition 8

2.1.3 Model Assumptions and Limitations 8

2.2 Characterization of the Model Components 9

2.2.1 Rigid Hub 9

2.2.2 Flexible Appendages 10

2.2.3 Elastic and Dissipative Interface 12

2.3 Derivation of the Equations of Motion 16

2.3.1 Kinematics of the System Components 17

2.3.1.1 Hub Kinematics 18

2.3.1.2 Kinematics of the Flexible Appendages 19

2.3.2 Energy Analysis of the System 20
2.3.2.1 Total Kinetic Energy (T) 20
2.3.2.2 Elastic Potential Energy (U) 21
2.3.2.3 Rayleigh Dissipation Function (D) 21
2.3.3 Analytical Derivation of the Equation Terms 22
2.3.4 Final Model Formulation 24

3 Case Study Definition and Model Validation 27
3.1 Definition of the Nominal Case Study 27
3.1.1 Central Hub Characteristics 28
3.1.2 Flexible Appendages Characteristics 28
3.1.3 Coupled Model Characteristics 29
3.2 Modal Analysis of the Coupled System 31
3.2.1 Foundations of Modal Analysis 31
3.2.2 Modal Analysis Results 33
3.3 Open-Loop Dynamic Validation 38
3.3.1 Simulation Setup 39
3.3.2 Results Analysis 41

4 Control Law Synthesis 53
4.1 Fundamentals of Sliding Mode Control 53
4.2 Adaptive Sliding Mode Control Law 55
4.2.1 Definition of Attitude Error 55
4.2.2 Sliding Surface Design 56
4.2.3 Dynamics and Control Law 56
4.2.4 Lyapunov Stability Analysis 58
4.2.5 Budget Allocation Algorithm 59

5 Numerical Simulations and Results Analysis 63

5.1 Validation of the Control Law on the Nominal Case Study 63

5.1.1 Simulation Setup 63

5.1.2 Closed-Loop Model 66

5.1.3 Simulation Results Analysis 69

5.2 Robustness Validation against Parametric Uncertainties 82

5.2.1 Sensitivity Analysis on Individual Uncertain Parameters 83

5.2.2 Monte Carlo Analysis on All Uncertain Parameters 97

5.3 Robustness validation against changes in the operational scenario 102

6 Conclusions and Future Perspectives 111

6.1 Critical review of the work and results obtained 111

6.2 Recommendations for future research 113

A Explanation and Execution Guide for MATLAB Scripts 115

A.1 Symbolic Derivation of the Equations of Motion 115

A.2 Model Setup, Tuning, and Modal Analysis 117

A.3 Open-Loop Non-Linear Simulation 119

A.4 Symbolic Derivation of the Rigid Synthesis Model 121

A.5 Closed-Loop Non-Linear Simulation 123

B Complete matrices 127

B.1 Mass matrix of the nominal case study 127

Bibliography 129

List of Figures

2.1 Main view of the coupled system, composed of the rigid Hub and the two flexible appendages: definition of the reference frames, state variables of the main rigid body, elastic deformation variables, and topological configuration. (Note: This figure depicts the coupled system in a generic deformed configuration). . 7

2.2 Geometric representation of the rigid Hub with the main geometric dimensions and definition of the mounting vectors. 10

2.3 Geometric representation of the rigid panel in the undeformed (dashed line) and deformed configurations, along with the main geometric dimensions and reference frames. Representation of the flexible joint, the element where all elasticity is lumped, shown in dark green in the drawing. The combination of the rigid panel and the elastic joint constitutes the flexible appendage. 11

2.4 Block diagram of the dynamic couplings of the Hub-Panels system (Dynamic Coupling). 25

3.1 Geometric representation of the nominal case study. The principal axes are shown in red, the body axes in black, and the alignment of the frames in the initial undeformed configuration is visible, with $\alpha_{sadm} = 0°$. 30

3.2 Modal Interaction Map. The matrix highlights how the flexible modes (from 7 to 18) do not solely involve the panel coordinates, but also excite the degrees of freedom of the Hub. 37

3.3 Block diagram of the Open-Loop simulation. The nominal torque profile is applied directly to the non-linear dynamic model to evaluate the free and forced response. 40

3.4 Time profile of the commanded external torque ($\boldsymbol{\tau}_{cmd}$) in Open-Loop. The impulse exclusively excites the yaw axis. 41

3.5 Time evolution of Euler angles. Discontinuities at ±180° are due to wrapping. 42

3.6 Time evolution of the quaternion. Only the q_0 and q_3 components relative to the Z-axis are active. 42

3.7 Time evolution of the angular velocities ($\boldsymbol{\omega}$). A linear macro-dynamic is noted, upon which an oscillatory *ripple* induced by the flexible panels is superimposed. 43

3.8 Time evolution of the angular accelerations ($\dot{\boldsymbol{\omega}}$). The violent vibrations highlight the direct exchange of reactive torques between the appendages and the Hub. 43

3.9 Time evolution of the modal coordinates in the local panel frame. The graphs on the left represent respectively the translational (top) and rotational (bottom) degrees of freedom of Panel 1. The right column relates to the degrees of freedom of Panel 2. 45

3.10 Linear displacement of the panel extremities (*Tip Displacement*). The top graph refers to Panel 1, the bottom graph refers to Panel 2. The in-plane deflection does not exceed one centimeter during the maneuver. 46

3.11 Analysis of the interaction torques. Left: the elastic reaction torques transferred from the panels to the Hub ($\boldsymbol{\tau}_{flex}$). Right: comparison between the ideal command ($\boldsymbol{\tau}_{cmd}$) and the net torque actually responsible for the central body's acceleration ($\boldsymbol{\tau}_{net}$). 47

3.12 Verification of the angular momentum in body axes. The system accumulates exactly 10 Nms on the Z-axis, conserving them indefinitely in the absence of external torques. The transient ripple is a symptom of the inertial exchange with the flexible degrees of freedom. 49

3.13 Detailed energy balance. (1) Macroscopic conservation of the total mechanical energy. (2) Microscopic dynamics of the elastic energy and its progressive structural dissipation. (3) Verification of the perfect exponential decay of the vibratory energy on a logarithmic scale. 50

3.14 Spectrogram of the dynamic signals. The frequency is reported on the ordinate, the time on the abscissa, while the color maps the Power Spectral Density on a logarithmic scale (dB). The dynamics are confined to the yaw axis, with a clear resonance at ≈ 1.23 Hz. 51

4.1 Phase plane representation of the evolution of the system under SMC action. The state trajectories (in red) converge towards the Sliding Surface (blue line) during the Reaching Phase, and then slide towards the origin during the Sliding Phase. 54

4.2 Admissible allocation space (green area) for the control parameters at a generic time instant t. The ordinate axis represents the allocated robust torque (**JK**), while the abscissa axis represents the kinematic parameter Λ. The space of valid solutions is lower-bounded by the disturbance robustness requirement ($\tau_{dist} + \eta$) and upper-bounded by the available residual budget line, beyond which the system would enter saturation. 61

5.1 Logical architecture of the Closed-Loop simulator. The diagram illustrates the signal flow between the ASMC control algorithm, the disturbance modeling, the mapping of the forcing terms and the state vector, and the integration of the non-linear multi-body dynamics. 67

5.2 Time evolution of the Euler angles. 70

5.3 Time evolution of the quaternion. 70

5.4 Accuracy and pointing stability analysis on a logarithmic scale. The upper graph shows the decay of the total attitude error with respect to the 45° target, while the lower graph illustrates the damping of the angular velocities (jitter). Both quantities settle stably below their respective tolerance thresholds (**R1** $< 0.05°$, **R2** $< 10^{-3}$ deg/s), highlighted by the green bands. 71

5.5 State trajectory in the phase plane. The initial and final trajectory of the Sliding Surface, the thickness of the Boundary Layer, the initial gray band ($\Lambda_{nom} = 0.2$), and the final green band ($\Lambda_{max} = 5.0$) are visible. The trajectory (colored line) is smoothly guided towards the origin (target reached). 71

5.6 Time evolution of the angular velocities ($\boldsymbol{\omega}$). 72

5.7 Time evolution of the angular accelerations ($\dot{\boldsymbol{\omega}}$). 72

5.8 Time evolution of the Sliding Variables s. The trajectories cancel out the large initial misalignment, enter within the Boundary Layer $\pm\Phi$, and converge asymptotically. Around 30 s, a phenomenon related to a gradual change in the slope of the Sliding Surface towards the value Λ_{max} is observed. The faster convergence of the Sliding Variable to zero is noted. 73

5.9 Evolution of the adaptive parameters: smooth transition of the parameter Λ_{act} (top) and directional allocation of the robust gain $J \cdot K$ (bottom). The shaded area represents the impassable operational safety limit below which the robustness and stability of the method are not guaranteed. 74

5.10 Analysis of the disturbance torques acting on the Hub: propellant Sloshing effects proportional to the applied torque, environmental disturbances, and proportional actuator gain uncertainties. 75

5.11 Time profile of the global control effort. The maneuver requires a high initial torque to overcome the system's inertia, which subsequently settles to a lower value without ever violating the physical or operational limits of the actuators. It is noted that the torque actually delivered to the Plant differs slightly from the commanded torque. The small difference is attributable to the disturbance torques, which are of a lower order of magnitude compared to the represented scale. 76

5.12 Analytical breakdown of the control law. It highlights the load distribution among the component related to dynamic cancellation, the gyroscopic compensation, and the robust action during transients. 77

5.13 Evolution of the flexible modal coordinates (η). The translational deformations (top) are numerically negligible, while the rotational deformations (bottom) exhibit limited and well-damped transient oscillations. The graphs on the left represent the degrees of freedom of Panel 1. The graphs on the right represent the degrees of freedom of Panel 2. 79

5.14 Linear displacement at the tips of the solar panels (Tip Displacement). The top graph refers to Panel 1, while the bottom graph refers to Panel 2. 79

5.15 Control-Structure Interaction (CSI). On the left, the impulsive disturbance torques generated by the solar panels' flexion (τ_{flex}) are represented. On the right, a comparison is shown between the torque input to the flexible Plant (τ_{app}) and the actual net torque experienced by the Hub (τ_{net}). 80

5.16 System energy balance. The total mechanical energy decays asymptotically (top). The elastic energy (middle and bottom on a logarithmic scale) is entirely dissipated. 81

5.17 Pointing accuracy and stability analysis on a logarithmic scale. The upper graph shows the decay of the total attitude error relative to the 45° target, while the lower graph illustrates the damping of angular velocities (jitter). Both quantities settle stably below their respective tolerance thresholds (**R1** $< 0.05°$, **R2** $< 10^{-3}$ deg/s) highlighted by the green bands. A small difference is noted between the blue curve (Nominal Case) and the green one (Undamped Case). 85

5.18 System energy balance. Total mechanical energy decays asymptotically (top). Elastic energy (middle and bottom on a logarithmic scale) dissipates over time without excitation of flexible dynamics. The blue curve represents the nominal case, while the green curve represents the undamped case. 86

5.19 Linear displacement at the ends of the solar panels (Tip Displacement). The graph refers to Panel 1. 88

5.20 Time profile of the global control effort. The maneuver requires a high initial torque to overcome the system's inertia. Subsequently, it settles to a lower value without ever violating the physical or operational limits of the actuators. The control torques exhibit different frequency content. 89

5.21 System energy balance. Total mechanical energy decays asymptotically (top). Elastic energy (middle and bottom on a logarithmic scale) dissipates over time without excitation of flexible dynamics. 90

5.22 Pointing accuracy and stability analysis on a logarithmic scale. The upper graph shows the decay of the total attitude error relative to the 45° target, while the lower graph illustrates the damping of the angular velocities (jitter). 91

5.23 System energy balance. Total mechanical energy decays asymptotically (top). Elastic energy (middle and bottom on a logarithmic scale) dissipates over time without excitation of flexible dynamics. Note the different magnitude of the total mechanical energy peak. 93

5.24 Pointing accuracy and stability analysis on a logarithmic scale. The upper graph shows the decay of the total attitude error relative to the 45° target, while the lower graph illustrates the damping of angular velocities (jitter). . . 94

5.25 Control-Structure Interaction (CSI). The impulsive disturbance torque (τ_{flex}) generated by the deflection of the solar panel is represented for different panel inertia values. 95

5.26 Linear displacement at the ends of the solar panels (Tip Displacement). The graph refers to Panel 1. 96

5.27 Pointing accuracy and stability analysis on a logarithmic scale. The top graph shows the decay of the total attitude error relative to the 45° target, while the graph at the bottom illustrates the damping of the angular velocities (jitter). 96

5.28 Pointing accuracy and stability analysis on a logarithmic scale. The top graph shows the decay of the total attitude error relative to the 45° target, while the graph at the bottom illustrates the damping of the angular velocities (jitter). 98

5.29 Pointing accuracy and stability analysis on a logarithmic scale. The upper graph shows the decay of the total attitude error relative to the 45° target, while the lower graph illustrates the damping of the angular velocities (jitter). 99

5.30 Linear displacement at the ends of the solar panels (Tip Displacement). The graph refers to Panel 1. 99

5.31 Time profile of the global control effort. 100

5.32 System energy balance. Total mechanical energy decays asymptotically (top). Elastic energy (middle and bottom on a logarithmic scale) dissipates over time without critical excitation of flexible dynamics. 101

5.33 Evolution of adaptive parameters: smooth transition of the parameter Λ_{act} (top) and directional allocation of the robust gain $J \cdot K$ (bottom). The shaded area represents the impassable operational safety limit, below which the robustness and stability of the method are no longer guaranteed. 102

5.34 Time evolution of the Euler angles. 103

5.35 Time evolution of the angular velocities $\boldsymbol{\omega}$. 103

5.36 Pointing accuracy and stability analysis on a logarithmic scale. The upper graph shows the decay of the total attitude error relative to the 45° target, while the lower graph illustrates the damping of the angular velocities (jitter). 104

5.37 Flexible torques $\boldsymbol{\tau}_{flex}$ exchanged between the Hub and the flexible appendages over time. 105

5.38 System energy balance. Total mechanical energy decays asymptotically (top). Elastic energy (middle and bottom on a logarithmic scale) persists over time due to the strong CSI interaction. 106

5.39 Time profile of the torque $\boldsymbol{\tau}_{app}$ applied to the flexible Plant. 107

5.40 Time evolution of the sliding variables s. The trajectories nullify the large initial misalignment but enter the Boundary Layer $\pm\Phi$ at different times and following different trajectories. 108

5.41 Evolution of adaptive parameters: smooth transition of the parameter Λ_{act} (top) and directional allocation of the robust gain $J \cdot K$ (bottom). The shaded area represents the impassable operational safety limit below which the robustness and stability of the method are not guaranteed. 109

5.42 Linear displacement at the ends of the solar panels (Tip Displacement). The graph refers to Panel 1. 109

A.1 Logical flowchart of the `N01_Derive_Satellite_Equations.m` script for the symbolic generation of the dynamic model. 116

A.2 Logical flowchart of the `N02_Step1_CompleteModel_Setup.m` script for the symbolic generation of the dynamic model. 118

A.3 Logical flowchart of the `N05_OpenLoop_FlexModel.m` script for the dynamic simulation. 120

A.4 Logical flowchart of the `N04_Derive_Rigid_Design_Model.m` script for the symbolic generation of the rigid body dynamic model. 122

A.5 Logical flowchart of the `N08_CL_FlexPlant_Disturbi_BASE.m` script for the dynamic simulation. 124

List of Tables

3.1 Physical and modal parameters of the nominal case study. 28

3.2 Classification of the predicted target mode shapes for the isolated panel. . . . 34

3.3 Classification of the mode shapes of the coupled satellite system. 35

List of Acronyms

ACS	*Attitude Control System*
ADCS	*Attitude Determination Control System*
ADR	*Active Debris Removal*
ASMC	*Adaptive Sliding Mode Control*
CSI	*Control-Structure Interaction*
DOF	*Degrees Of Freedom*
ESA	*European Space Agency*
FEM	*Finite Element Method*
FS	*Flexible Spacecraft*
GNC	*Guide Navigation and Control*
HITL	*Hardware-In-The-Loop*
HOSMC	*Higher-Order Sliding Mode Control*
HSMC	*Hybrid Sliding Mode Control*
ISMC	*Integral Sliding Mode Control*
LASM	*Large Angle Slew Maneuvers*
LEO	*Low Earth Orbit*
LPA	*Lumped Parameter Approach*
LSS	*Large Space Structures*
MBS	*Multi Body System*
OOS	*On-orbit Servicing*
PSD	*Power Spectral Density*
PZT	*Piezoelectric*
RW	*Reaction Wheel*
SADM	*Single Axis Drive Mechanism*
SITL	*Software-In-The-Loop*

SMC *Sliding Mode Control*

STFT *Short-Time Fourier Transform*

STSMC *Super Twisting Sliding Mode Control*

VSC *Variable Structure Control*

Chapter 1

Introduction

Contents

1.1 Context and motivations 1
1.2 Research Objectives and Methodology 3
1.3 Thesis Outline 4

1.1 Context and motivations

The modern aerospace industry is driven by a continuous pursuit of efficiency and versatility, which translates into the need to reduce launch costs while increasing the operational capabilities of space platforms. On the one hand, the development of Large Space Structures (LSS) is gaining momentum: large-scale, low-mass satellites characterized by the extensive use of composite materials and large deployable appendages (such as solar arrays for electric propulsion or high-gain antennas), where structural flexibility becomes the dominant dynamic feature. On the other hand, there is the emergence of On-Orbit Servicing (OOS) and Active Debris Removal (ADR) missions, which involve the use of platforms equipped with robotic manipulator arms. In this scenario, the satellite is no longer a passive observer, but a dynamic actor: the movement of the robotic arm for capture or repair operations generates strong reaction torques on the central body (Dynamic Coupling), acting as an internal disturbance that can trigger strong nonlinear behaviors, excite structural vibrations, and destabilize the attitude during the most critical phases of the operation.

In both cases, the structure exhibits low-frequency vibration modes, often overlapping with the bandwidth of the Attitude Determination and Control System (ADCS). This makes the rigid-body assumption an insufficient and potentially dangerous approximation for the stability of the entire dynamic system. The inclusion of flexibility transforms the control problem into a multi variable challenge subject to strong structured uncertainties. Critical parameters such as the inertia matrix and the eigenvalues of the elastic system are not constant but evolve dynamically depending on the operational scenario (e.g., geometry variations due to robotic maneuvers or deployments). Consequently, any nominal model used for the synthesis of the control law will be affected by a variable modeling error compared to the real system.

In this context, it becomes necessary to adopt a robust control perspective, where the flexible dynamics are interpreted as a bounded perturbation or an unmodeled disturbance

acting on the Rigid Body Plant. The goal of the synthesis is to ensure that the controlled rigid body system remains stable and capable of meeting performance requirements even in the presence of these dynamic perturbations and the associated parametric uncertainties.

State of the Art: Modeling and Control Strategies. The scientific community tackles the Control-Structure interaction problem (CSI) by employing various strategies. Regarding modeling and control, recent works such as [Rod+24] and the ESA project [Pas+] study the behavior of continuously spinning satellites equipped with extremely long flexible booms to obtain Earth's magnetic field measurements. Specifically, their work focuses on vibration control once the desired attitude has been reached. The former [Rod+24], emphasizes high-fidelity modeling to capture complex phenomena such as centrifugal stiffening, aiming to push the control system to its performance limits. The latter, [Pas+], proposes a robust linear control system (H_∞, μ-synthesis) to actively dampen the oscillations of the flexible appendages.

Other authors [Nad+19] focus on active vibration control through the use of piezoelectric actuators (PZT) attached to flexible appendages, while others [Gao+21] investigate CSI during aggressive rotational maneuvers, known as Large Angle Slew Maneuvers (LASM), for reference trajectory tracking. Although all these authors propose control laws to manage the flexible satellite, only a few introduce their own dynamic model of the Multi-Body System (MBS) featuring flexible appendages.

The majority of researchers utilize Sliding Mode Control (SMC) techniques to analyze the satellite's behavior and ensure its stabilization throughout the execution of the maneuver. Some authors investigated Hybrid Sliding Mode Control strategies (HSMC) to stabilize nonlinear dynamics through the SMC technique while improving disturbance rejection and vibration suppression capabilities using the H_∞ approach [KM20]. Additionally, Super Twisting Sliding Mode Control techniques (STSMC) have been proposed [Nad+19] to achieve faster transient responses and improve the steady-state behavior of the system. Finally, SMC techniques with adaptive parameters have also been explored [Lah+23].

Some authors compare the SMC technique with the H_∞ approach to controlling a robotic manipulator mounted on an oscillating platform [KJ17]. In this scenario, the challenge is to control the position of the manipulator's end-effector and maintain the attitude between the two links of the robotic arm in the presence of an oscillating base. The authors report that the SMC technique is more effective in achieving the intended goal compared to the H_∞ technique. The mathematical model and the control law presented in the cited paper can be easily extended to space robotics in OOS applications.

Genesis of the Thesis Work: An Investigative Path. The selection of the topic for this thesis work is the result of a critical analysis of various operational scenarios, which were evaluated during the preliminary research phase to identify the best compromise between scientific relevance and engineering feasibility. Several different thematic paths were considered:

1. **Spinning Satellites with Flexible Appendages**: Inspired by recent literature, the stabilization of rotating platforms was evaluated. Although this topic is of great scientific interest, it primarily focuses on steady-state attitude maintenance, making it less suitable for investigating nonlinear transient dynamics.

2. **On-Orbit Servicing and Robotic Manipulation**: The scenario of a Chaser satellite using a robotic arm to capture space debris or service a target was analyzed. This scenario represents the extreme case of dynamic interaction: the arm acts as a flexible appendage that changes its configuration over time. However, the additional complexity associated with the manipulator's kinematics and contact dynamics would have shifted the research focus toward guidance trajectory optimization (Path Planning and Inverse Kinematic Optimization) aimed at minimizing base reactions. Therefore, it was decided to test the SMC control law in a simplified scenario to isolate the physical phenomenon of interest: the Control-Structure Interaction in the presence of low-frequency flexible modes.

3. **Rapid Pointing Maneuvers (LASM)**: Finally, the focus was on rapid reorientation maneuvers and trajectory tracking of a flexible satellite. This scenario represents the worst-case for ADCS and the perfect setting to study CSI: it requires high control torques (inducing the risk of actuator saturation) and fast attitude changes (leading to mode excitation), making it the ideal testbed for assessing stability limits. Furthermore, the ability to perform rapid reorientation maneuvers while ensuring stable pointing in short time is a key cross-cutting capability: it is essential both to maximize the accuracy and the number of acquisitions in Earth observation missions and to provide a sufficiently stable base platform for future robotic manipulation operations, where the inclusion of the robotic manipulator introduces further complexity.

1.2 Research Objectives and Methodology

Taking into account the considerations discussed in the previous sections, this thesis aims to investigate CSI during rapid pointing maneuvers (LASM). The multi-body mathematical model of the flexible satellite is defined in a parametric manner to enable the study of the phenomenon by evaluating different satellite configurations and exploring various operational scenarios. The SMC technique, renowned for its robustness against parametric uncertainties and external disturbance torques, is chosen for investigation, but it is formulated within a novel adaptive architecture. This logic is specifically designed to optimize the different phases of the maneuver and effectively manage the available torque budget, avoiding actuator saturation, and ensuring system stability even in the presence of significant disturbance torques. Ultimately, the robustness of the system is evaluated under parametric uncertainties and varying operational scenarios.

The *MATLAB / Simulink* platform is utilized to generate the mathematical model, develop and implement the ASMC control law, and validate the results obtained. The developed codes are provided in the Appendix A.

1.3 Thesis Outline

This thesis work is organized into six chapters. The contents of each chapter are summarized below to guide the reader through the document.

Chapter 1 introduces the reference scenario for modern space missions, analyzing the technological challenges imposed by the use of large flexible structures. Through a review of the state of the art, the problem CSI is contextualized, highlighting the limitations of current solutions and defining the motivations behind the research. Finally, the objectives of the work and the tools adopted to tackle the problem are presented.

Chapter 2 presents the mathematical formulation of the problem. It describes the mathematical model of the flexible satellite that will be used for the validation of the control law, and derives the multi-body dynamic equations using the Lagrangian approach. This yields a control-affine mathematical formulation that is easily integrable with a nonlinear control law SMC.

Chapter 3 numerically defines the nominal case study for the Open-Loop validation of the nonlinear flexible satellite model described in the previous chapter. Through modal analysis and energy verifications, the physical consistency of the simulator and the correct representation of the dynamic coupling are demonstrated.

Chapter 4 briefly explains the functioning of the traditional Sliding Mode Control technique. Subsequently, it describes in detail the adaptive control law (ASMC) proposed in this thesis work.

Chapter 5 presents the results of the numerical simulation campaign. Resuming the nominal case study defined in the third chapter, the investigation proceeds with an approach of increasing complexity. First, the control law is validated on the complete flexible model, including the effect of environmental disturbance torques set to a critical value associated with their maximum amplitude. Subsequently, a sensitivity analysis is performed to evaluate the robustness of the adaptive control law against parametric uncertainties. Finally, the chapter concludes with a robustness test across different operational scenarios, simulating the dynamic response of the system under varying initial conditions.

Chapter 6 is the final chapter. It presents a brief summary and a critical review of the work performed. The effectiveness of the parametric model and the adaptive control law is analyzed, and identified flaws and physical limitations are reported. Finally, possible future developments for the research are defined.

Chapter 2

Mathematical Model of the Flexible Satellite

Contents

2.1 Model Architecture and Assumptions 6
2.1.1 Definition of Reference Frames 7
2.1.2 System State Definition 8
2.1.3 Model Assumptions and Limitations 8
2.2 Characterization of the Model Components 9
2.2.1 Rigid Hub 9
2.2.2 Flexible Appendages 10
2.2.3 Elastic and Dissipative Interface 12
2.3 Derivation of the Equations of Motion 16
2.3.1 Kinematics of the System Components 17
2.3.1.1 Hub Kinematics 18
2.3.1.2 Kinematics of the Flexible Appendages 19
2.3.2 Energy Analysis of the System 20
2.3.2.1 Total Kinetic Energy (T) 20
2.3.2.2 Elastic Potential Energy (U) 21
2.3.2.3 Rayleigh Dissipation Function (D) 21
2.3.3 Analytical Derivation of the Equation Terms 22
2.3.4 Final Model Formulation 24

The design and validation of a robust attitude control system require, as a fundamental prerequisite, the availability of a mathematical representation of the system.

This chapter presents the derivation of the mathematical model for the flexible satellite under study. The aim of this work does not lie in the derivation of a high-fidelity model (typical of static structural analyzes FEM), but rather in the formulation of a dynamic Control-Oriented Model. Such a model must describe the time evolution of the state of the system under the effect of control torques and external disturbances, explicitly highlighting how rapid reorientation maneuvers (LASM) excite the structure and, conversely, how the elastic deformation of the flexible appendages influences the satellite's attitude.

The model must be fully parametric and computationally efficient. Indeed, it must easily represent different geometric, inertial, and modal properties of the system while ensuring extremely short numerical integration times. This combination is the fundamental prerequisite for enabling the practical execution of extensive simulation campaigns (such as Monte Carlo analyzes and sensitivity studies), which require thousands of iterations to statistically evaluate the robustness of the control law under varying nominal conditions and operational scenarios.

The following sections first describe the topological architecture of the multi-body system and the simplifying assumptions adopted for its treatment. Subsequently, the individual components of the satellite (central Hub and appendages) are characterized, detailing the Lumped Parameter Approach (LPA). Finally, the complete nonlinear equations of motion are derived using the Lagrangian energy approach, which allows obtaining a closed-form formulation of the coupled system's nonlinear dynamics in a control-affine form.

The entire mathematical architecture presented in this chapter is fully translated into code through dedicated scripts. For details on the implementation of the software, flow charts, and accessory functions developed, the reader is referred to the Appendix A, which is conceived as a formal guide for the execution of the simulator.

2.1 Model Architecture and Assumptions

The system is modeled as a multi-body system, composed of three interconnected rigid bodies: a central Hub and two lateral appendages (Solar Panels). The general sketch of the coupled system is shown in Figure 2.1. To account for the elasticity of the flexible appendages within the multi-body model, a Lumped Parameter Approach (LPA) is adopted. In this formulation, the distributed flexibility of the appendages is lumped at the connection interface (Joint) between the Hub and the rigid body of the panel. This assumption reduces the modeling complexity of the physical system, ensures a high level of computational efficiency, and allows maintaining a good level of fidelity to the actual dynamic behavior. The topology of the system is defined as follows:

- **Central Hub**: A 6 Degrees of Freedom (DOF) rigid body, acting as a base reference (Base Body) for the kinematic chain.
- **Flexible Appendages**: Two rigid bodies (Panels) connected to the Hub via an elastic joint. Each flexible appendage has 6 relative DOF with respect to its attachment point.
- **Geometric Offsets**: The panels are connected to the Hub through massless rigid arms (Offsets), which simulate the geometric footprint of the primary structure and increase the inertia of the coupled model.

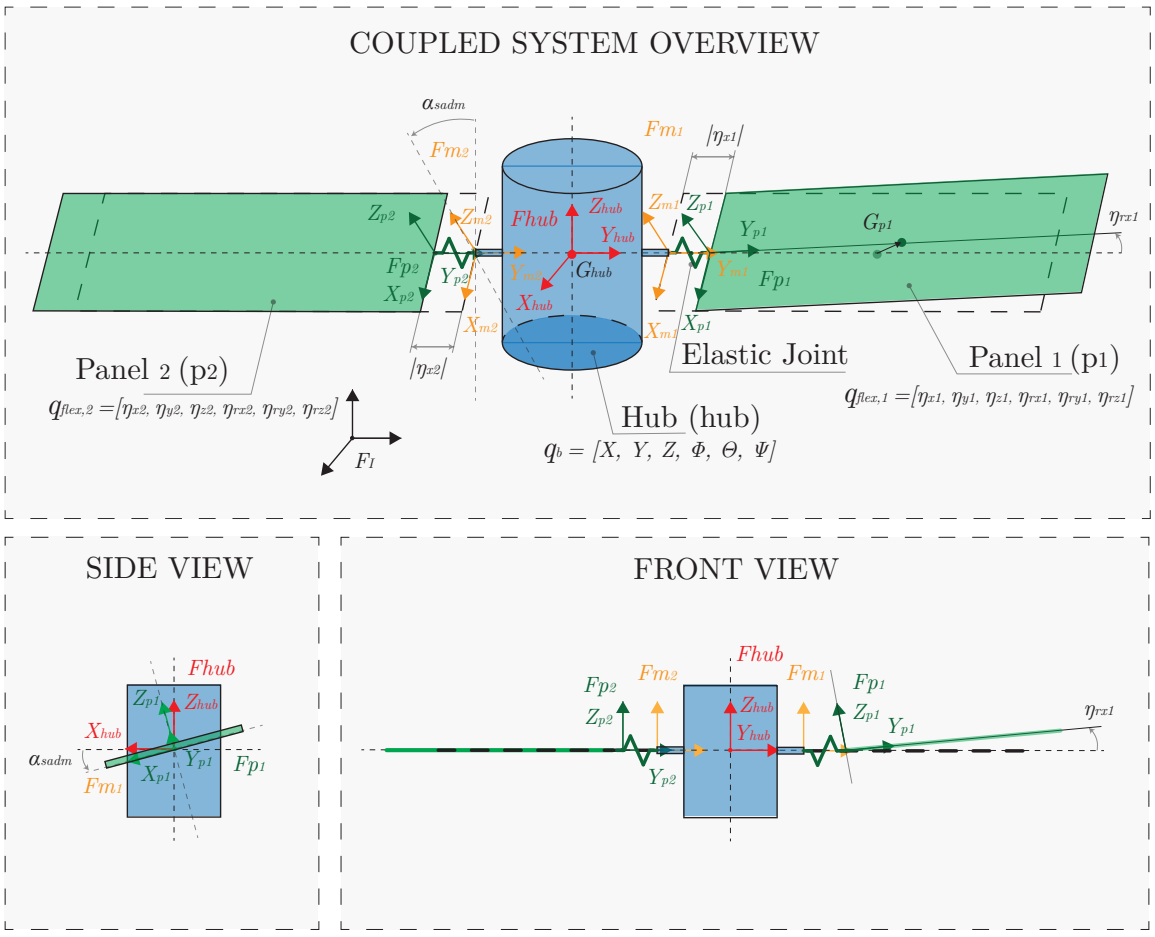

Figure 2.1: Main view of the coupled system, composed of the rigid Hub and the two flexible appendages: definition of the reference frames, state variables of the main rigid body, elastic deformation variables, and topological configuration. (Note: This figure depicts the coupled system in a generic deformed configuration).

2.1.1 Definition of Reference Frames

To uniquely describe the system configuration, the following coordinate systems (Frames) are defined, as shown in Figure 2.1:

Inertial Frame ($\mathcal{F}_I$): A fixed frame in inertial space.

Body Frame ($\mathcal{F}_{hub}$): A frame attached to the Hub, with its origin located at the Center of Mass (G_{hub}) and its axes aligned with the geometric axes of the central body. This frame serves as the reference with respect to which the angular velocities ($\boldsymbol{\omega}_{hub}$) and the global attitude are measured. Furthermore, the overall inertia matrix of the satellite varies with respect to this frame depending on the panels' configuration.

Mounting Frame ($\mathcal{F}_{m,i}$): A reference frame fixed to the Hub but translated to the attach-

ment point of the i-th panel ($i = 1, 2$). Its orientation includes the static rotation α_{sadm} about the Y_{hub} axis.

Panel Frame ($\mathcal{F}_{p,i}$): A frame rotated by α_{sadm} about the Y_{hub} axis and attached to the base of the i-th panel. The relative motion between $\mathcal{F}_{p,i}$ and $\mathcal{F}_{m,i}$ defines the elastic deformation coordinates and measures the displacement (elastic deformations) of the root of the i-th panel with respect to the attachment point on the rigid Hub.

2.1.2 System State Definition

The state of the system is defined by the following vector of generalized coordinates $\mathbf{q} \in \mathbb{R}^{18}$:

$$\underset{\in\mathbb{R}^{18\times 1}}{\mathbf{q}} = \begin{bmatrix} q_{hub} \\ q_{flex,1} \\ q_{flex,2} \end{bmatrix} \tag{2.1}$$

Where:

- $\mathbf{q}_{hub} \in \mathbb{R}^6$: position and Euler angles of the central body with respect to the inertial frame ($\mathcal{F}_I$).
- $\mathbf{q}_{flex,i} \in \mathbb{R}^6$: elastic deformations (translations $\boldsymbol{\eta_i}$ and rotations $\boldsymbol{\eta_{r,i}}$) of the i-th panel in the local frame $\mathcal{F}_{m,i}$.

2.1.3 Model Assumptions and Limitations

The formulation of the equations of motion is based on the following physical assumptions:

1. **Configuration Generality**: The model is parametric and does not impose symmetry constraints between the two panels. The panels can rotate around their own $Y_{p,i}$ axis at an angle α_{sadm}. The angle of orientation of the panel α_{sadm} is treated as a constant configuration parameter. It is assumed that the rotation mechanism (Single Axis Drive Mechanism - SADM) is locked ($\dot{\alpha}_{sadm} = 0$) during the rapid reorientation maneuver, or that its solar tracking dynamics is significantly slower than the attitude dynamics.
2. **Kinematic Assumptions**: The model exactly describes the large rigid rotations of the Hub (full nonlinear kinematics). For the flexible part, the assumption of small elastic deformations ($\boldsymbol{\eta_i}/L \ll 1, \boldsymbol{\eta_{r,i}} \ll 1$ rad) is adopted with respect to the non-deformed configuration. This assumption is physically consistent with the structural stiffness typical of deployed space appendages, even for LSS.
3. **Elastic Linearity**: By virtue of small deformations, the elastic interaction is legitimately modeled using a linear constitutive law ($U = \frac{1}{2}\mathbf{q}_{flex}^T K \mathbf{q}_{flex}$).

4. **Damping Model**: A simple viscous damping model $F_d = -c\dot{x}$ is adopted. This model is valid in the presence of small damping ratios $\zeta \ll 0.1 \quad (10\%)$.

5. **First Mode Approximation**: The lumped parameter discretization (LPA) with a single rigid body per panel limits the model's validity to the representation of the first fundamental vibration mode across all 6 DOF. Representing higher-order bending modes would require a finer spatial discretization, dividing the appendage into a kinematic chain of N rigid segments connected in series; this additional complexity is deemed unnecessary for the control objectives of this work.

6. **Offsets and Inertia**: The connection arms, depicted in Figure 2.1 as small cylinders, are modeled as massless kinematic constraints.

7. **Environment and Microgravity**: The system operates in zero-gravity conditions. The potential energy consists exclusively of elastic energy; the gravitational contribution is null.

2.2 Characterization of the Model Components

This section describes the physical, inertial, and geometric properties of the rigid bodies constituting the multi-body system, as well as the parameterization of the elastic interface used to represent the flexibility.

2.2.1 Rigid Hub

The central body (Hub) represents the primary structure of the satellite. It is modeled as a homogeneous rigid body with mass M_{hub}.

In the nominal model, the Hub is conceived as a cylinder of height H_{hub} and radius R_{hub}, with its axis of symmetry coinciding with the Z_{hub} axis of the body frame. Figure 2.2 presents the dimensioned sketch of the described model along with its corresponding geometric definitions.

Inertial properties are described by the inertia tensor $\mathbf{J}_{hub} \in \mathbb{R}^{3\times3}$, defined with respect to the body-fixed frame $\mathcal{F}_{hub}$. Assuming a homogeneous mass distribution and coincidence between the geometric axes and the principal axes of inertia, the matrix assumes the following diagonal form:

$$\underset{\in\mathbb{R}^{3\times3}}{\mathbf{J}_{hub}} = \begin{bmatrix} J_{hub,xx} & 0 & 0 \\ 0 & J_{hub,yy} & 0 \\ 0 & 0 & J_{hub,zz} \end{bmatrix} \tag{2.2}$$

The principal moments of inertia are calculated analytically as a function of the cylindrical

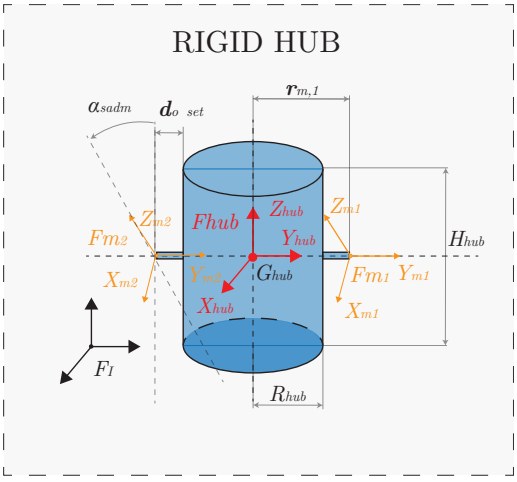

Figure 2.2: Geometric representation of the rigid Hub with the main geometric dimensions and definition of the mounting vectors.

geometry:

$$J_{hub,xx} = J_{hub,yy} = \frac{1}{12} M_{hub}(3R_{hub}^2 + H_{hub}^2) \tag{2.3}$$

$$J_{hub,zz} = \frac{1}{2} M_{hub} R_{hub}^2 \tag{2.4}$$

The Hub serves as the base for the connection of the appendages. The position of the attachment points with respect to the center of mass G_{hub} is defined by the constant vectors $\mathbf{r}_{m,1}$ and $\mathbf{r}_{m,2}$ expressed in body coordinates:

$$\underset{\in\mathbb{R}^{3\times1}}{\mathbf{r}_{m,1}} = \begin{bmatrix} 0 \\ +(R_{hub} + d_{offset}) \\ 0 \end{bmatrix}, \quad \underset{\in\mathbb{R}^{3\times1}}{\mathbf{r}_{m,2}} = \begin{bmatrix} 0 \\ -(R_{hub} + d_{offset}) \\ 0 \end{bmatrix} \tag{2.5}$$

where d_{offset} represents the length of the rigid massless connecting arms.

This body is subjected to the control torques generated by the actuators, denoted by $\boldsymbol{\tau}_{ctrl}$ (reaction wheels or thrusters), and to the external disturbance torques $\boldsymbol{\tau}_{dist}$.

2.2.2 Flexible Appendages

Under the assumptions of the Lumped Parameter Approach (LPA), each solar panel is modeled as a rigid body in the shape of a rectangular parallelepiped. The geometry of the panel is defined by its length L_p, width W_p, and thickness t_p. Assuming a uniform surface density ρ_{sup}, the total mass M_p of each appendage is given by:

$$M_p = \rho_{sup} \cdot L_p \cdot W_p \tag{2.6}$$

The characteristics of the generic panel are defined in the local reference frame $\mathcal{F}_{p,i}$ (Panel Frame), which originates at the connection point to the elastic joint (panel root). Consistent with the system's topology (where the local Y-axis represents the longitudinal axis of the appendage), the position of the Center of Mass (G_p) with respect to the origin of the frame $\mathcal{F}_{p,i}$ is identified by the vector $\mathbf{d}_{Gp}$:

$$\underset{\in\mathbb{R}^{3\times1}}{\mathbf{d}_{Gp}^{(\mathcal{F}_{p,i})}} = \begin{bmatrix} 0 \\ d_{Gp,local} \\ 0 \end{bmatrix}, \quad \text{with} \quad d_{Gp,local} = \frac{L_p}{2} \tag{2.7}$$

It is therefore assumed that the geometric centroid coincides with the center of mass of the equivalent rigid body.

Figure 2.3 presents the dimensioned sketch of the described model along with the relevant geometric definitions. The figure depicts both the undeformed panel configuration (dashed line) and a generic deformed configuration to highlight the degrees of freedom of the flexible appendage.

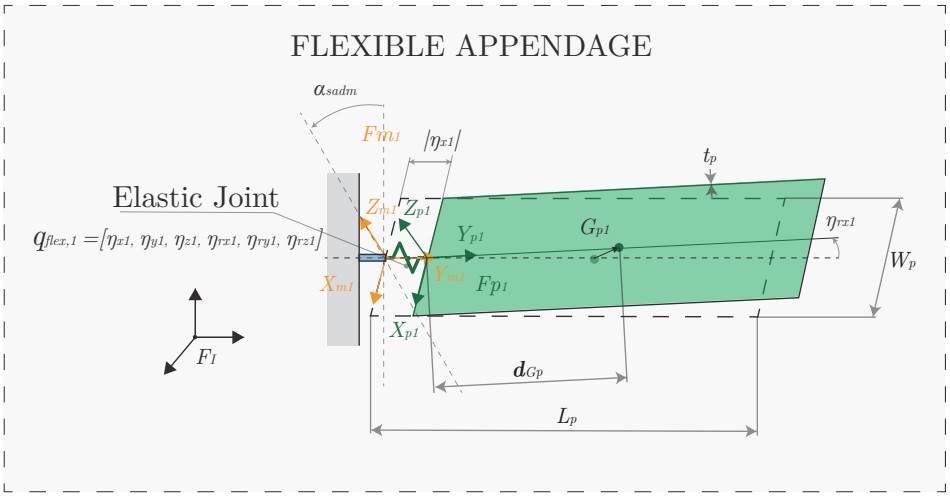

Figure 2.3: Geometric representation of the rigid panel in the undeformed (dashed line) and deformed configurations, along with the main geometric dimensions and reference frames. Representation of the flexible joint, the element where all elasticity is lumped, shown in dark green in the drawing. The combination of the rigid panel and the elastic joint constitutes the flexible appendage.

Inertial properties are described by the centroidal inertia tensor $\mathbf{J}_p \in \mathbb{R}^{3\times3}$. Assuming the panel to be a homogeneous thin plate, the principal moments of inertia are calculated analytically with respect to the axes of the local frame:

$$\underset{\in\mathbb{R}^{3\times3}}{\mathbf{J}_p} = \begin{bmatrix} J_{p,xx} & 0 & 0 \\ 0 & J_{p,yy} & 0 \\ 0 & 0 & J_{p,zz} \end{bmatrix} \tag{2.8}$$

The components of the diagonal matrix are derived from the following geometric relationships, which account for the mass distribution along the principal dimensions:

$$J_{p,xx} = \frac{1}{12} M_p (L_p^2 + t_p^2) \tag{2.9}$$

$$J_{p,yy} = \frac{1}{12} M_p (W_p^2 + t_p^2) \tag{2.10}$$

$$J_{p,zz} = \frac{1}{12} M_p (L_p^2 + W_p^2) \tag{2.11}$$

Note that

- $J_{p,yy}$ represents the torsional inertia on the longitudinal axis (minimum, dependent mainly on the width W_p).
- $J_{p,xx}$ and $J_{p,zz}$ represent the bending inertias (dominant, dependent on the length L_p).

Finally, the panel's orientation with respect to the Hub is imposed via the static angle α_{sadm} (SADM), which defines a fixed rotation about the local Y-axis prior to deformation. The flexible interaction is modeled by defining the relative kinematics between the frame that originates at the attachment point of the flexible appendages, $\mathcal{F}_{m,i}$ (fixed to the Hub, rotated) and the panel frame $\mathcal{F}_{p,i}$. In the undeformed configuration, the origins and axes of the two frames coincide. In the presence of deformation, the frame $\mathcal{F}_{p,i}$ is translated and rotated with respect to $\mathcal{F}_{m,i}$.

The deformation state is described by the following vectors:

- $\boldsymbol{\eta}_i = [\eta_{x,i}, \eta_{y,i}, \eta_{z,i}]^T$: relative translation vector of the origin of $\mathcal{F}_{p,i}$ with respect to $\mathcal{F}_{m,i}$.
- $\boldsymbol{\eta}_{r,i} = [\eta_{rx,i}, \eta_{ry,i}, \eta_{rz,i}]^T$: relative rotation vector (Euler angles for small rotations) that aligned $\mathcal{F}_{m,i}$ with $\mathcal{F}_{p,i}$.

These 6 relative DOF constitute the generalized elastic coordinates $\mathbf{q}_{flex,i}$ introduced in the state of the system. Figure 2.3 geometrically illustrates this separation: the vector $\mathbf{d}_{Gp}$ is rigidly defined in the $\mathcal{F}_{p,i}$ frame, while the flexibility is confined to the relative motion between the two frames at the root.

2.2.3 Elastic and Dissipative Interface

The dynamic interaction between the Hub and the appendages is governed by the elastic and dissipative forces acting on the relative generalized coordinates $\mathbf{q}_{flex,i}$ defined in the previous section. In the Lumped Parameter Approach (LPA), this interaction is represented by diagonal stiffness ($\mathbf{K}_{flex}$) and damping ($\mathbf{C}_{flex}$) matrices, defined in the local frame $\mathcal{F}_{m,i}$. Although

energy dissipation in composite materials and mechanical joints is hysteretic (structural), for the purposes of control synthesis and time-domain simulation, it is modeled according to the simple viscous damping approach. When the damping assumes very small values ($\zeta \ll 0.1 \quad (10\%)$), as in the present case study, an extremely precise model is not required to understand exactly how energy is dissipated in each vibration cycle. The adoption of a visco-elastic model or an equivalent viscous model for the purpose of modeling hysteretic damping is not necessary.

For each panel, the stiffness matrix $\mathbf{K}_{flex} \in \mathbb{R}^{6\times6}$ is composed of translational (k_t) and rotational (k_r) coefficients. Assuming elastic decoupling between the axes, the matrix assumes the following diagonal form:

$$\underset{\in\mathbb{R}^{6\times6}}{\mathbf{K}_{flex}} = \begin{bmatrix} k_{tx} & 0 & 0 & 0 & 0 & 0 \\ 0 & k_{ty} & 0 & 0 & 0 & 0 \\ 0 & 0 & k_{tz} & 0 & 0 & 0 \\ 0 & 0 & 0 & k_{rx} & 0 & 0 \\ 0 & 0 & 0 & 0 & k_{ry} & 0 \\ 0 & 0 & 0 & 0 & 0 & k_{rz} \end{bmatrix} \tag{2.12}$$

Similarly, energy dissipation is modeled according to the **viscous damping** approach. The corresponding matrix $\mathbf{C}_{flex}$ is defined as:

$$\underset{\in\mathbb{R}^{6\times6}}{\mathbf{C}_{flex}} = \begin{bmatrix} c_{tx} & 0 & 0 & 0 & 0 & 0 \\ 0 & c_{ty} & 0 & 0 & 0 & 0 \\ 0 & 0 & c_{tz} & 0 & 0 & 0 \\ 0 & 0 & 0 & c_{rx} & 0 & 0 \\ 0 & 0 & 0 & 0 & c_{ry} & 0 \\ 0 & 0 & 0 & 0 & 0 & c_{rz} \end{bmatrix} \tag{2.13}$$

Parameter Tuning Methodology. Since the LPA model is a discretization of a continuous system, the values of k and c are not direct material properties, but rather parameters whose values are calculated to replicate the fundamental modal frequencies of the actual structure. Following a classical approach, the natural frequencies of the system are derived once the values of stiffness k and mass M are known. In this specific case, the adopted calculation procedure follows an inverse approach based on the assignment of target natural frequencies, implemented in the *MATLAB* environment, to ensure dynamic consistency with the varying inertial properties. For each configuration of the flexible appendage, depending on the assigned geometric dimensions (W_p, L_p) and the imposed inertial characteristics (M_p), the model auto-adapts by calculating the correct stiffness values to keep the natural frequencies constant.

For each DOF j associated with the state of the flexible appendage, once a target natural frequency $f_{n,j}$ (in Hz) representative of the vibration mode (e.g., First Flapping Mode,

Torsional Mode, In-plane Bending Mode) is set, the equivalent stiffness is calculated as:

$$k_j = J_{eq,j} \cdot (2\pi f_{n,j})^2 \tag{2.14}$$

where $J_{eq,j}$ represents the equivalent inertia (or mass) seen by the j-th degree of freedom.

In order to minimize modeling errors, the calculation is automated through a dedicated initialization script. In this script, the value of $J_{eq,j}$ is extracted directly from the diagonal of the mass matrix of the overall system (M_{sys}), which is computed symbolically in the undeformed configuration. This ensures that the stiffness is perfectly tuned to the actual inertia of the multi-body model, regardless of the geometric complexity of the panels.

Finally, the damping matrix is calculated to impose a specific dimensionless damping ratio ζ_j (typically $\zeta \approx 0.005 \div 0.01$ for space structures), according to the relationship:

$$c_j = 2\zeta_j(2\pi f_{n,j})J_{eq,j} \tag{2.15}$$

This parameterization allows simulating operational scenarios with different flexibility characteristics (e.g., soft or stiff panels) by exclusively modifying the target frequencies in the initialization code, without altering the structure of the equations of motion.

Considerations on Geometric and Centrifugal Stiffening. The assumption of a constant stiffness matrix $\mathbf{K}_{flex}$ (calculated in the undeformed configuration) implies that the natural frequencies of the flexible appendages (also defined in the undeformed configuration at $\boldsymbol{\omega}_{hub} = [0; 0; 0]^T$) are invariant with respect to the angular velocity of the central body ($\boldsymbol{\omega}_{hub}$).

In reality, flexible systems subjected to large overall rotations undergo the phenomenon of Geometric Stiffening (or Centrifugal Stiffening), whereby centrifugal inertia forces induce a stress state that increases the transverse stiffness of the structure and, consequently, its natural frequencies as the angular velocity increases. Authors such as Liu and Hong demonstrate in various studies on beams [LH03] and rectangular plates [JyJ05] that the use of classical linear formulations (without nonlinear geometric coupling terms) fails to capture this variation of stiffness.

However, these same studies highlight that the error introduced by the constant stiffness model is negligible when the rotation speed is low compared to the first natural frequency of the structure. Specifically, for rectangular plates, the conventional method is considered accurate for angular velocities $\omega < 0.29\omega_{n,1}$ [JyJ05]. Since the LASM maneuvers planned for the satellite under consideration occur at low angular velocities (typically on the order of 10^{-2} rad/s) relative to the natural frequencies of the panels ($f_n \geq 0.25$ Hz), the centrifugal stiffening effect is considered negligible. This justifies the adoption of a constant stiffness matrix to reduce computational complexity without compromising simulation accuracy. To model these effects, one would need to use a nonlinear stiffness matrix $\mathbf{K}_{flex}(\mathbf{q}, \dot{\mathbf{q}})$ that is capable of updating at each time step. This would enormously complicate the solver for a

negligible gain in precision.

For the analysis of operational scenarios characterized by high spin rates or extremely flexible structures, and just in case higher precision is desired, the reader is referred to advanced nonlinear formulations that include axial deformation terms (foreshortening deformation) as proposed in [JyJ05].

Phenomenological Analysis of Spin Softening. In the present model, the use of dynamically nonlinear Lagrangian formulations coupled with linear elastic models tends to numerically produce a phenomenon opposite to the one described in the previous section, known as Spin Softening (apparent frequency reduction).

To understand the physical origin of the Spin Softening phenomenon inherent in the formulation LPA with constant stiffness $\mathbf{K}_{flex}$, consider a simplified one-degree-of-freedom (1-DOF) model representative of a rotating flexible appendage.

Let $\eta(t)$ be the elastic deformation coordinate (tip displacement with respect to the root) and r_{hub} the distance of the lumped mass from the rigid central body. When the system rotates at a constant angular velocity Ω, two antagonistic forces act on the equivalent modal mass m along the radial direction:

- Elastic restoring force (F_{el}): Tends to return the appendage to its undeformed configuration. Assuming a linear model:

$$F_{el} = -k \cdot \eta \tag{2.16}$$

- Centrifugal force (F_{cf}): Tends to move the mass away from the center of rotation. Its intensity depends on the total radial distance from the center of rotation ($R_{tot} = r_{hub} + \eta$):

$$F_{cf} = m\Omega^2(r_{hub} + \eta) = \underbrace{m\Omega^2 r_{hub}}_{F_{static}} + \underbrace{m\Omega^2\eta}_{F_{dynamic}} \tag{2.17}$$

The local equation of motion in the rotating reference frame is written by imposing a dynamic equilibrium ($m\ddot{\eta} = \sum F$):

$$m\ddot{\eta} = F_{el} + F_{cf} = -k\eta + m\Omega^2 r_{hub} + m\Omega^2\eta \tag{2.18}$$

Grouping the terms dependent on the deformation coordinate η on the left-hand side, we obtain:

$$m\ddot{\eta} + \underbrace{(k - m\Omega^2)}_{k_{eff}}\eta = m\Omega^2 r_{hub} \tag{2.19}$$

From the analysis of the effective stiffness term (k_{eff}), the effect of rotation clearly

emerges:

$$k_{eff}(\Omega) = k - m\Omega^2 < k \tag{2.20}$$

Since the centrifugal inertial term $-m\Omega^2$ is negative, it subtracts from structural stiffness k. Consequently, the natural frequency of the rotating system (ω_{rot}) is lower than that of the static one (ω_n):

$$\omega_{rot} = \sqrt{\frac{k - m\Omega^2}{m}} = \sqrt{\omega_n^2 - \Omega^2} \tag{2.21}$$

This result analytically demonstrates why the present model with constant structural stiffness (k = cost), including nonlinear inertial forces (and therefore centrifugal forces), predicts a reduction in natural frequencies (Softening). In order for the model to represent the actual physical phenomenon of stiffening, it would be necessary for the elastic term k not to be constant, but to depend nonlinearly on the stress state induced by the rotation itself ($k = k(\Omega) \approx k_0 + c\Omega^2$), in such a way as to overcome the Centrifugal Softening term.

2.3 Derivation of the Equations of Motion

In this section, the complete mathematical model that describes the dynamics of the flexible satellite is derived, leading to a closed-form formulation suitable for numerical simulation. The objective is to obtain a system of second-order Ordinary Differential Equations (ODE) in general nonlinear vector form:

$$\boxed{\mathbf{M}(\mathbf{q})\ddot{\mathbf{q}} + \mathbf{h}(\mathbf{q}, \dot{\mathbf{q}}) + \mathbf{C}_{damp}\dot{\mathbf{q}} + \mathbf{k}_{el}(\mathbf{q}) = \boldsymbol{\tau}_{ext}} \tag{2.22}$$

where:

- $\mathbf{M}(\mathbf{q}) \in \mathbb{R}^{18\times18}$ is the mass matrix (symmetric and positive definite), representing the inertial properties of the multi-body system.
- $\mathbf{h}(\mathbf{q}, \dot{\mathbf{q}}) \in \mathbb{R}^{18}$ is the vector of convective terms, containing Coriolis and centrifugal forces arising from high angular velocities and dynamic couplings.
- $\mathbf{C}_{damp} \in \mathbb{R}^{18\times18}$ is the damping matrix that models the dissipation of viscous energy at the joints where the elasticity of the flexible appendages is lumped.
- $\mathbf{k}_{el}(\mathbf{q}) \in \mathbb{R}^{18}$ is the vector of elastic forces, obtained from the gradient of the potential energy, which describes the elastic restoring force of the flexible appendages.
- $\boldsymbol{\tau}_{ext} \in \mathbb{R}^{18}$ is the vector of external generalized forces and torques (e.g., motor actuation, various external disturbance torques).

This representation is chosen because it exactly reflects the way the simulator computes the accelerations at each time instant. Rather than constructing complex matrices that mask

the physical terms, the adopted approach clearly separates the inertia ($\mathbf{M}$) from the forces. Conceptually, equation 2.22 is nothing more than a generalized formulation of Newton's Second Law of Motion ($F = ma$):

$$\text{Acceleration}(\ddot{\mathbf{q}}) = \mathbf{M}^{-1} \cdot (\text{External Forces} - \text{Internal Forces}) \tag{2.23}$$

where the "Internal Forces" are precisely the sum of the vectors $\mathbf{h}$, $\mathbf{k}$, and the damping terms. This makes the model extremely transparent and computationally efficient, as it allows for the direct calculation of the force vectors and acceleration without unnecessary intermediate steps.

Structure of the Derivation. The analytical derivation is conducted following the Euler-Lagrange energy approach. This method allows for systematically managing the complexity of an 18-degree-of-freedom system by operating on scalar quantities (kinetic energy, potential energy, and dissipation function), which are independent of the local reference frame. The entire procedure is automated in the *MATLAB* environment using the *Symbolic Math Toolbox* through the script provided in the Appendix A.1.

The discussion follows the logical flow of the computational script, structured into the following steps:

1. **Kinematics of the Hub and Flexible Appendages:** Definition of the position vectors and calculation of the absolute velocities of the Hub and Panels.
2. **Energy Analysis:** Formulation of the total Kinetic Energy (T), the elastic Potential Energy (U) and the Rayleigh Dissipation Function (D).
3. **Analytical Derivation of the Equation Terms:**
   - Calculation of the Mass Matrix $\mathbf{M}$ (Hessian of the Kinetic Energy with respect to velocities).
   - Calculation of the vector $\mathbf{h}$.
   - Calculation of the vector $\mathbf{k}_{el}$ (Gradient of U) and the matrix $\mathbf{C}_{damp}$ (Hessian of D).
4. **Final Assembly:** Composition of the vector equation of motion (Eq. 2.22).

2.3.1 Kinematics of the System Components

The construction of the Lagrangian model requires a precise definition of the kinematic quantities (position and velocity) for all rigid and flexible bodies that make up the system. Consistent with the approach implemented in the computational script, the kinematics of the Hub are defined with respect to the inertial frame $\mathcal{F}_i$; however, the velocities are subsequently projected into the local frame (Body Frame) $\mathcal{F}_b$ to simplify the calculation of the rotational kinetic energy.

2.3.1.1 Hub Kinematics

The positional state of the Hub is defined by the center of mass position vector $\mathbf{r}_{hub} \in \mathbb{R}^3$ and the Euler angles vector $\mathbf{\Theta}_{hub} \in \mathbb{R}^3$:

$$\mathbf{r}_{hub} = \begin{bmatrix} x_{hub} \\ y_{hub} \\ z_{hub} \end{bmatrix}, \quad \mathbf{\Theta}_{hub} = \begin{bmatrix} \phi_{hub} \\ \theta_{hub} \\ \psi_{hub} \end{bmatrix} \tag{2.24}$$

To describe the spacecraft's orientation, the standard aerospace ZYX (3-2-1) rotation sequence is adopted: Yaw (ψ) $\rightarrow$ Pitch (θ) $\rightarrow$ Roll (ϕ). The rotation matrix $\mathbf{R}_{IB}$ that transforms coordinates from the Body-fixed frame to the Inertial frame is given by the product of the elementary matrices:

$$\mathbf{R}_{IB} = \mathbf{R}_z(\psi_{hub})\mathbf{R}_y(\theta_{hub})\mathbf{R}_x(\phi_{hub}) \tag{2.25}$$

The inverse transformation (Inertial $\rightarrow$ Body) is given by transposing $\mathbf{R}_{BI} = \mathbf{R}_{IB}^T$.

Linear and angular velocities, required for the energy formulation, are expressed in the Hub's body-fixed reference frame ($\mathcal{F}_{hub}$):

Linear Velocity (Body Frame). The inertial linear velocity $\dot{\mathbf{r}}_h$ is projected onto the local axes of the Hub using the inverse rotation matrix:

$$\mathbf{v}_{hub}^{(\mathcal{F}_{hub})} = \mathbf{R}_{BI} \cdot \dot{\mathbf{r}}_{hub} = \mathbf{R}_{IB}^T \cdot \begin{bmatrix} \dot{x}_{hub} \\ \dot{y}_{hub} \\ \dot{z}_{hub} \end{bmatrix} \tag{2.26}$$

Angular Velocity (Body Frame). The angular velocity vector $\boldsymbol{\omega}_{hub}^{(\mathcal{F}_{hub})} = [p, q, r]^T$ does not coincide with the simple time derivative of the Euler angles ($\dot{\mathbf{\Theta}}_{hub}$), but is related to it through the nonlinear kinematic relationship associated with the ZYX sequence:

$$\boldsymbol{\omega}_{hub}^{(\mathcal{F}_{hub})} = \begin{bmatrix} \omega_{hub,x} \\ \omega_{hub,y} \\ \omega_{hub,z} \end{bmatrix}_{\mathcal{F}_{hub}} = \mathbf{S}(\mathbf{\Theta}_h)\dot{\mathbf{\Theta}}_h \tag{2.27}$$

Explicating the kinematic transformation matrix $\mathbf{S}(\mathbf{\Theta}_h)$ derived in the script:

$$\boldsymbol{\omega}_{hub}^{(\mathcal{F}_{hub})} = \begin{bmatrix} 1 & 0 & -\sin(\theta_{hub}) \\ 0 & \cos(\phi_{hub}) & \cos(\theta_{hub})\sin(\phi_{hub}) \\ 0 & -\sin(\phi_{hub}) & \cos(\theta_{hub})\cos(\phi_{hub}) \end{bmatrix} \begin{bmatrix} \dot{\phi}_{hub} \\ \dot{\theta}_{hub} \\ \dot{\psi}_{hub} \end{bmatrix} \tag{2.28}$$

Following the kinematic analyzes, the total kinetic energy of the Hub (T_{hub}) can be cal-

culated, which will be formalized in the following section as the sum of the translational and rotational contributions. It should be noted that the use of velocities projected into the Hub's body-fixed frame ($\mathcal{F}_{hub}$) allows treating the inertia tensor $\mathbf{J}_{hub}$ as a constant diagonal matrix, significantly simplifying the time derivatives required by the Lagrangian algorithm.

2.3.1.2 Kinematics of the Flexible Appendages

Defining the kinematic state of the solar panels requires reconstruction of the kinematic chain connecting the Hub's center of mass (G_{hub}) to the center of mass of the generic i-th panel ($G_{p,i}$). This chain accounts for the rigid geometry, the static orientation of SADM, and the instantaneous elastic deformation.

The following vector quantities are defined in the Hub frame $\mathcal{F}_{hub}$:

- $\mathbf{r}_{m,i}^{(\mathcal{F}_{hub})}$: Position vector of the origin of the mounting frame $\mathcal{F}_{m,i}$ (root of the panel) with respect to G_{hub}. This constant vector includes both the radial dimension of the Hub (R_{hub}) and the joint structural offset d_{offset}.
- $\mathbf{d}_{Gp}$: Constant vector in the local panel frame $\mathcal{F}_{p,i}$ identifying the position of the geometric centroid (at a distance of $L_p/2$ along the local Y-axis).
- $\mathbf{R}_{sadm,i}$: Static rotation matrix aligning the Hub frame with the mounting frame, defined by a rotation α_{sadm} about the Y-axis.
- $\mathbf{R}_{flex,i}$: Elastic rotation matrix constructed using the Euler angle sequence (Z-Y-X) associated with the rotational deformation coordinates ($\boldsymbol{\eta}_{r,i} = [\eta_{rx,i}, \eta_{ry,i}, \eta_{rz,i}]^T$).

Center of Mass Position. The position of the center of mass of the i-th panel, expressed in the Hub's reference frame ($\mathcal{F}_{hub}$), is calculated as:

$$\mathbf{r}_{G_{p,i}}^{(\mathcal{F}_{hub})} = \mathbf{r}_{m,i}^{(\mathcal{F}_{hub})} + \mathbf{R}_{sadm,i} \left(\boldsymbol{\eta}_i + \mathbf{R}_{flex,i} \mathbf{d}_{Gp} \right) \tag{2.29}$$

In this formulation, the translational deformation vector $\boldsymbol{\eta}_i = [\eta_{tx,i}, \eta_{ty,i}, \eta_{tz,i}]^T$ represents the relative displacement of the base of the panel with respect to the undeformed root ($\mathcal{F}_{m,i}$).

Absolute Linear Velocity of the Center of Mass. The absolute velocity of the center of mass of the panel, projected into the Hub frame ($\mathbf{v}_{G_{p,i}}^{(\mathcal{F}_{hub})}$), is the sum of different contributions: the velocity of the rigid hub $\mathbf{v}_{hub}^{(\mathcal{F}_{hub})}$ and the transport terms (Coriolis derivative). Considering that $\mathbf{r}_{G_{p,i}}^{(\mathcal{F}_{hub})}$ is a time-varying vector in a rotating frame with angular velocity $\boldsymbol{\omega}_{hub}^{(\mathcal{F}_{hub})}$:

$$\mathbf{v}_{G_{p,i}}^{(\mathcal{F}_{hub})} = \mathbf{v}_{hub}^{(\mathcal{F}_{hub})} + (\boldsymbol{\omega}_{hub}^{(\mathcal{F}_{hub})} \times \mathbf{r}_{G_{p,i}}^{(\mathcal{F}_{hub})}) + \dot{\mathbf{r}}_{G_{p,i}}^{(\mathcal{F}_{hub})} \tag{2.30}$$

The term $\dot{\mathbf{r}}_{G_{p,i}}^{(\mathcal{F}_{hub})}$ represents the relative velocity due exclusively to the variation of the elastic coordinates $(\dot{\boldsymbol{\eta}}_i, \dot{\boldsymbol{\eta}}_{r,i})$, calculated in the script as the symbolic time derivative of the relative position vector.

Total Angular Velocity. For the calculation of the rotational kinetic energy of the panel, it is necessary to express its absolute angular velocity projected into its local frame $(\mathcal{F}_{p,i})$. This velocity $(\boldsymbol{\omega}_{G_{p,i}}^{(\mathcal{F}_{p,i})})$ is the sum of the Hub's angular velocity (transported into the panel frame) and the local elastic angular velocity $(\dot{\boldsymbol{\eta}}_{r,i})$:

$$\boldsymbol{\omega}_{G_{p,i}}^{(\mathcal{F}_{p,i})} = (\mathbf{R}_{sadm,i}\mathbf{R}_{flex,i})^T \, \boldsymbol{\omega}_{hub}^{(\mathcal{F}_{hub})} + \dot{\boldsymbol{\eta}}_{r,i} \tag{2.31}$$

where $\dot{\boldsymbol{\eta}}_{r,i}$ is the vector of the angular deformation velocities $[\dot{\eta}_{rx,i}, \dot{\eta}_{ry,i}, \dot{\eta}_{rz,i}]^T$. This projection is fundamental so that the calculation of the rotational kinetic energy $(\frac{1}{2}\boldsymbol{\omega}_p^T \mathbf{J}_p \boldsymbol{\omega}_p)$ is consistent with the inertia tensor $\mathbf{J}_p$, which is constant and diagonal in its own local frame.

2.3.2 Energy Analysis of the System

Once the kinematic vectors have been defined, the next step consists of formulating the scalar energy quantities necessary to apply the Lagrange equation to derive the equations of motion. The total energy of the system is calculated as the sum of the contributions from the central rigid body (Hub) and the flexible appendages (Panels).

2.3.2.1 Total Kinetic Energy (T)

The total kinetic energy of the system T_{tot} is the sum of the kinetic energy of the Hub and that of the $N_p = 2$ appendages:

$$\boxed{T_{tot} = T_{hub} + \sum_{i=1}^{N_p} T_{p,i}} \tag{2.32}$$

Hub Contribution. Since the Hub is a rigid body, its kinetic energy consists of a translational and a rotational part. Using the velocities projected into the body-fixed frame $(\mathcal{F}_{hub})$ calculated in the previous section, one obtains the following:

$$T_{hub} = \underbrace{\frac{1}{2} M_{hub} (\mathbf{v}_{hub}^{(\mathcal{F}_{hub})T} \mathbf{v}_{hub}^{(\mathcal{F}_{hub})})}_{\text{Translational}} + \underbrace{\frac{1}{2} \boldsymbol{\omega}_{hub}^{(\mathcal{F}_{hub})T} \mathbf{J}_{hub} \boldsymbol{\omega}_{hub}^{(\mathcal{F}_{hub})}}_{\text{Rotational}} \tag{2.33}$$

where $\mathbf{J}_{hub}$ is the Hub's inertia tensor (constant and diagonal in $\mathcal{F}_{hub}$).

Appendages Contribution. Similarly, for each panel i, the kinetic energy is the sum of translational and rotational contributions. It is fundamental to note that, consistent with the numerical implementation:

- Linear velocity $\mathbf{v}_{G_{p,i}}^{(\mathcal{F}_{hub})}$ is expressed in the Hub frame ($\mathcal{F}_{hub}$). The dot product $\mathbf{v}^T\mathbf{v}$ is invariant under rotation; therefore, this choice is legitimate and convenient for calculations.
- The angular velocity $\boldsymbol{\omega}_{G_{p,i}}^{(\mathcal{F}_{p,i})}$ is expressed in the local panel frame ($\mathcal{F}_{p,i}$). This is necessary to ensure consistency with the panel's inertia tensor $\mathbf{J}_p$, which is defined in its own local coordinate system.

The analytical expression is:

$$T_{p,i} = \underbrace{\frac{1}{2}M_p(\mathbf{v}_{G_{p,i}}^{(\mathcal{F}_{hub})T}\mathbf{v}_{G_{p,i}}^{(\mathcal{F}_{hub})})}_{\text{Translational}} + \underbrace{\frac{1}{2}\boldsymbol{\omega}_{G_{p,i}}^{(\mathcal{F}_{p,i})T}\mathbf{J}_p\boldsymbol{\omega}_{G_{p,i}}^{(\mathcal{F}_{p,i})}}_{\text{Rotational}} \tag{2.34}$$

2.3.2.2 Elastic Potential Energy (U)

Neglecting the gravitational potential energy, the system's potential energy consists exclusively of the elastic strain energy accumulated in the virtual springs that model the flexibility. Since the Hub is rigid, the contribution comes solely from the appendages:

$$\boxed{U_{tot} = \sum_{i=1}^{N_p} U_{p,i} = \sum_{i=1}^{N_p} \frac{1}{2}\mathbf{q}_{flex,i}^T\mathbf{K}_{flex}\mathbf{q}_{flex,i}} \tag{2.35}$$

where $\mathbf{K}_{flex}$ is the diagonal stiffness matrix defined in Section 2.2.3, and $\mathbf{q}_{flex,i}$ is the vector of the 6 relative deformation coordinates of the i-th panel.

2.3.2.3 Rayleigh Dissipation Function (D)

To include the effects of viscous damping in the Lagrangian model, the Rayleigh Dissipation Function (D_{tot}) is introduced. This scalar function is defined so that its derivative with respect to the generalized velocities yields the viscous damping forces assumed in the model. Given that damping acts on the relative deformation velocities ($\dot{\mathbf{q}}_{flex,i}$), it is written as:

$$\boxed{D_{tot} = \sum_{i=1}^{N_p} \frac{1}{2}\dot{\mathbf{q}}_{flex,i}^T\mathbf{C}_{flex}\dot{\mathbf{q}}_{flex,i}} \tag{2.36}$$

where $\mathbf{C}_{flex}$ is the viscous damping matrix, defined in 2.13 in Section 2.2.3.

2.3.3 Analytical Derivation of the Equation Terms

Starting from the scalar expressions for the Kinetic Energy (T_{tot}), the Potential Energy (U_{tot}) and the Dissipation Function (D_{tot}) derived in the previous section, the equations of motion are obtained by applying the Euler-Lagrange equation in vector form:

$$\boxed{\frac{d}{dt}\left(\frac{\partial \mathcal{L}}{\partial \dot{\mathbf{q}}}\right) - \frac{\partial \mathcal{L}}{\partial \mathbf{q}} + \frac{\partial D_{tot}}{\partial \dot{\mathbf{q}}} = \boldsymbol{\tau}_{ext}} \tag{2.37}$$

where the Lagrangian is defined as:

$$\boxed{\mathcal{L} = T_{tot}(\mathbf{q}, \dot{\mathbf{q}}) - U_{tot}(\mathbf{q})} \tag{2.38}$$

Since the potential energy U_{tot} depends only on the coordinates $\mathbf{q}_{flex}$ and the kinetic energy T_{tot} is a quadratic form in generalized velocities, the equation can be expanded into its constitutive terms. The following sections detail the analytical procedure implemented in the *MATLAB* symbolic computation script to extract the matrices and vectors of the dynamic model (Eq. 2.22).

Mass Matrix ($M(q)$). The Mass Matrix $\mathbf{M}(\mathbf{q}) \in \mathbb{R}^{18\times 18}$ represents the generalized inertia of the system and the dynamic couplings between the rigid and flexible degrees of freedom. Since the kinetic energy is a quadratic form of the type $T = \frac{1}{2}\dot{\mathbf{q}}^T\mathbf{M}(\mathbf{q})\dot{\mathbf{q}}$, the mass matrix is obtained by calculating the Hessian of the kinetic energy with respect to the generalized velocities:

$$\mathbf{M}(\mathbf{q}) = \frac{\partial^2 T_{tot}}{\partial \dot{\mathbf{q}}^2} = \frac{\partial}{\partial \dot{\mathbf{q}}}\left(\underbrace{\frac{\partial T_{tot}}{\partial \dot{\mathbf{q}}}}_{\mathbf{p}}\right)^T \tag{2.39}$$

In the script, this step is performed in two stages to ensure numerical robustness:

1. Calculation of the generalized momentum vector $\mathbf{p} = \frac{\partial T}{\partial \dot{\mathbf{q}}} = \mathbf{M}\dot{\mathbf{q}}$;
2. Calculation of the Jacobian matrix of $\mathbf{p}$ with respect to $\dot{\mathbf{q}}$.

The resulting matrix is, by definition, symmetric ($\mathbf{M} = \mathbf{M}^T$) and positive definite. Its block structure explicitly highlights the dynamic couplings between the rigid and flexible parts:

$$\mathbf{M}(\mathbf{q}) = \begin{bmatrix} \mathbf{M}_{hub,hub}(\mathbf{q}) & \mathbf{M}_{hub,p}(\mathbf{q}) \\ \mathbf{M}_{p,hub}(\mathbf{q}) & \mathbf{M}_{p,p}(\mathbf{q}) \end{bmatrix} \tag{2.40}$$

where:

- $\mathbf{M}_{hub,hub} \in \mathbb{R}^{6\times6}$: Inertia of the central body (Hub), which includes the contribution of the mass of the panels.
- $\mathbf{M}_{p,p} \in \mathbb{R}^{12\times12}$: Generalized inertia of flexible appendages.
- $\mathbf{M}_{hub,p} = \mathbf{M}_{p,hub}^T \in \mathbb{R}^{6\times12}$: Inertial coupling blocks. These non-zero terms indicate that an acceleration of the Hub induces forces on the panels and, conversely, the vibration of the panels perturbs the motion of the Hub.

Coriolis and Centrifugal Forces Vector (h). For the calculation of convective inertial forces (Coriolis and centrifugal), a direct vector approach based on the expansion of the time derivative of momentum is adopted.

Considering the first term of the Lagrange equation:

$$\frac{d}{dt}\left(\frac{\partial T}{\partial \dot{\mathbf{q}}}\right) = \frac{d}{dt}(\mathbf{M}\dot{\mathbf{q}}) = \mathbf{M}\ddot{\mathbf{q}} + \dot{\mathbf{M}}\dot{\mathbf{q}} \tag{2.41}$$

By substituting into the general equation, terms dependent on velocities (quadratic) and position are isolated:

$$\mathbf{M}\ddot{\mathbf{q}} + \underbrace{\left(\dot{\mathbf{M}}\dot{\mathbf{q}} - \frac{\partial T}{\partial \mathbf{q}}\right)}_{\mathbf{h}(\mathbf{q},\dot{\mathbf{q}})} + \cdots = \boldsymbol{\tau} \tag{2.42}$$

The vector $\mathbf{h}(\mathbf{q}, \dot{\mathbf{q}}) \in \mathbb{R}^{18}$ is calculated in the script using the relationship:

$$\mathbf{h} = \dot{\mathbf{M}}(\mathbf{q}, \dot{\mathbf{q}}) \cdot \dot{\mathbf{q}} - \left(\frac{\partial T_{tot}}{\partial \mathbf{q}}\right)^T \tag{2.43}$$

A crucial detail of the implementation concerns the calculation of the term $\dot{\mathbf{M}}\dot{\mathbf{q}}$. Since the matrix $\mathbf{M}$ depends only on the positions $\mathbf{q}$ and not explicitly on time, its total time derivative is obtained via the *Chain Rule*:

$$\dot{\mathbf{M}} = \sum_{k=1}^{N_{dof}} \frac{\partial \mathbf{M}}{\partial q_k}\dot{q}_k \tag{2.44}$$

This algorithm allows for obtaining the exact vector $\mathbf{h}(\mathbf{q}, \dot{\mathbf{q}})$ without having to explicitly compute the complex Coriolis matrix $\mathbf{C}(\mathbf{q}, \dot{\mathbf{q}})$, drastically reducing the complexity of the symbolic expressions.

Elastic Forces Vector (K_{el}). The elastic restoring forces vector $\mathbf{k}_{el}(\mathbf{q}) \in \mathbb{R}^{18}$ derives directly from the potential energy U_{tot}. It is calculated as the gradient of the potential energy with respect to the generalized coordinates:

$$\mathbf{k}_{el}(\mathbf{q}) = \left(\frac{\partial U_{tot}}{\partial \mathbf{q}}\right)^T = \mathbf{K}_{flex}\mathbf{q} \tag{2.45}$$

Given the nature of the system (a rigid Hub free in space), the stiffness is exclusively associated with the flexible DOF. The vector takes the following form:

$$\mathbf{k}_{el}(\mathbf{q}) = \begin{bmatrix} \mathbf{0}_{6\times 1} \\ \mathbf{k}_{flex}\mathbf{q} \end{bmatrix} \in \mathbb{R}^{18} \tag{2.46}$$

Damping Matrix (C_{damp}). Finally, the viscous dissipative forces are derived from the Rayleigh Dissipation Function D_{tot} as the Hessian with respect to velocities. The damping matrix $\mathbf{C}_{damp} \in \mathbb{R}^{18\times 18}$ is obtained as:

$$\mathbf{C}_{damp} = \frac{\partial^2 D_{tot}}{\partial \dot{\mathbf{q}}^2} = \begin{bmatrix} \mathbf{0}_{6\times 6} & \mathbf{0}_{6\times 12} \\ \mathbf{0}_{12\times 6} & \mathbf{C}_{flex} \end{bmatrix} \tag{2.47}$$

Similarly to stiffness, damping only acts on the relative deformation velocities ($\mathbf{C}_{flex}$), dissipating internal vibrational energy without damping rigid-body motion.

2.3.4 Final Model Formulation

Starting from Equation 2.37, and expanding the terms:

$$\mathbf{M}(\mathbf{q})\ddot{\mathbf{q}} + \underbrace{\left(\dot{\mathbf{M}}\dot{\mathbf{q}} - \left(\frac{\partial T_{tot}}{\partial \mathbf{q}}\right)^T\right)}_{\mathbf{h}(\mathbf{q},\dot{\mathbf{q}})} + \underbrace{\frac{\partial D_{tot}}{\partial \dot{\mathbf{q}}}}_{\mathbf{C}_{damp}\dot{\mathbf{q}}} + \underbrace{\left(\frac{\partial U_{tot}}{\partial \mathbf{q}}\right)^T}_{\mathbf{k}_{el}(\mathbf{q})} = \boldsymbol{\tau}_{ext} \tag{2.48}$$

by assembling the derived terms, the final structure of the dynamic model used for simulation is obtained:

$$\underbrace{\mathbf{M}(\mathbf{q})\ddot{\mathbf{q}}}_{\substack{\text{Inertial Terms} \\ (\mathbf{M}\in\mathbb{R}^{18\times 18})}} + \underbrace{\mathbf{h}(\mathbf{q},\dot{\mathbf{q}})}_{\substack{\text{Coriolis and Centrifugal} \\ (\mathbf{h}\in\mathbb{R}^{18})}} + \underbrace{\mathbf{C}_{damp}\dot{\mathbf{q}}}_{\substack{\text{Damping} \\ (\mathbf{C}_{damp}\in\mathbb{R}^{18\times 18})}} + \underbrace{\mathbf{k}_{el}(\mathbf{q})}_{\substack{\text{Elastic Forces} \\ (\mathbf{k}_{el}\in\mathbb{R}^{18})}} = \underbrace{\boldsymbol{\tau}_{ext}}_{\substack{\text{External Forces} \\ (\in\mathbb{R}^{18})}} \tag{2.49}$$

Instantaneous acceleration $\ddot{\mathbf{q}}$ is highlighted as the result of the balance between the external forces and the sum of the inertial, the dissipative and the internal elastic forces:

$$\ddot{\mathbf{q}} = \mathbf{M}(\mathbf{q})^{-1}\left(\boldsymbol{\tau}_{ext} - \mathbf{h}(\mathbf{q},\dot{\mathbf{q}}) - \mathbf{C}_{damp}\dot{\mathbf{q}} - \mathbf{k}_{el}(\mathbf{q})\right) \tag{2.50}$$

This mathematical formulation reflects the physical architecture of the system shown in Figure 2.4, where the force flows and the coupling terms linking the Hub dynamics (Rigid Motion) to the Panel dynamics (Elastic Vibrations) are highlighted.

In detail, the red arrows on the left represent the inputs received by the system in terms of torques, namely τ_{ctrl} and τ_{dist}, while the blue arrow represents $[\mathbf{q}_{hub}, \dot{\mathbf{q}}_{hub}]$, which is the

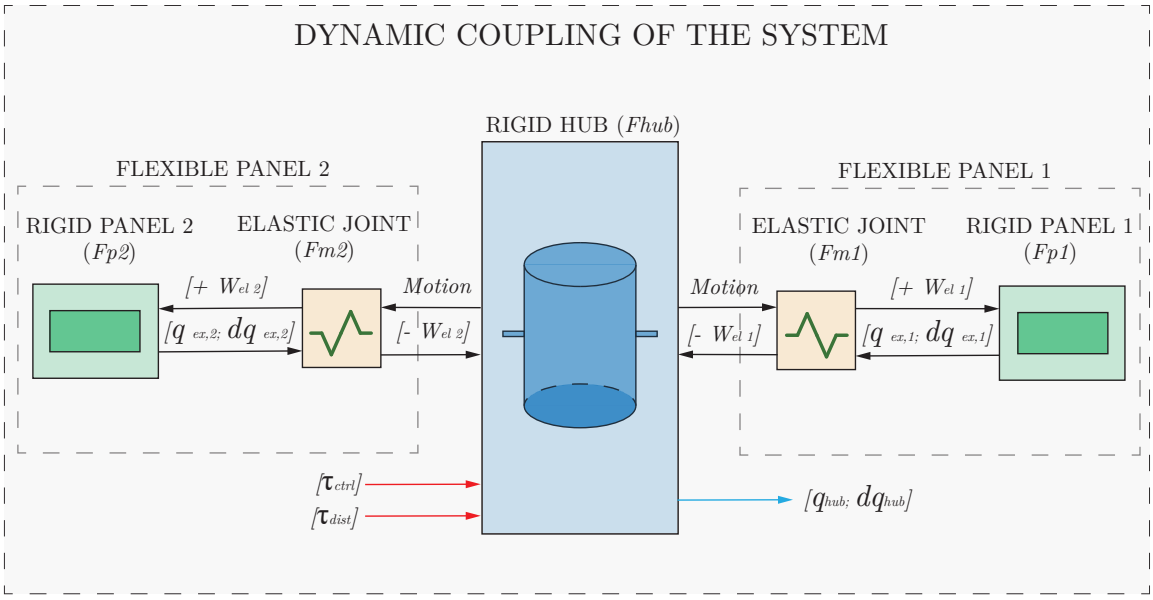

Figure 2.4: Block diagram of the dynamic couplings of the Hub-Panels system (Dynamic Coupling).

state of the central rigid body, the output of the system. The motion of the rigid central body (Hub) dynamically excites the attachment point of the panel. The elastic joint, by deforming, generates a reaction wrench $\mathbf{W}_{el} = [\mathbf{F}_{el}^T, \boldsymbol{\tau}_{el}^T]^T \in \mathbb{R}^6$ that acts in two opposite directions according to the principle of action and reaction: it transmits forces and torques to the rigid panel, tending to return it toward the undeformed equilibrium configuration, and exerts an equal and opposite action on the Hub, perturbing its attitude. This instantaneous feedback mechanism, combined with inertial effects, constitutes the Dynamic Coupling between the rigid and flexible degrees of freedom.

Chapter 3

Case Study Definition and Model Validation

Contents

3.1 Definition of the Nominal Case Study 27
3.1.1 Central Hub Characteristics 28
3.1.2 Flexible Appendages Characteristics 28
3.1.3 Coupled Model Characteristics 29
3.2 Modal Analysis of the Coupled System 31
3.2.1 Foundations of Modal Analysis 31
3.2.2 Modal Analysis Results 33
3.3 Open-Loop Dynamic Validation 38
3.3.1 Simulation Setup 39
3.3.2 Results Analysis 41

This chapter defines the nominal case study to be addressed using the mathematical model derived in Chapter 2. It then proceeds with a description of the inertial and geometric properties of the case study. Finally, the accuracy of the mathematical model is evaluated by modal analysis of the coupled system, and the CSI interaction is studied by means of an Open-Loop validation, carried out by subjecting the satellite to the action of an external torque time profile $\boldsymbol{\tau}_{ext}$.

3.1 Definition of the Nominal Case Study

This section defines the numerical characteristics of the nominal case study: a Light-class satellite platform (total mass of approximately 160 kg) equipped with extended and markedly flexible solar appendages. The configuration has been conceived following specific design guidelines to recreate a critical operational scenario for the Attitude Determination and Control System (ADCS). In particular, it was chosen to impose an appendage inertia comparable to that of the central body and natural frequencies sufficiently low to induce large elastic deformations, thus making high energy dissipation essential.

The entire initialization procedure is automated using the script `N02 _Step1 _CompleteModel _Setup.m`. The code is also integrated with graphic routines dedicated to visual validation, such as `visualize _inertia _and _axes.m` to represent the principal axes of inertia and `animate_mode.m` to animate the mode shapes. The architecture and operation of these software modules are analyzed in detail in the Appendix A.2.

The set of geometric, inertial and modal parameters that uniquely identify the resulting nominal configuration is summarized in Table 3.1.

Table 3.1: Physical and modal parameters of the nominal case study.

System	Parameter	Description	Value
Main Hub	M_{hub}	Mass	150 kg
	$\mathbf{J}_{hub} \in \mathbb{R}^{3\times3} = \begin{bmatrix} J_{hub,xx} & 0 & 0 \\ 0 & J_{hub,yy} & 0 \\ 0 & 0 & J_{hub,zz} \end{bmatrix}$	Inertia in Main Body Frame $\mathcal{F}_{hub}$ $\begin{bmatrix} 41.6 & 0 & 0 \\ & 41.6 & 0 \\ & & 27.0 \end{bmatrix}$	kg m^2
	R_{hub}	Radius	0.6 m
	H_{hub}	Length	1.5 m
	$\mathbf{d}_{offset}$	Connection arm length	0.2 m
	$\mathbf{r}_{m,i}$	Panel attachment point	0.8 m
Flexible appendages	M_p	Single panel mass	6.75 kg
	$\mathbf{J}_p \in \mathbb{R}^{3\times3} = \begin{bmatrix} J_{p,xx} & 0 & 0 \\ 0 & J_{p,yy} & 0 \\ 0 & 0 & J_{p,zz} \end{bmatrix}$	Inertia in Panel Frame $\mathcal{F}_{p,i}$ $\begin{bmatrix} 11.4 & 0 & 0 \\ & 1.3 & 0 \\ & & 12.7 \end{bmatrix}$	kg m^2
	$[\mathbf{f}_{n,Flapping};\ \mathbf{f}_{n,In-Plane\ bending};\ \mathbf{f}_{n,Torsional};\ \mathbf{f}_{n,Translational}]$	Flexible mode frequencies of the panel	[0.25; 0.50; 0.80; 50] Hz
	ζ	Viscous damping coefficient	0.005
	α_{sadm}	Nominal Orientation of $\mathcal{F}_{m,i}$ & $\mathcal{F}_{p,i}$	0°

3.1.1 Central Hub Characteristics

The Hub represents the satellite bus and is modeled as a homogeneous rigid cylindrical body. The geometric dimensions (R_{hub}, H_{hub}) have been sized to accommodate a hypothetical payload and the avionics onboard. A mass M_{hub} is assigned and the inertia tensor $\mathbf{J}_{hub}$ is calculated assuming a uniform mass distribution.

3.1.2 Flexible Appendages Characteristics

The solar panels are identical and mounted symmetrically with respect to the central body. Each panel is modeled as a rigid rectangular plate of length L_p and width W_p. An areal density ρ_{sup} is assumed and the mass M_p is derived. The inertia tensor $\mathbf{J}_p$ is calculated with respect to the panel's own center of mass, in Frame $\mathcal{F}_p$. The geometric and inertial properties of the flexible appendages are shown in Table 3.1.

3.1.3 Coupled Model Characteristics

The union of the subsystems defined in the previous paragraphs leads to the definition of the global mass matrix of the system $\mathbf{M}(\mathbf{q}_0) \in \mathbb{R}^{18\times 18}$, evaluated in the non-deformed nominal configuration. This matrix represents the generalized inertia of the system and contains all the information regarding the mass distribution, geometry, and, above all, the dynamic couplings between the degrees of freedom.

The matrix features a symmetric block structure, where the contributions of the central body, the appendages, and the interaction terms can be clearly distinguished:

$$\mathbf{M}(\mathbf{0}) = \left[\begin{array}{c|c|c} \mathbf{M}_{hub}^{agg} & \mathbf{M}_{hub,p_1} & \mathbf{M}_{hub,p_2} \\ \hline \mathbf{M}_{hub,p_1}^T & \mathbf{M}_{p_1} & \mathbf{0} \\ \hline \mathbf{M}_{hub,p_2}^T & \mathbf{0} & \mathbf{M}_{p_2} \end{array}\right] \tag{3.1}$$

where $\mathbf{M}_{hub}^{agg}$ is the "aggregated" Hub inertia, i.e., augmented by the presence of the panels, $\mathbf{M}_{p_i}$ is the local mass matrix of the i-th panel, and $\mathbf{M}_{hub,p_i}$ contains the inertial coupling terms. The numerical values of the mass matrix evaluated in the undeformed configuration are reported in the Appendix B.

The physical meaning of the constituent blocks is analyzed in the following ways:

Aggregated Hub block $\mathbf{M}_{(1:6,1:6)}$. This block describes the inertia of the central body with the additive terms imposed by the appendages, considered as connected rigid bodies. The elements of the first diagonal block ($\mathbf{M}_{(1:3,1:3)} = 163.5$ kg) correspond exactly to the total mass of the satellite: $M_{tot} = M_{hub} + 2 \cdot M_p = 150 + 2 \cdot 6.75 = 163.5$ kg. The elements of the second diagonal block ($\mathbf{M}_{(4:6,4:6)}$) include the proper rotational inertia of the hub added to the transport contributions of the parallel axis of the two panels. Since the panels are far from the rotation axis, the total inertia increases significantly.

Local panel block $\mathbf{M}_{(7:12,7:12)}$. This 6×6 block represents the mass matrix of the panel (P1) calculated with respect to the hinge point rather than the center of mass. The diagonal terms of this matrix are fundamental and represent the effective rotational inertia seen by the joint. The terms $M_{(10,10)} \approx 45.56$ kg m^2, $M_{(11,11)} \approx 1.26$ kg m^2, $M_{(12,12)} \approx 46.83$ kg m^2 are, respectively, the effective rotational inertias about the reference axes. Applying the Huygens-Steiner theorem (parallel axis theorem), these values are the sum of barycentric inertia and the transport of the panel mass concentrated at a distance of $L_p/2$. These are the inertia values that the rotational spring must counteract, and on these values the stiffness $k_{r,i}$ will be tuned. Within the panel block, non-zero off-diagonal terms also appear. These represent the coupling between local translation and rotation due to the fact that the panel's center of mass does not coincide with the hinge point. The value 15.19 corresponds exactly to the static moment (first moment of mass) of the panel with respect to the hinge ($S = M_p \cdot d_{CG} = 6.75 \cdot 2.25 \approx 15.19$ kg m).

Dynamic coupling terms. The off-diagonal blocks $\mathbf{M}_{hub,p}$ are responsible for the interaction between the Hub and the Panels. The term $M_{(4,10)} \approx 15.19$ couples the rotation of the Hub on the X-axis with the rotation of the panel on the hinge. The value coincides with the static moment calculated above. This implies that an angular acceleration of the Hub generates an inertial force on the panel's center of mass which, having a lever arm with respect to the hinge, translates into a torque that excites the flapping mode. The term $M_{(6,12)} \approx 58.98$ highlights the strong coupling on the Z-axis. The high value indicates that yaw maneuvers transfer a large amount of kinetic energy to the in-plane vibration mode of the panel, which makes this axis particularly critical for control.

The analysis of this matrix lays the foundation for the subsequent inverse tuning: knowing the exact effective inertia (the diagonal terms of the panel block, e.g., 45.56), it is possible to analytically calculate the stiffnesses required to place the natural frequencies at the desired target values.

The three-dimensional representation of the nominal case study of the modeled satellite is shown in Figure 3.1. This visualization was created using *Adobe Illustrator* software, taking the figure generated directly by the *MATLAB* scripts as a reference. In addition to the representation of the individual components, the principal axes of inertia are visible in the figure. In this specific case, the principal inertia axes coincide with the body axes of the frame $\mathcal{F}_{hub}$, since by imposing $\alpha_{sadm} = 0°$, the configuration of the coupled model is symmetric.

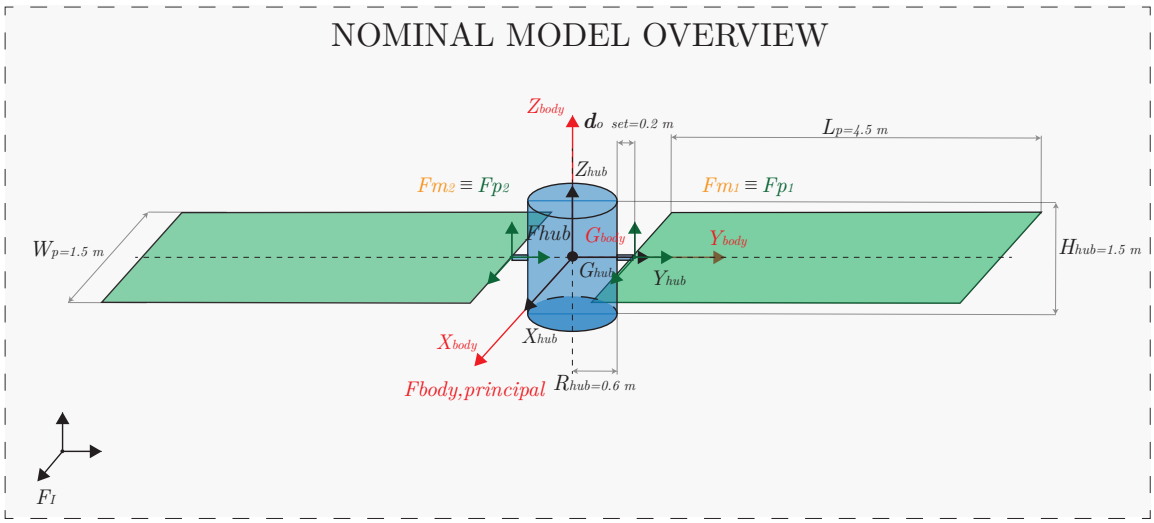

Figure 3.1: Geometric representation of the nominal case study. The principal axes are shown in red, the body axes in black, and the alignment of the frames in the initial undeformed configuration is visible, with $\alpha_{sadm} = 0°$.

3.2 Modal Analysis of the Coupled System

Before proceeding with the study of dynamics, it is necessary to validate the consistency of the model through modal analysis. As detailed in Chapter 2 (Section 2.2.3), the stiffness and damping parameters of the elastic joints are not intrinsic material properties, but derived parameters obtained through an inverse tuning procedure. The tuning of the system's stiffnesses and viscous damping involves defining the target frequencies and extracting the equivalent inertia from the global mass matrix of the system $\mathbf{M}(\mathbf{q}_0) \in \mathbb{R}^{18\times18}$. This procedure aims to assign the elastic joints a stiffness such that they replicate the natural modes of the panel in a clamped configuration. The modal analysis of the overall system then extends this verification to the coupled operational scenario, highlighting the spectral variations caused by the removal of the clamping constraint and the interaction with the rigid degrees of freedom of the central body.

3.2.1 Foundations of Modal Analysis

Modal analysis consists of studying the free vibration properties of the linearized and undamped system. Mathematically, this involves solving the generalized eigenvalue problem associated with homogeneous equations of motion:

$$\mathbf{M}(\mathbf{q}_0)\ddot{\mathbf{q}} + \mathbf{K}_{sys}\mathbf{q} = \mathbf{0} \tag{3.2}$$

Assuming a harmonic solution of the type $\mathbf{q}(t) = \boldsymbol{\phi} e^{j\omega t}$, the problem reduces to the characteristic equation:

$$\det(\mathbf{K}_{sys} - \omega^2 \mathbf{M}(\mathbf{q}_0)) = 0 \tag{3.3}$$

The solution to this equation yields two fundamental quantities for the physical understanding of the system:

- Eigenvalues ($\lambda_i = \omega_i^2$): These represent the square of the natural frequencies of the system. The natural frequencies in Hertz are given by $f_i = \sqrt{\lambda_i}/2\pi$.
- Eigenvectors ($\boldsymbol{\phi}_i$): These represent the Mode Shapes, i.e., the deformed geometric configuration that the system assumes when vibrating at that specific frequency ω_i.

Classification of modes. Since the model is described by $N = 18$ DOF, the analysis will yield 18 natural modes, which can be divided into two distinct physical categories:

1. Rigid Body Modes: Because the satellite is a free-floating system in space (unconstrained to the ground), the global stiffness matrix $\mathbf{K}_{sys}$ is singular. The first 6 eigenvalues will be zero ($f \approx 0$ Hz), corresponding to the 6 rigid body DOF of the coupled system (3 translations + 3 rotations).

2. Flexible Modes: The remaining 12 eigenvalues represent the elastic vibration modes of the coupled system (Flapping mode, Torsional mode, In-Plane Bending mode, Translational modes).

Difference between local and global frequencies. It is important to emphasize a crucial physical distinction: the target frequencies used for tuning refer to the cantilevered condition (Panel clamped to a fixed base). However, in the real system, the base of the panel is the Hub, which has a finite mass and is free to move. The inertial interaction between the Hub and the panels modifies the dynamic response, causing a Frequency Shift compared to the clamped case. The modal analysis serves precisely to quantify these new "coupled" frequencies and their associated mode shapes.

Analysis conditions and numerical implementation. The modal analysis presented in this section is conducted by linearizing the system around the undeformed equilibrium configuration ($\mathbf{q} = \mathbf{0}$) and at rest conditions ($\dot{\mathbf{q}} = \mathbf{0}, \boldsymbol{\Omega}_{hub} = \mathbf{0}$). This assumption implies the absence of gyroscopic effects or Centrifugal Stiffening/Softening terms. Although natural frequencies undergo variations during operational maneuvers ($\boldsymbol{\Omega}_{hub} \neq 0$), for the low slew rates typical of maneuvers LASM, these effects are considered second-order perturbations with respect to the fundamental dynamics analyzed here.

The numerical implementation in the *MATLAB* environment follows the logical steps described below:

1. Mass Matrix Calculation ($\mathbf{M}_0$): The mass matrix of the complete system is evaluated in the nominal configuration (fixed α_{sadm}, zero deformations).

2. Stiffness Matrix Construction ($\mathbf{K}_{sys}$): The block-diagonal global stiffness matrix is assembled:
$$\mathbf{K}_{sys} = \text{diag}\left(\mathbf{0}_{6\times6},\ \mathbf{K}_{flex,1},\ \mathbf{K}_{flex,2}\right) \tag{3.4}$$
The first 6×6 null block reflects the absence of elastic restoring forces for the absolute position and orientation of the Hub in inertial space. The subsequent blocks contain the stiffnesses $k_{t,i}, k_{r,i}$ calculated in the previously tuning phase mentioned above.

3. Eigenvalue problem Solution: Using the `eig(K, M)` function, eigenvalues and eigenvectors are extracted simultaneously, which are subsequently sorted by increasing frequency. The eigenvectors $\boldsymbol{\phi}_i$ are extracted from the eigenvector matrix $\boldsymbol{\Phi}_i$ and normalized to allow for the visualization and comparison of the modal shapes.

The numerical results of this procedure, in terms of natural frequencies and mode shape identification, are reported and discussed in the following paragraph.

3.2.2 Modal Analysis Results

This section presents the results of the eigenvalue analysis conducted on the linearized model. The objective is twofold: to verify that the natural frequencies of the coupled system are consistent with the design ones, and to identify which rigid degrees of freedom of the Hub are most influenced by the flexible dynamics.

Mode shape identification. The solution of the eigenvalue problem yields 18 vibration modes. Table 3.2 summarizes the fundamental characteristics of the identified modes, reporting the target frequency used for the tuning of the isolated panel and the shape of the mode obtained according to the approach LPA. Table 3.3 reports the frequencies of the coupled system and their respective mode shapes.

To facilitate interpretation, the modes are grouped according to the DOF they influence. It should be noted that, for the flexible modes, the coupled system presents pairs of eigenvalues that are not always very close to each other, corresponding to the symmetric and antisymmetric configurations.

Table 3.2: Classification of the predicted target mode shapes for the isolated panel.

Mode Type	**Target Frequency** (Cantilever)	**Mode Shape Visualization**
1st Bending Out-of-Plane (Flapping)	0.25 Hz	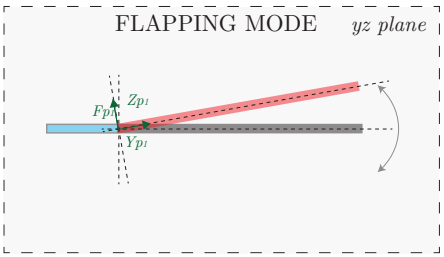 Out-of-plane bending around the X_m axis in the reference frame anchored to the panel root $\mathcal{F}_m$. The deformed configuration is indicated in red.
1st Bending In-Plane (Lead-Lag)	0.50 Hz	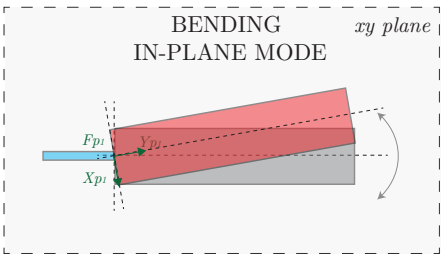 In-plane bending around the Z_m axis in the reference frame anchored to the panel root $\mathcal{F}_m$.
1st Torsional (Twisting)	0.80 Hz	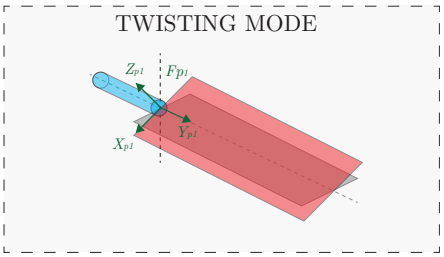 Torsion around the longitudinal Y_m axis in the reference frame anchored to the panel root $\mathcal{F}_m$.
Panel Translation (Stiff Modes)	50.0 Hz	High-frequency rigid axial modes.

Table 3.3: Classification of the mode shapes of the coupled satellite system.

Mode Type	Freq. & Type	Mode Shape Visualization
Rigid Body Modes (Modes 1-6)	0.00 Hz	The system translates and rotates as a single undeformed body.
1st Bending Out-of-Plane (Flapping mode)	Mode 7: 0.26 Hz Symmetric	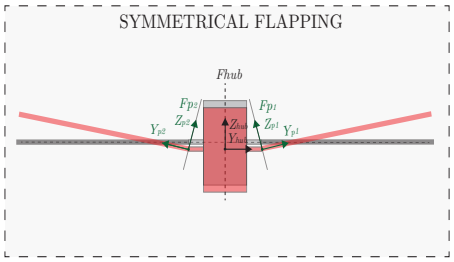 Symmetric flapping (panels bend in-phase).
	Mode 9: 0.52 Hz Asymmetric	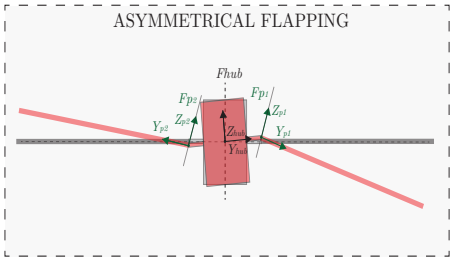 Asymmetric flapping (coupling with Hub Roll).
1st Bending In-Plane (Lead-Lag)	Mode 8: 0.52 Hz Symmetric	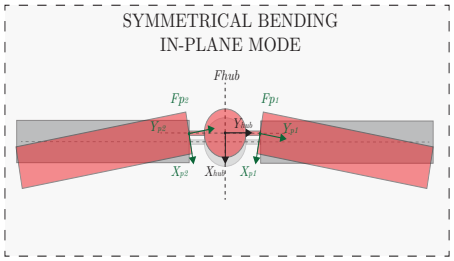 Symmetric in-plane bending.
	Mode 12: 1.23 Hz Asymmetric	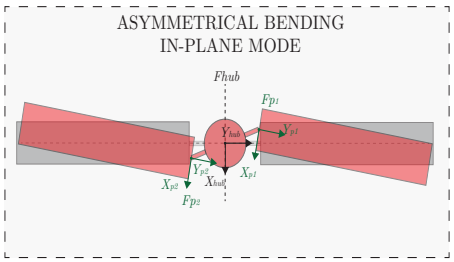 Asymmetric in-plane bending (Strong coupling with Hub Yaw).

Table 3.3 (continued): Mode shape classification.

Mode Type	Freq. & Type	Mode Shape Visualization
1st Torsional (Twisting)	Mode 10: 0.80 Hz Asymmetric	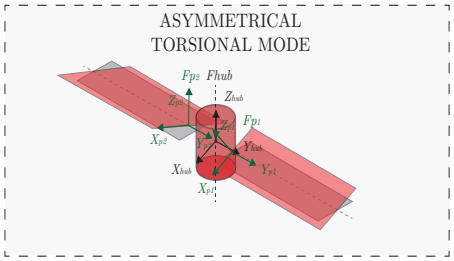 Pure asymmetric torsion.
	Mode 11: 0.82 Hz Symmetric	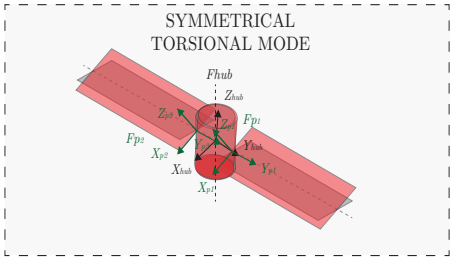 Symmetric torsion with minimal impact on the Hub.
Panel Translation (Modes 13-18)	50.0 Hz	High-frequency rigid axial modes (> 50 Hz).

Modal Interaction Map. To understand how each mode shape interacts with the motion of the central body, in addition to the mode shape drawings shown in Table 3.3, the modal interaction map is provided (Figure 3.2). This graphical matrix displays the normalized components of the eigenvectors ϕ_i. The horizontal axis shows the 18 modes ordered by frequency, while the vertical axis lists the 18 physical degrees of freedom of the system. An intense color (value 1) indicates that the specific degree of freedom participates dominantly in the corresponding vibration mode.

From the analysis of the map, some key dynamic interactions for attitude control clearly emerge.

Coupled system Flapping mode. The Flapping mode (modes 7 and 9) of the coupled satellite system presents higher frequencies compared to the target frequency of the isolated panel. The shape of the mode can be qualitatively observed in Table 3.3; Figure 3.2 shows the degrees of freedom most involved in this mode shape. Mode 7 (symmetric Flapping) implies a translational motion of the Hub along the Z_{hub} axis, whereas mode 9 (antisymmetric

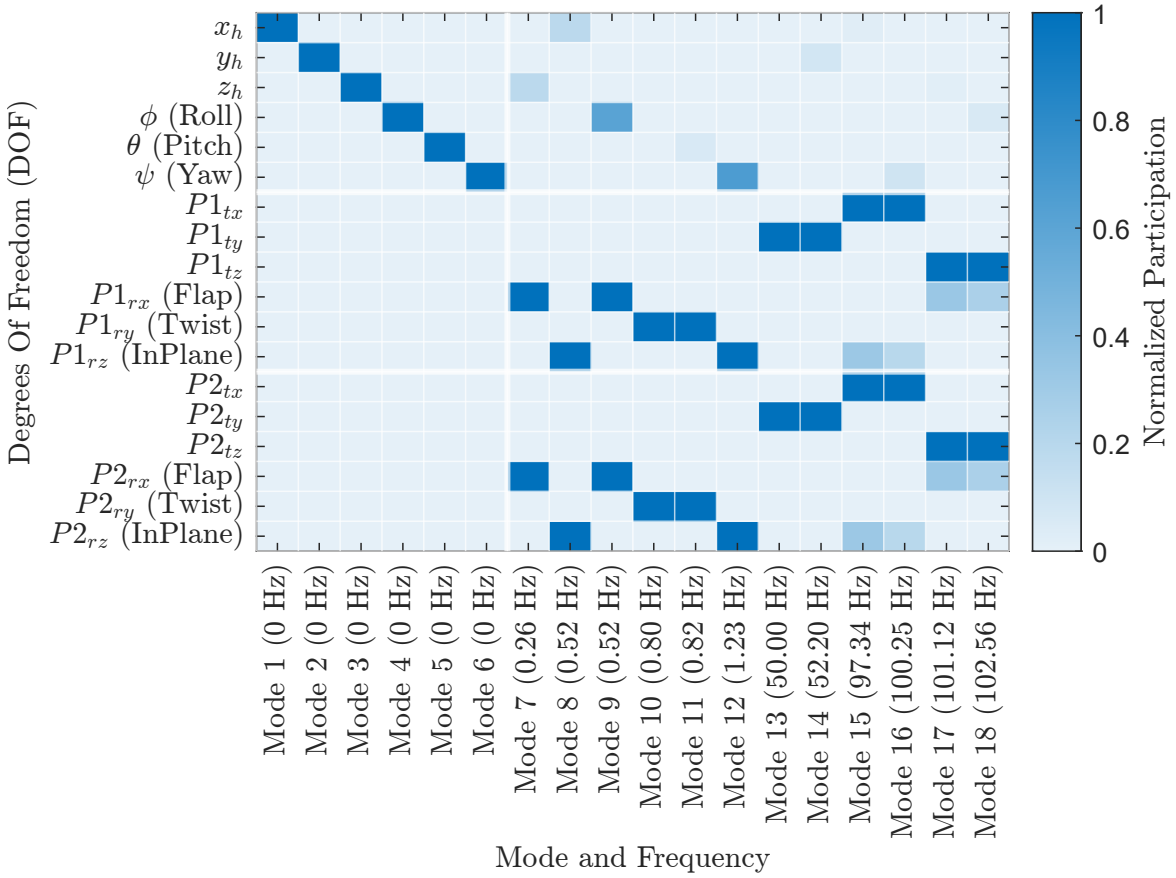

Figure 3.2: Modal Interaction Map. The matrix highlights how the flexible modes (from 7 to 18) do not solely involve the panel coordinates, but also excite the degrees of freedom of the Hub.

Flapping) implies a roll motion (ϕ) of the Hub around the X_{hub} axis. It is noted that the frequency associated with the symmetric Flapping mode shifts from 0.25 to 0.26 Hz, while the frequency associated with the antisymmetric Flapping mode shifts from 0.25 to 0.52 Hz. During antisymmetric Flapping, the effective inertia of the vibration mode drops drastically, the Hub couples more strongly with the flexible appendages, and consequently, the frequency increases.

Coupled system In-Plane Bending mode. The In-Plane Bending mode (modes 8 and 12) of the satellite system also presents higher frequencies compared to the target frequencies of the isolated panel. Mode 8 (symmetric In-Plane Bending) implies a translation of the rigid Hub along X_{hub}, while mode 12 (antisymmetric In-Plane Bending) is strongly coupled with the rotation of the Hub around the Yaw axis Z_{hub} (ψ). In this case as well, an increase in the frequencies associated with the vibration mode is evident. In particular, the frequency relative to mode 12 increases from 0.5 to 1.23 Hz, a symptom of the strong coupling between the Hub and the flexible appendages on the Yaw axis, which causes the vibration mode to see

a lower effective inertia and consequently, higher frequencies and improved energy transfer.

Coupled system Torsional mode. Finally, it is also interesting to analyze the frequencies related to the torsional mode. The frequency related to the antisymmetric torsional mode does not change and remains equal to 0.80 Hz. The frequency related to the symmetric torsional mode, on the other hand, increases slightly from 0.8 to 0.82 Hz. While in the first case, the massive Hub acts as a clamp for the torsional motion of both panels, in the second case of symmetric torsion, the panel mode couples with the Hub on the Pitch axis Y_{hub} (θ). However, the interaction is negligible and the frequency does not undergo significant variations.

From these analyzes, it is evident that the Pitch axis is the "cleanest" from the point of view of dynamic interaction, as it involves reduced inertias. The most critical axis turns out to be the Yaw axis, which is capable of involving large inertias and generating a strong coupling between the Hub and the flexible appendages. This axis represents the one where the energy exchanges between the Hub and the flexible appendages are dominant.

3.3 Open-Loop Dynamic Validation

The modal analysis conducted in the previous section provides an important linear characterization of the system around the equilibrium configuration. However, the mathematical model derived in Chapter 2 describes highly non-linear multi-body dynamics, characterized by large rigid body motions. In order to validate the robustness of the numerical simulator and verify the actual onset of CSI interaction phenomena in the time domain, this section analyzes the dynamic response of the satellite in Open-Loop.

The numerical integration of the equations of motion was assigned to a fixed-step fourth-order Runge-Kutta (RK4) scheme. The choice of the integration time step, set to $\Delta t = 0.001$ s, is the result of a rigorous compromise between computational load and dynamic fidelity, and is closely linked to the spectrum of the system's natural frequencies.

In an oscillating system, to avoid the onset of numerical instabilities or aliasing phenomena, the Nyquist-Shannon sampling theorem imposes an integration frequency at least double that of the fastest dynamics. In the model under consideration, the highest frequency modes are the axial translation modes of the panels coupled to the rigid Hub, located at $f_{max} \approx 100$ Hz (period $T_{min} = 0.01$ s). To ensure correct wave reconstruction, engineering practice requires the evaluation of at least 10-20 points per period. With $\Delta t = 10^{-3}$ s, the solver evaluates 10 samples for each oscillation of the fastest mode, and more than 800 samples per period for the dominant bending modes (e.g., Yaw mode at 1.23 Hz).

This level of time discretization offers three fundamental guaranties for the model validation:

- Prevention of spurious numerical damping: By integrating with time steps that are too

large, solvers tend to artificially attenuate the amplitude of high-frequency oscillations (a phenomenon known as numerical damping). A fine step preserves the mechanical energy exchanged during the CSI interaction intact, ensuring that the only damping observed in the graphs is the physical one (defined by the factor $\zeta = 0.005$).

- Control of the truncation error: The global error accumulated by an RK4 scheme scales according to the order $\mathcal{O}(\Delta t^4)$. Concurrent with the choice of $\Delta t = 10^{-3}$, the temporal truncation error settles on an order of magnitude proportional to 10^{-12}, guaranteeing near machine-level precision for the macro-dynamics of the satellite.
- Phenomenological completeness: The only dynamics not captured with this discretization are those with frequencies higher than 100 Hz.

The software architecture developed for the simulator validation is governed by the main script `N05 _OpenLoop _FlexModel.m`, which utilizes several auxiliary functions developed in the *MATLAB* environment for integration and force mapping. To avoid burdening the analytical discussion, the flow chart of the developed code, the complete list of accessory functions, and the architectural details of the code are reported in full in the Appendix A.3.

3.3.1 Simulation Setup

To perform a clear and rigorous validation, it is essential to isolate the dynamic phenomena. The simultaneous application of control torques on three axes would generate strong rigid gyroscopic couplings ($\boldsymbol{\omega} \times \mathbf{J}\boldsymbol{\omega}$) that would complicate the interpretation of the energy transfer towards the flexible appendages.

For this reason, it was chosen to subject the system to a step torque applied exclusively along the axis previously identified as the most critical: the Yaw axis (Z_{hub}). The satellite, initially at rest ($\mathbf{q}_0 = \mathbf{0}, \dot{\mathbf{q}}_0 = \mathbf{0}$), is excited by the following external torque profile:

$$\boldsymbol{\tau}_{cmd}(t) = \begin{cases} \begin{bmatrix} 0 & 0 & 1.0 \end{bmatrix}^T \text{ Nm} & \text{for } 0 \leq t \leq 10 \text{ s} \\ \begin{bmatrix} 0 & 0 & 0 \end{bmatrix}^T \text{ Nm} & \text{for } t > 10 \text{ s} \end{cases} \tag{3.5}$$

The logical architecture of this numerical test is summarized in the block diagram in Figure 3.3. As illustrated in the block diagram, the logical architecture of the numerical experiment is divided into three main sub-modules:

- Torque Generator: defines the time profile of the maneuver, providing the ideal control torque $\boldsymbol{\tau}_{cmd}$ on the body axes. In this validation phase, external environmental disturbances are deliberately set to zero.
- Torque Mapping: converts the vector of physical torques into the vector of generalized forces $\mathbf{Q}_{cmd}$ compatible with the Lagrangian formulation, mapping the moments onto the Euler angles through the Principle of Virtual Work.

- Non-Linear Flexible Plant: constitutes the core of the simulator. It receives the forcing inputs and numerically integrates the multi-body dynamics, outputting the entire state vector $\mathbf{x} = [\mathbf{q}^T, \dot{\mathbf{q}}^T]^T$.

The vector of generalized coordinates $\mathbf{q} \in \mathbb{R}^{18}$ is defined as $\mathbf{q} = [\mathbf{r}^T, \boldsymbol{\Theta}^T, \boldsymbol{\eta}_{p1}^T, \boldsymbol{\eta}_{p2}^T]^T$, where $\mathbf{r}$ and $\boldsymbol{\Theta} = [\phi, \theta, \psi]^T$ represent, respectively, the translation coordinates and Euler angles of the central Hub in the inertial frame, while $\boldsymbol{\eta}_{p1}, \boldsymbol{\eta}_{p2} \in \mathbb{R}^6$ group the modal degrees of freedom associated with the flexible deformations of the two solar panels.

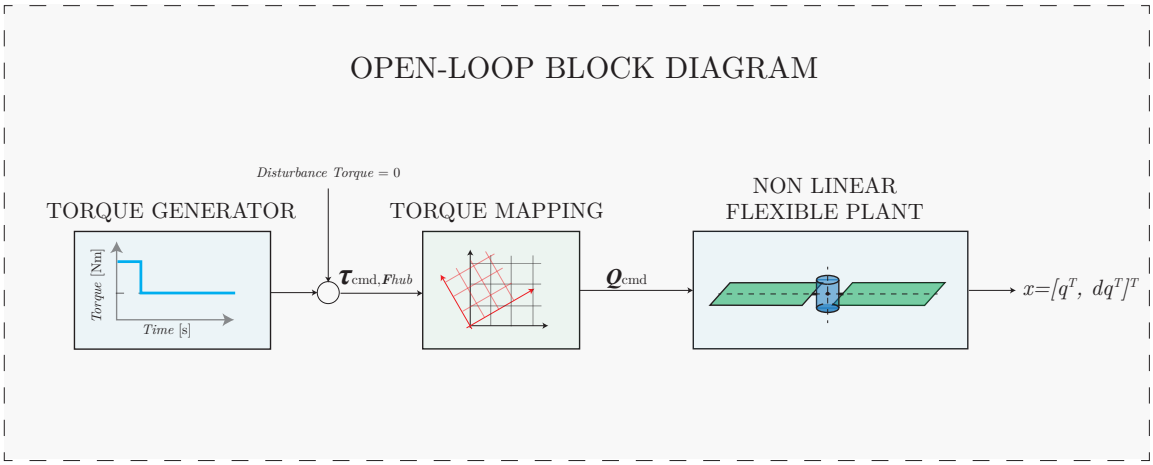

Figure 3.3: Block diagram of the Open-Loop simulation. The nominal torque profile is applied directly to the non-linear dynamic model to evaluate the free and forced response.

It should be noted that the configuration chosen for this test represents one of the simplest operational scenarios among those that can be analyzed. The angle of orientation of the panel, set to $\alpha_{sadm} = 0°$, ensures that the initial inertia matrix is symmetric and free of macroscopic products of inertia. Furthermore, the absence of external environmental disturbances and the single-axis excitation effectively cancel the onset of cross-coupled non-linear dynamics. This simplicity constitutes a specific methodological choice rather than a limitation of the validation: by eliminating external perturbations and rigid coupling terms, it is possible to verify with absolute certainty that the transverse axes remain uncoupled (as expected from theory) and isolate solely the CSI interaction induced by the mass matrix on the critical axis.

This specific test configuration allows one to evaluate the system's behavior by dividing the simulation into two distinct phases:

1. Excitation phase (0 - 10 s): The torque input injects energy into the system, rigidly accelerating the Hub and forcefully exciting the In-Plane Bending flexible modes. In this phase, it is possible to evaluate the reaction of the appendages and the onset of the flexible disturbance torque on the central body.

2. Free response phase (beyond 10 s): Once the external input is removed, the Hub proceeds at a constant angular velocity. The total mechanical energy is conserved and the

appendages oscillate freely, allowing evaluation of the structural dissipation effect and isolation of the natural vibration frequencies for a direct comparison with the results of modal analysis.

3.3.2 Results Analysis

The simulation analysis begins by observing the macroscopic quantities of the system, namely, the attitude variables and the applied torque.

Macroscopic evolution of the attitude. Figure 3.4 shows the generated control torque profile; as established in the setup, a torque step of 1 Nm is evident, limited to the first 10 s and delivered exclusively along the Yaw axis ($\tau_{cmd,z}$). The Roll and Pitch components remain identically zero for the entire duration of the simulation.

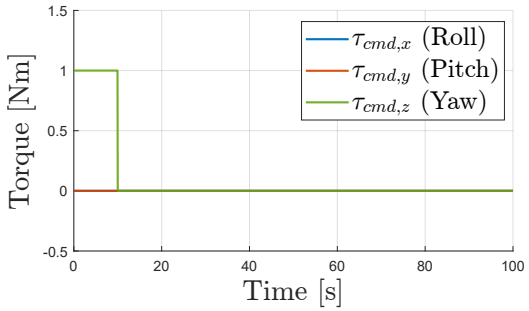

Figure 3.4: Time profile of the commanded external torque ($\boldsymbol{\tau}_{cmd}$) in Open-Loop. The impulse exclusively excites the yaw axis.

Subjected to this forcing input, the satellite begins to rotate in space. The evolution of the attitude is represented both in terms of Euler angles (Figure 3.5) and quaternions (Figure 3.6). Observing the yaw angle (ψ), the two phases of the maneuver can be clearly recognized: in the first 10 seconds, under the action of the constant torque, the angle grows with a parabolic trend (constant angular acceleration phase); at the end of the step command, the angle assumes a purely linear trend, indicating a rotation at a constant angular velocity during the free response phase. The discontinuity visible in the graph is solely due to the mathematical wrapping of the angle between +180° and -180°, which allows for a better visualization of the central body's dynamics when it completes multiple full rotations. The roll and pitch components, macroscopically, remain unchanged.

The same behavior is captured in a more elegant and singularity-free manner by the unit quaternions. Since the rotation is predominantly confined around the local Z-axis, the vector components q_1 and q_2 (corresponding to the X and Y axes) remain zero throughout the simulation. In contrast, the scalar component q_0 and the vector component q_3 evolve, describing a profile typical of a continuous rotation around a single axis of rotation.

From a preliminary, purely kinematic, and positional evaluation, the satellite would

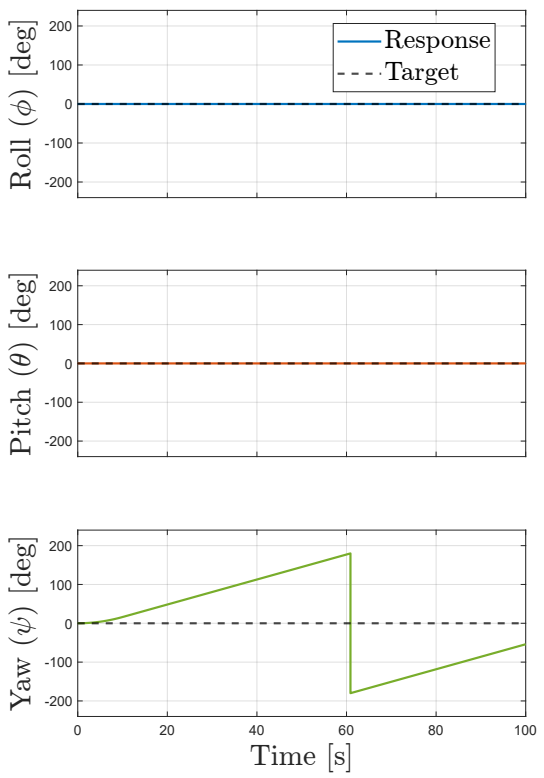

Figure 3.5: Time evolution of Euler angles. Discontinuities at ±180° are due to wrapping.

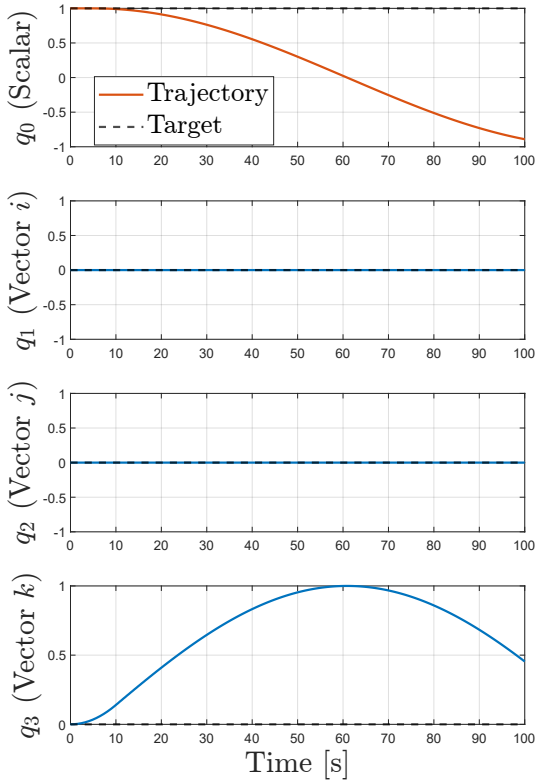

Figure 3.6: Time evolution of the quaternion. Only the q_0 and q_3 components relative to the Z-axis are active.

seem to behave as a perfect rigid body, completing the rotation in a seemingly smooth and perturbation-free manner.

Hub Kinematics and Control-Structure Interaction. The absence of visible anomalies on the global attitude is due to the fact that mathematical integration acts as a natural low-pass filter, masking the high-frequency vibratory dynamics. Only by shifting the focus and analyzing the angular velocities and accelerations of the Hub emerges the effects of the Control-Structure Interaction (CSI) unequivocally.

As highlighted by the graphs in Figures 3.7 and 3.8, the dynamics is strongly dominated by the response on the yaw axis, while perturbations on the transverse axes (roll and pitch) remain within negligible numerical tolerances (on the order of 10^{-3} deg/s).

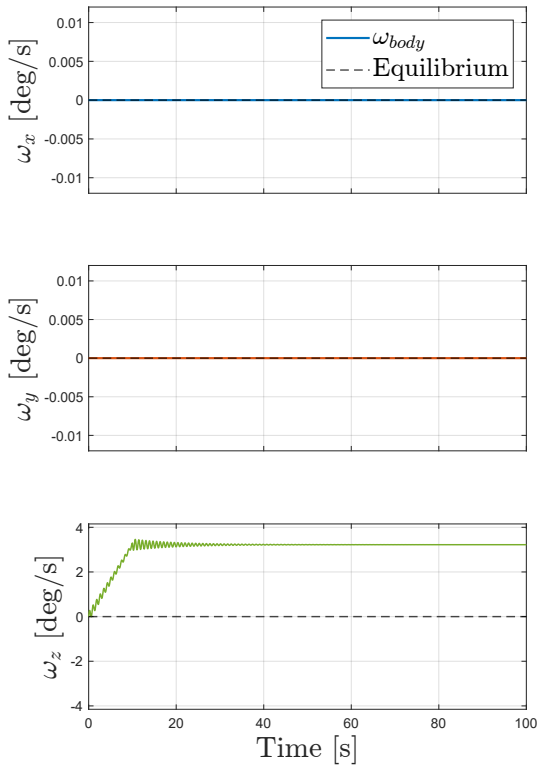

Figure 3.7: Time evolution of the angular velocities ($\boldsymbol{\omega}$). A linear macro-dynamic is noted, upon which an oscillatory *ripple* induced by the flexible panels is superimposed.

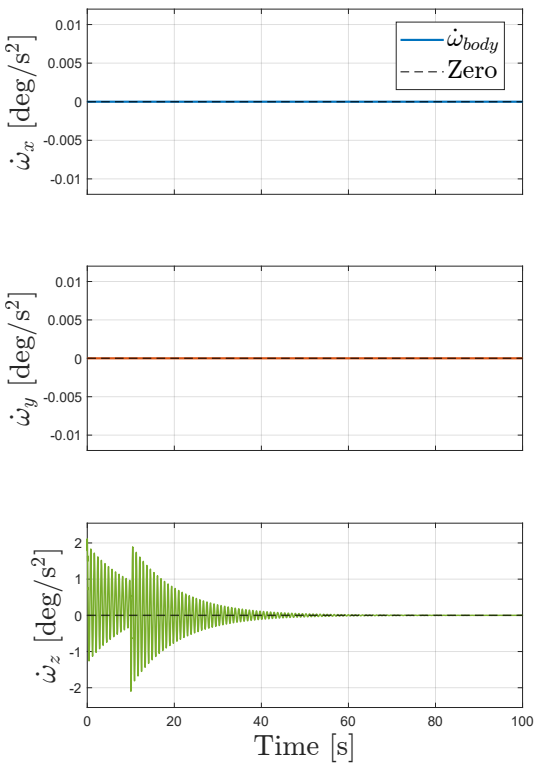

Figure 3.8: Time evolution of the angular accelerations ($\dot{\boldsymbol{\omega}}$). The violent vibrations highlight the direct exchange of reactive torques between the appendages and the Hub.

The theoretical response of a purely rigid body subjected to a rectangular torque pulse would produce a perfect step acceleration (constant from 0 to 10 s and zero thereafter) and a linear ramp angular velocity (up to reaching a free response velocity of about 3.2 deg/s). In the present case, the angular acceleration (Figure 3.8) instead assumes the appearance of a dense oscillatory envelope, with peaks reaching ± 2 deg/s^2.

This phenomenon finds its explanation in the purely physical nature of the coupled system: when the actuator pushes the Hub, the flexible appendages, due to their own inertia, bend in the opposite direction to the motion. By deforming, they act as enormous torsional springs being loaded. Once loaded, they begin to vibrate. During this vibration, the hinges at the roots of the panels transmit an elastic reaction torque directly to the Hub. Consequently, the central body does not solely experience the thrust profile imposed by the actuators but simultaneously receives the continuous elastic "tugs" of the oscillating panels. The incessant balance between the torque applied by the actuators and the structural reaction is exactly what generates the high-frequency jitter visible on the acceleration.

It is also of fundamental importance to observe the evolution of this phenomenon in the time domain. During the first 10 s, the vibration occurs under the action of a constant torque profile around a non-zero mean deformation. When the actuator is turned off at $t = 10$ s, the external forcing vanishes: a second oscillatory envelope begins, this time in a regime of damped free vibration.

The extinction of these residual oscillations allows for a quantitative validation of the effect of structural damping introduced in the analytical model ($\zeta = 0.005$). Although the global multibody mathematical model is highly non-linear, during the free response phase two fundamental conditions are met: the deformation amplitudes of the appendages are small enough to remain in the linear elastic range, and the steady-state angular velocity of the satellite (≈ 3.2 deg/s) is so contained that the non-linear effects related to Coriolis forces are entirely negligible.

In this local regime, the flexible subsystem behaves, to all intents and purposes, as a second-order linear oscillator. Noting that the impulse on the Z-axis primarily excites the asymmetric In-Plane Bending mode, whose natural frequency from the coupled model is $f_n \approx 1.23$ Hz (circular frequency $\omega_n = 2\pi f_n \approx 7.73$ rad/s), it is legitimate to analytically estimate the time constant of the exponential decay:

$$\tau_{decay} = \frac{1}{\zeta \omega_n} = \frac{1}{0.005 \cdot 7.73} \approx 25.9 \text{ s} \tag{3.6}$$

The classical theory of linear system dynamics prescribes that a transient is almost completely extinguished after about four time constants ($t_{settling} \approx 4\tau_{decay} \approx 103$ s). Observing the graph in Figure 3.8, there is full visual and numerical confirmation of this analytical estimate: at time $t = 100$ s, or 90 s after the actuators are turned off, the acceleration amplitude has reduced almost to zero, demonstrating the absolute physical consistency of the numerical solver implemented.

To fully understand the geometry of these perturbations and confirm which specific mode shapes are responsible for this energy exchange, it is essential to shift the focus from the Central Hub to the local variables of the appendages.

Structural response and appendage deformation. To justify the strong oscillations observed in the angular acceleration of the central body, it is necessary to analyze the local

dynamics of the flexible appendages. In the lumped parameter model (LPA), the deformation of each panel is described by a set of six degrees of freedom $\boldsymbol{\eta} \in \mathbb{R}^6$, defined with respect to the local reference frame $\mathcal{F}_m$ attached to the root of the panel.

Observing the evolution of the modal coordinates in Figure 3.9, an almost total decoupling emerges between the various vibration modes, consistent with the nature of the applied excitation. The control impulse, which being purely confined to the yaw axis (Z) of the satellite, does not excite the translational dynamics η_2, η_3 in any way and only minimally excites η_1. Similarly, the rotational degrees of freedom of Flapping (η_4) and Torsion (η_5) remain inactive. The only coordinate that actively participates in the energy exchange is η_6, which describes the in-plane bending of the panel around the local Z-axis.

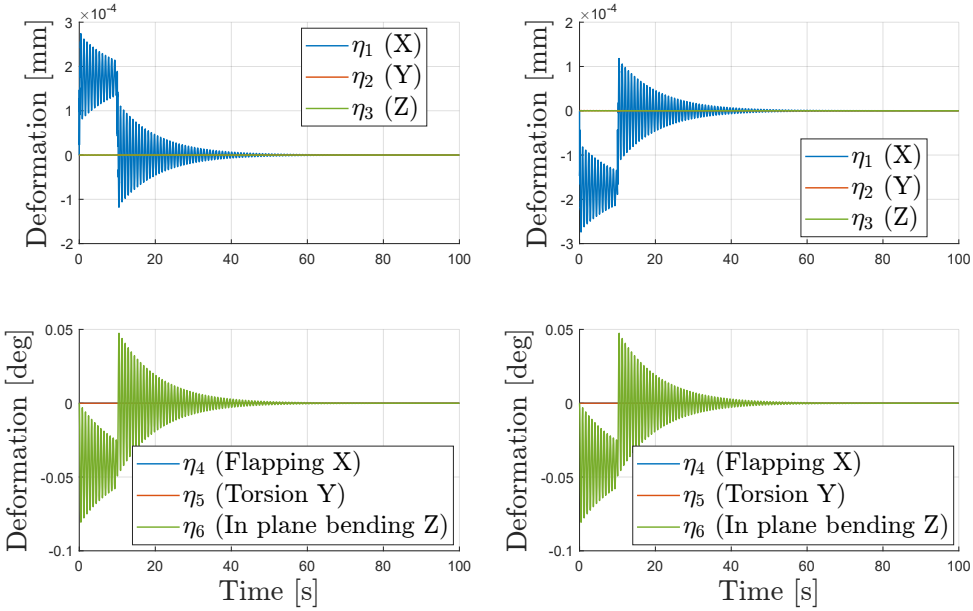

Figure 3.9: Time evolution of the modal coordinates in the local panel frame. The graphs on the left represent respectively the translational (top) and rotational (bottom) degrees of freedom of Panel 1. The right column relates to the degrees of freedom of Panel 2.

To physically quantify the extent of this deformation, the modal rotations η_i are mapped to the corresponding physical displacement at the extremities of the panels (Tip Displacement). Considering the panel as a rigid body hinged at its root, the maximum linear displacement induced by the in-plane bending is derived trigonometrically as:

$$\Delta_{tip,InPlane}(t) = \pm L_p \sin(\eta_6(t)) \tag{3.7}$$

where $L_p = 4.5$ m is the length of the panel, and the sign depends on the orientation of the local frame $\mathcal{F}_m$ with respect to the Hub's frame. Please refer to Figure 2.1 for the orientation of the reference frames. The time history of the tip displacements is shown in Figure 3.10. During the thrust phase ($0 \leq t \leq 10$ s), the degree of freedom η_6 reaches deformation peaks of almost $|0.1|^\circ$. Inserting this value into the kinematic relationship yields a physical displacement of the tip of just over 6 mm.

The visual analysis of Figure 3.10 provides a further fundamental confirmation: the deflections of the two panels have opposite signs in the local frame. Physically, since panels are mounted in opposite directions on the Hub's Y-axis, an opposite sign in the local coordinates indicates that the two appendages are bending in the same inertial spatial direction. While the Hub accelerates rotating in one direction, the panels "lag behind" due to inertia. This kinematics corresponds exactly to the antisymmetric In-Plane mode shape, already discussed and classified in the modal analysis (Mode 12, Table 3.3, frequency $f = 1.23$ Hz).

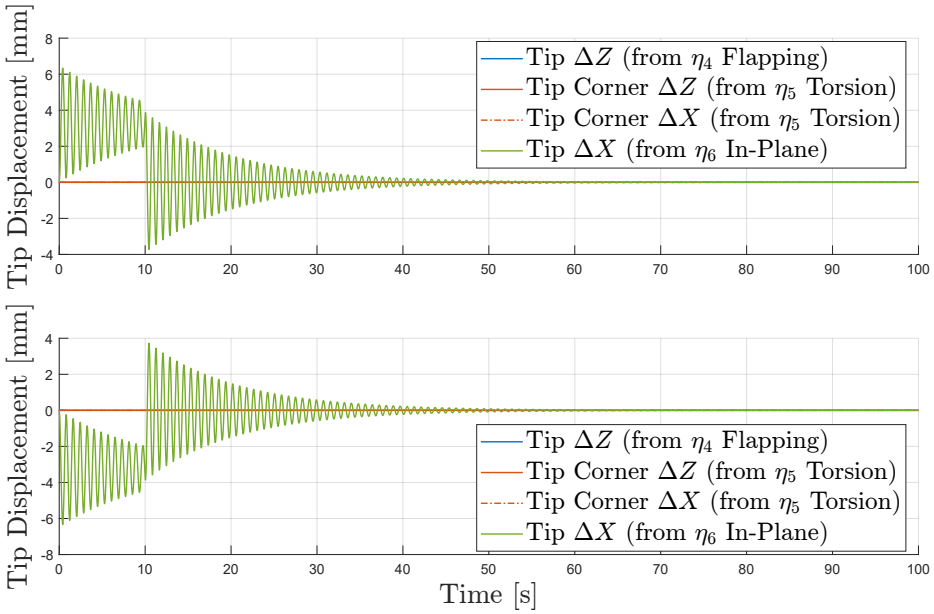

Figure 3.10: Linear displacement of the panel extremities (*Tip Displacement*). The top graph refers to Panel 1, the bottom graph refers to Panel 2. The in-plane deflection does not exceed one centimeter during the maneuver.

Structural reaction torque and CSI effect. The deflection quantified in the previous paragraph is not a mere kinematic consequence, but is the very core of CSI. By deforming the flexible joint, the panels accumulate elastic potential energy and, according to Newton's third law of motion, exert on the Hub a reaction torque equal and opposite to the stress that deformed them.

Figure 3.11 isolates and mathematically quantifies this interaction. The left column shows the disturbance vector $\boldsymbol{\tau}_{flex}$ transferred from the panels to the Hub. As expected, the reaction is zero on roll and pitch, but on the yaw axis, it generates a sinusoidal elastic torque oscillating with peak amplitudes close to ± 1.5 Nm. The disturbance torque generated solely by the structural vibration exceeds in amplitude the nominal torque itself provided by the actuator (1.0 Nm).

The impact of this phenomenon on the satellite's controllability is clearly visible in the

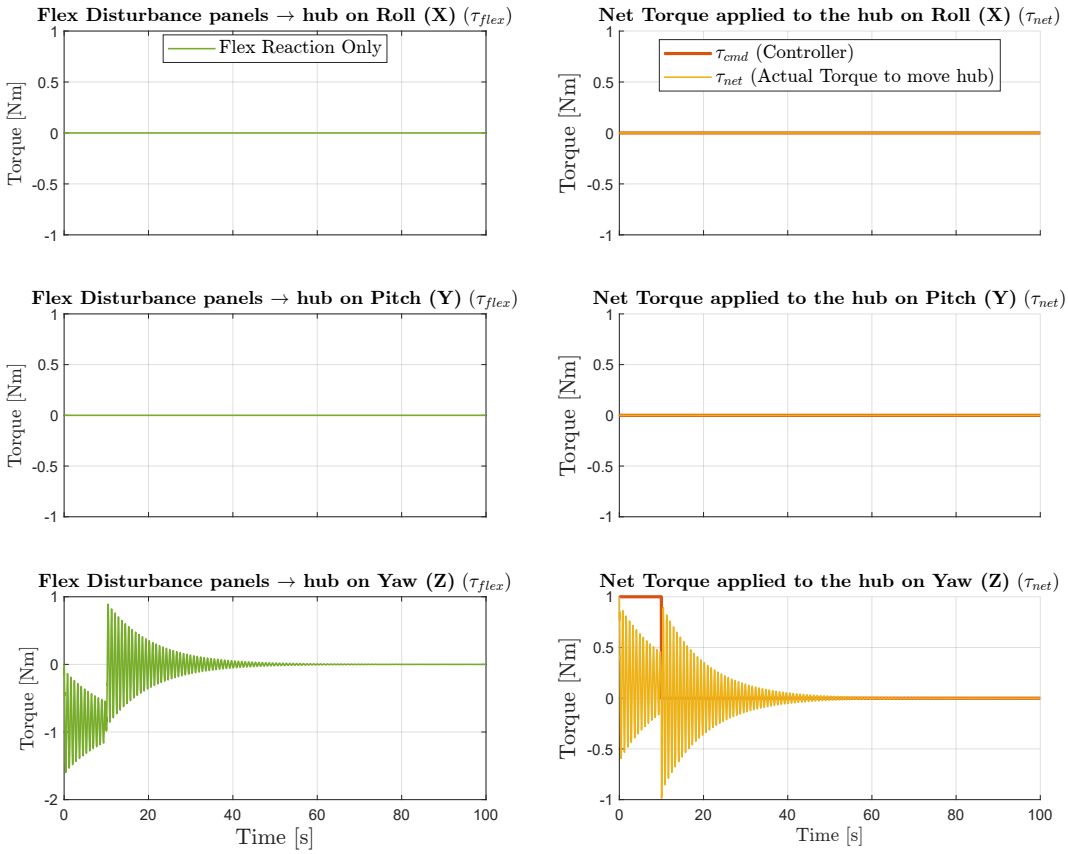

Figure 3.11: Analysis of the interaction torques. Left: the elastic reaction torques transferred from the panels to the Hub ($\boldsymbol{\tau}_{flex}$). Right: comparison between the ideal command ($\boldsymbol{\tau}_{cmd}$) and the net torque actually responsible for the central body's acceleration ($\boldsymbol{\tau}_{net}$).

right column of the same figure, where the total moment balance is plotted:

$$\boldsymbol{\tau}_{net}(t) = \boldsymbol{\tau}_{cmd}(t) + \boldsymbol{\tau}_{flex}(t) \tag{3.8}$$

The net torque $\boldsymbol{\tau}_{net}$, which represents the forcing term determining the actual acceleration of the Hub ($\mathbf{J}_{hub}\dot{\boldsymbol{\omega}} + \boldsymbol{\omega} \times (\mathbf{J}_{hub}\boldsymbol{\omega})$), is deeply "polluted" by the flexible contribution. Instead of commanding a constant rectangular torque pulse, the actuator finds itself pushing a dynamic load that varies tens of times per second, temporarily altering the effectiveness of the maneuver and fully justifying the violent vibrations found on the angular acceleration. At the initial instant ($t = 0$), all the torque commanded $\boldsymbol{\tau}_{cmd}$ is used to move the hub, but immediately after ($t = t_0 + \Delta t$), the panels begin to brake the central Hub. The dynamic coupling turns out to be in line with what was qualitatively described in Figure 2.4 in Chapter 2.

Energy validation of the model. The numerical simulation of complex multi-body systems is frequently subject to the accumulation of integration errors, which can manifest in the form of energy drifts. To definitively validate the correctness of the Lagrangian model and the RK4 integration scheme, it is very important to verify that the system respects the fundamental principles of conservation of angular momentum and mechanical energy.

Since the satellite is a free-floating system in space, the variation of its **total angular momentum** must exactly be equal to the time integral of the applied external torque. Given a constant torque $\tau_z = 1.0$ Nm applied for $t = 10$ s, the expected final angular momentum along the yaw axis is trivially derived as:

$$H_{z,target} = \int_{t=0}^{t=10} \tau_z dt = 10 \text{ Nms} \tag{3.9}$$

Figure 3.12 fully confirms this balance. The roll and pitch components remain strictly zero, while the H_z component grows following the linear ramp and then stabilizes at a value of 10 Nms during the free response phase.

It is essential to analyze the evident oscillatory ripple superimposed on the simulated curve during the first 30 s. This phenomenon is not attributable to numerical instabilities of the integrator, but rather to a precise kinematic characteristic of coupled multi-body models. In such systems, the total angular momentum vector $\mathbf{H}_{tot}$ is defined by the global mass matrix and is the sum of two contributions:

$$\mathbf{H}_{tot} = \mathbf{J}(\boldsymbol{\eta})\boldsymbol{\omega} + \mathbf{M}_{hub,flex}(\boldsymbol{\eta})\dot{\boldsymbol{\eta}} \tag{3.10}$$

namely, the contribution related to the macro-rotation of the system with time-varying inertia, a function of the panels' deformation ($\boldsymbol{\eta}$), and the relative angular momentum deriving from the local vibration velocities of the appendages.

In the calculation of the quantity represented in Figure 3.12, in order to isolate the dynamics of the central body, only the first rotational term $\mathbf{H}_{calc} = \mathbf{J}(\boldsymbol{\eta})\boldsymbol{\omega}$ was evaluated, extracting the updated inertia tensor at each step of integration, but omitting the contribution related to

dynamic coupling $\dot{\boldsymbol{\eta}}$. Since the total angular momentum $\mathbf{H}_{tot}$ of the isolated system must be strictly conserved, every fluctuation of the internal flexible momentum (owing to the reversal of the velocity of the panels during oscillation) mathematically imposes an equal and opposite fluctuation of the rotational term. The ripple visible in the graph therefore represents the exact portion of angular momentum transiently exchanged with the flexible appendages. As structural damping extinguishes vibrations ($\dot{\boldsymbol{\eta}} \to \mathbf{0}$), the relative coupling term vanishes; the entire portion of angular momentum is transferred solely to the rigid body motion, and the simulated curve collapses onto the theoretical target of 10 Nms.

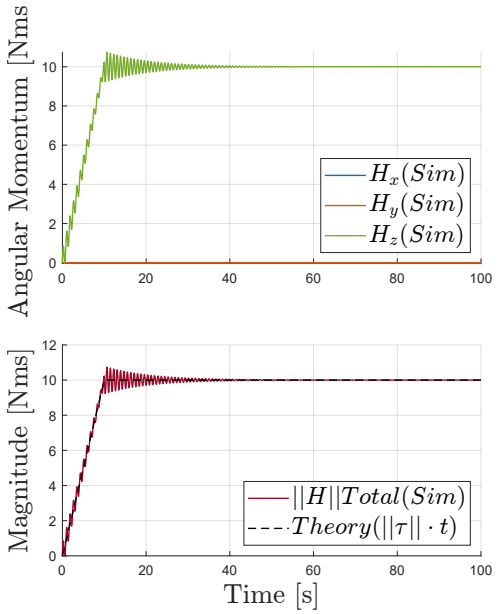

Figure 3.12: Verification of the angular momentum in body axes. The system accumulates exactly 10 Nms on the Z-axis, conserving them indefinitely in the absence of external torques. The transient ripple is a symptom of the inertial exchange with the flexible degrees of freedom.

The same analytical rigor is found when observing the **energy metrics of the system**, in Figure 3.13.

At a macroscopic level (Subplot 1), the total mechanical energy of the satellite ($E_{tot} = T + V$) grows quadratically during the maneuver, driven by the mechanical work of the actuator, reaching a steady-state value of approximately 0.28 J. Since the energy is dominated by the rigid rotation motion of the Hub, it is visually conserved intact after 10 s in the absence of applied torques $\boldsymbol{\tau}$, certifying the absence of numerical drifts in the integrator.

At a microscopic level (Subplot 2), it is possible to isolate the internal dynamics of the deformation. The elastic potential energy stored in the panels is on the order of milli-Joules (peak of ≈ 0.9 mJ). As imposed by the Rayleigh damping parameter $\zeta = 0.005$, the damping matrix $\mathbf{C}$ progressively converts this elastic energy into dissipated heat (burgundy curve). The cumulative dissipative work ($\int \dot{\boldsymbol{q}}^T \mathbf{C} \dot{\boldsymbol{q}} dt$) grows monotonically, perfectly matching the decay of the elastic potential energy and the structural vibrations, until it stabilizes at approximately 0.55 mJ. Finally, the logarithmic scale (Subplot 3) offers the definitive proof of

the linear-viscous behavior of the flexible joint around the equilibrium position: the peaks of the elastic potential energy decay following a perfect straight line, the unmistakable signature of a decreasing damped exponential envelope.

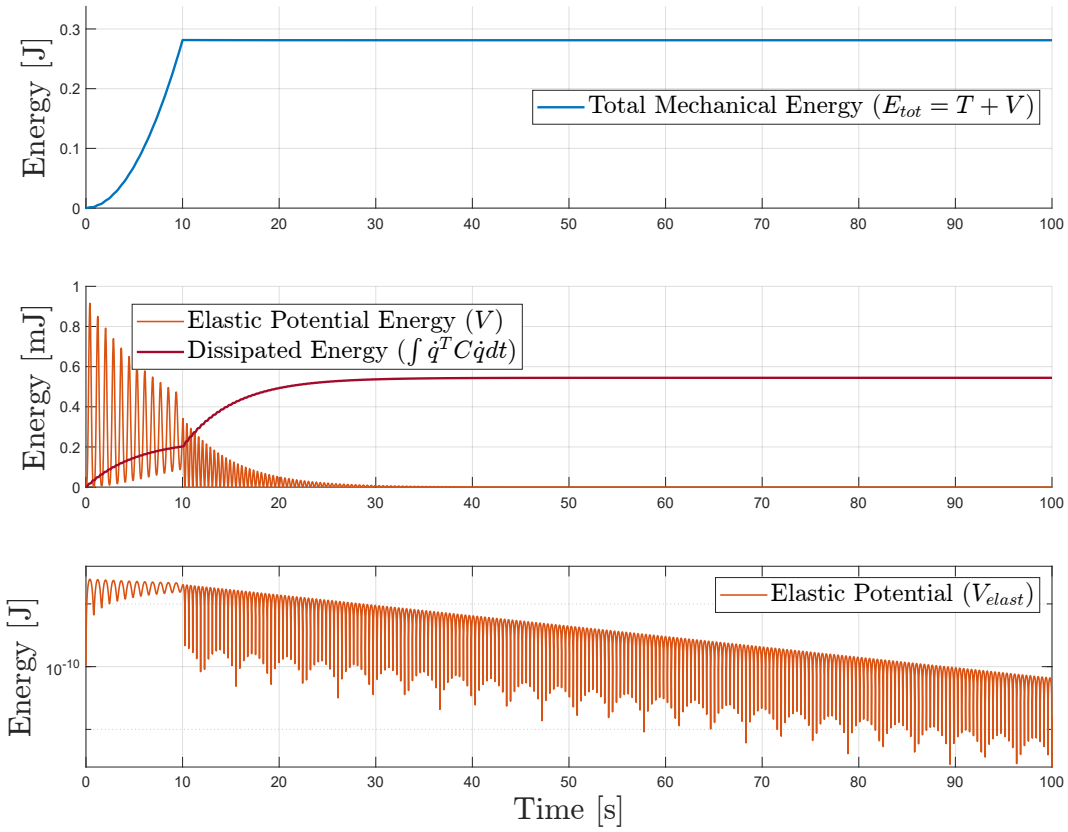

Figure 3.13: Detailed energy balance. (1) Macroscopic conservation of the total mechanical energy. (2) Microscopic dynamics of the elastic energy and its progressive structural dissipation. (3) Verification of the perfect exponential decay of the vibratory energy on a logarithmic scale.

Frequency Analysis of Dynamic Interaction. The final validation step of the Open-Loop simulator consists of verifying that the frequencies of the oscillations observed in the time domain actually correspond to the system's natural modes calculated analytically. To this end, a time-frequency analysis of the signals is conducted by calculating the Power Spectral Density (PSD) using the Short-Time Fourier Transform (STFT) algorithm.

To isolate only the vibratory content, the raw signals were previously subjected to a detrending process: by subtracting their moving average from the instantaneous signal, the macroscopic low-frequency trend attributable to the rigid body motion was removed. To ensure high sharpness in the separation of harmonics at such low frequencies, the transform was performed with a high number of points ($N_{FFT} = 65536$), ensuring an infinitesimal frequency resolution ($\Delta f \approx 0.015$ Hz).

The results of this processing are collected in the spectral response in Figure 3.14. The graphical matrix is organized by rotation axes (on the rows) and physical quantities (on the columns). The white dashed lines indicate the natural target frequencies (isolated panel in a cantilever configuration) used for the structural tuning of the isolated panel (0.25 Hz, 0.50 Hz, 0.80 Hz).

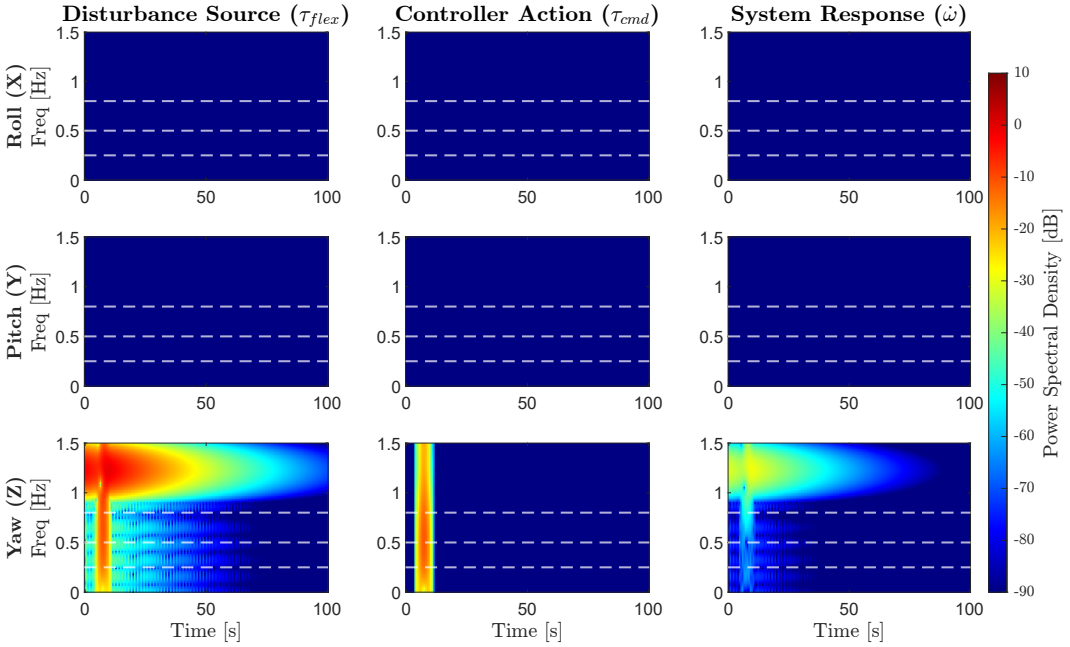

Figure 3.14: Spectrogram of the dynamic signals. The frequency is reported on the ordinate, the time on the abscissa, while the color maps the Power Spectral Density on a logarithmic scale (dB). The dynamics are confined to the yaw axis, with a clear resonance at ≈ 1.23 Hz.

From the analysis of the spectrograms, three fundamental conclusions emerge that certify the total consistency of the mathematical model:

1. Spatial decoupling: The graphs relating to the roll (X) and pitch (Y) axes do not present any spectral signature, confirming that, around the nominal configuration, an input purely confined to the yaw axis does not spuriously excite the transverse axes.

2. Disturbance causality: Focusing on the yaw row (Z), it is observed how the control action (τ_{cmd}) does not present harmonic content, being a constant step cleared of its trend (detrended). The motor injects high frequencies into the system only at the turn-on and turn-off instants at 10 s, when it brings the applied torque back to 0 Nm. In contrast, the flexible reaction torque (τ_{flex}) and the Hub's acceleration ($\dot{\omega}_z$) share the exact same spectral signature. Given that the commanded torque does not emit frequency content, all of the acceleration vibration is caused exclusively by the panels. This definitively proves that the entire ripple encountered during the integration phase is induced by the dynamic coupling term of the Lagrange equations, as justified by the following equation: $\mathbf{J}\dot{\boldsymbol{\omega}} = \boldsymbol{\tau}_{cmd} + \boldsymbol{\tau}_{flex}$.

3. Frequency Shift Validation: The high-energy band (red/yellow color) does not align with the 0.50 Hz dashed line (design frequency of the In-Plane Bending mode), but is clearly higher, centered exactly at ≈ 1.23 Hz. This result is the time-domain confirm of the dynamic coupling effect (Frequency Shift) theorized in Section 3.2: by removing the clamp at the base and allowing the Hub to rotate freely, the effective inertia seen by the antisymmetric mode drops, shifting the resonance of the free system to the higher frequencies highlighted by the eigenvalue analysis.

Finally, the chromatic gradient along the time axis provides an elegant visualization of the energy dissipated by internal friction: the intensity of the spectral line progressively degrades from its maximum values during the thrust phase, until it completely dissolves around 100 s, following the decay times predicted by the analytical model and qualitatively visualized in the time response.

Finally, the developed *MATLAB* code also includes an auxiliary function (`animate _simulation.m`) that allows generating a 3D animation of the actual motion of the satellite in the time domain, providing a visual and intuitive feedback of the Hub's macro-rotation coupled with the transient micro-vibrations of the solar panels (further operational details are available in Appendix A.3).

Chapter 4

Control Law Synthesis

Contents

4.1 Fundamentals of Sliding Mode Control 53
4.2 Adaptive Sliding Mode Control Law 55
4.2.1 Definition of Attitude Error 55
4.2.2 Sliding Surface Design 56
4.2.3 Dynamics and Control Law 56
4.2.4 Lyapunov Stability Analysis 58
4.2.5 Budget Allocation Algorithm 59

This chapter addresses the attitude control problem for the flexible satellite during rapid reorientation maneuvers (LASM). As extensively demonstrated in Chapter 3, the primary critical issue for system stability lies in the strong dynamic coupling between the central body and the flexible appendages: the accelerations imposed by the maneuver inevitably excite the vibration modes of the panels, which interact with the Hub by exerting intense internal disturbance torques (CSI).

The management of this energy exchange is further complicated by the presence of highly non-linear gyroscopic dynamics, parametric uncertainties in the model (such as variations in effective inertia or inaccurate estimates of structural stiffness), and the need to reject external environmental disturbance torques.

This chapter illustrates the synthesis of an SMC controller. Initially, a general and rigorous description of the non-linear variable structure control technique will be presented, illustrating its fundamental mathematical principles. Subsequently, the control law with adaptive parameter allocation proposed in this thesis will be derived and explained in detail.

4.1 Fundamentals of Sliding Mode Control

Sliding Mode Control (SMC) is a non-linear variable structure control technique widely used in aerospace applications due to its ease of implementation and its renowned robustness against imprecise knowledge of the system to be controlled.

The synthesis procedure is divided into two phases:

1. The definition of a Sliding Surface $\mathbf{s} = \mathbf{0}$, designed so that, when the state of the system is constrained to it, the error decays asymptotically to zero following a reduced-order dynamic.
2. The design of a Reaching Law, consisting of a discontinuous control action designed to drive the system trajectories onto the surface in finite time and keep them constrained to it.

Figure 4.1 qualitatively represents these two phases for different initial conditions of the system.

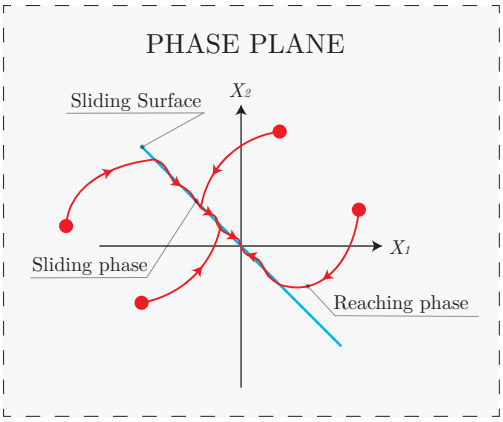

Figure 4.1: Phase plane representation of the evolution of the system under SMC action. The state trajectories (in red) converge towards the Sliding Surface (blue line) during the Reaching Phase, and then slide towards the origin during the Sliding Phase.

The existence and reachability of the surface are guaranteed by imposing Lyapunov stability. Defining a positive-definite candidate functional $V = \frac{1}{2}\mathbf{s}^T\mathbf{s}$, the control action must ensure that its time derivative is strictly negative-definite ($\dot{V} = \mathbf{s}^T\dot{\mathbf{s}} < 0$). To satisfy this condition, the Reaching Law typically assumes the form $\dot{\mathbf{s}} = -\mathbf{K}\text{sgn}(\mathbf{s})$, where $\mathbf{K}$ is a matrix of positive gains.

The chattering problem and the boundary layer. The use of the discontinuous $\text{sgn}(\cdot)$ function generates the chattering phenomenon: high-frequency oscillations of the control input when the system is in the proximity of the Sliding Surface (and therefore in the Sliding Mode condition for $\mathbf{s} = 0$). Chattering is unacceptable as it leads to actuator wear and the excitation of the flexible dynamics present in the problem considered. The standard engineering solution consists of introducing a Boundary Layer of width Φ around the surface, replacing the sign function with a continuous approximation, typically a linear saturation $\text{sat}(\mathbf{s}/\Phi)$.

The adoption of this technique eliminates the high-frequency switching, but introduces an inevitable trade-off in the choice of the Boundary Layer thickness parameter Φ. A larger Φ results in less chattering but can increase the steady-state error. Conversely, a smaller Φ can reduce the steady-state error but increase chattering.

4.2 Adaptive Sliding Mode Control Law

Control objective. The control objective consists of determining the command torque vector $\boldsymbol{\tau}_{cmd}$ such that the attitude of the satellite tracks the desired trajectory. Classical SMC formulations involve the use of constant parameters to define the slope of the Sliding Surface and the authority of the robust term. However, the use of constant gains to ensure effective tracking in maneuvers LASM does not optimize the different phases of the SMC and often leads to actuator saturation. Such saturation irreversibly degrades the theoretical stability guarantees and triggers cross-axis non-linear dynamics, exciting the vibrations of the flexible appendages and thus increasing the intensity of the disturbance torques. To overcome this critical issue, an SMC law enriched by a dynamic torque budget allocation logic is proposed. Before proceeding with the synthesis of the control law and the adaptive algorithm, the kinematic definitions of the attitude error are introduced, referencing the approach presented in [Nad+19].

4.2.1 Definition of Attitude Error

To avoid the onset of kinematic singularities typical of Euler angles during large rotations, the satellite kinematics are parameterized using unit quaternions $\mathbf{q} = [q_0, \mathbf{q}_v^T]^T \in \mathbb{R}^4$. The desired attitude is denoted by $\mathbf{q}_d = [q_{d,0}, q_{d,1}, q_{d,2}, q_{d,3}]^T$, the current attitude by $\mathbf{q} = [q_0, q_1, q_2, q_3]^T$, and the conjugate of the desired attitude by $\mathbf{q}_d^{-1} = [q_{d,0}, -q_{d,1}, -q_{d,2}, -q_{d,3}]^T$. The quaternion error $\mathbf{q}_e = [q_{0,e}, \mathbf{q}_{v,e}^T]^T$ is defined as $(\mathbf{q}_e = \mathbf{q}_d^{-1} \otimes \mathbf{q})$, which can be explicitly expressed in the following matrix form:

$$\mathbf{q}_e = \begin{bmatrix} q_{0,e} \\ q_{1,e} \\ q_{2,e} \\ q_{3,e} \end{bmatrix} = \begin{bmatrix} q_{d,0} & q_{d,1} & q_{d,2} & q_{d,3} \\ -q_{d,1} & q_{d,0} & q_{d,3} & -q_{d,2} \\ -q_{d,2} & -q_{d,3} & q_{d,0} & q_{d,1} \\ -q_{d,3} & q_{d,2} & -q_{d,1} & q_{d,0} \end{bmatrix} \begin{bmatrix} q_0 \\ q_1 \\ q_2 \\ q_3 \end{bmatrix} \tag{4.1}$$

The angular velocity error, projected into the satellite's Body reference frame, is defined as the difference between the current and the desired angular velocity:

$$\boldsymbol{\omega}_e = \boldsymbol{\omega} - \boldsymbol{\omega}_d \tag{4.2}$$

The rate of change of the vector component of the quaternion error $\dot{\mathbf{q}}_{v,e}$, necessary for the construction of the dynamics on the Sliding Surface, is governed by the following kinematic relationship, described once again in the reference paper [Nad+19]:

$$\dot{\mathbf{q}}_{v,e} = \frac{1}{2} \left(q_{0,e} \mathbf{I}_{3\times3} + \mathbf{S}(\mathbf{q}_{v,e}) \right) \boldsymbol{\omega}_e \tag{4.3}$$

where $\mathbf{I}_{3\times3}$ is the 3×3 identity matrix and $\mathbf{S}(\mathbf{q}_{v,e})$ represents the skew-symmetric matrix

associated with the vector $\mathbf{q}_{v,e} = [q_{1,e}, q_{2,e}, q_{3,e}]^T$, explicitly given as:

$$\mathbf{S}(\mathbf{q}_{v,e}) = \begin{bmatrix} 0 & -q_{3,e} & q_{2,e} \\ q_{3,e} & 0 & -q_{1,e} \\ -q_{2,e} & q_{1,e} & 0 \end{bmatrix} \tag{4.4}$$

4.2.2 Sliding Surface Design

The objective of the control law consists of forcing the error dynamics onto a mathematical surface that guaranties its asymptotic convergence to zero. The Sliding Surface $\mathbf{s} \in \mathbb{R}^3$ is designed by linearly coupling the angular velocity error with the vector component of the quaternion error, as indicated in [Nad+19]:

$$\mathbf{s} = \boldsymbol{\omega}_e + \Lambda_{act}(t)\mathbf{q}_{v,e} \tag{4.5}$$

When the system is in Sliding Mode (the condition where $\mathbf{s} = \mathbf{0}$), the error follows the following first-order dynamics:

$$\boldsymbol{\omega}_e + \Lambda_{act}(t)\mathbf{q}_{v,e} = \mathbf{0} \tag{4.6}$$

The parameter $\Lambda_{act}(t) > 0$ is a scalar design parameter that guaranties the stability of the dynamic evolution of the error once in Sliding Mode and defines the speed of the error's convergence to zero. Unlike traditional SMC, in the present formulation Λ_{act} is not a fixed constant, but a time-varying parameter, modulated by the Budget Allocation algorithm to prevent actuator saturation.

4.2.3 Dynamics and Control Law

For the design of the control law, it is assumed that the panel deformation variables are neither measurable nor accessible. The controller will calculate a command torque $\boldsymbol{\tau}_{cmd}$ considering the dynamics of the satellite as if it were a single rigid body with a total inertia of J_{tot}. The rotational dynamics of the central body, under the prevailing rigid body assumption, is described by Euler's equation:

$$\mathbf{J}\dot{\boldsymbol{\omega}} + \boldsymbol{\omega} \times (\mathbf{J}\boldsymbol{\omega}) = \boldsymbol{\tau}_{cmd} + \boldsymbol{\tau}_{dist} \tag{4.7}$$

where $\mathbf{J}$ is the inertia tensor J_{tot} of the complete coupled system considered rigid, $\boldsymbol{\tau}_{cmd}$ is the control torque, and $\boldsymbol{\tau}_{dist}$ includes the external disturbance torques and reaction torques induced by the coupling CSI.

To guaranty the reachability of the surface (Reaching Phase), a dynamic of type $\dot{\mathbf{s}} = -\mathbf{K}(t)\text{sat}(\mathbf{s}/\Phi)$ is imposed, using the saturation function to mitigate chattering. Computing the time derivative of the surface (Eq. 4.5) yields:

$$\dot{\mathbf{s}} = (\dot{\boldsymbol{\omega}} - \dot{\boldsymbol{\omega}}_d) + (\Lambda_{act}(t)\dot{\mathbf{q}}_{v,e}) + (\dot{\Lambda}_{act}\mathbf{q}_{v,e}) \tag{4.8}$$

Subsequently, it is required that the actual dynamics of the sliding variable (intrinsically dependent on the control input $\boldsymbol{\tau}_{cmd}$ through acceleration $\dot{\boldsymbol{\omega}}$) match exactly the desired dynamics imposed by the Reaching Law. This yields the following fundamental identity:

$$\underbrace{(\dot{\boldsymbol{\omega}} - \dot{\boldsymbol{\omega}}_d) + (\Lambda_{act}(t)\dot{\mathbf{q}}_{v,e}) + (\dot{\Lambda}_{act}\mathbf{q}_{v,e})}_{\dot{\mathbf{s}}_{real}(\boldsymbol{\tau}_{cmd})} = \underbrace{-\mathbf{K}(t)\text{sat}\left(\frac{\mathbf{s}}{\Phi}\right)}_{\dot{\mathbf{s}}_{desired}} \tag{4.9}$$

Multiplying everything by the inertia tensor $\mathbf{J}$:

$$\mathbf{J}(\dot{\boldsymbol{\omega}} - \dot{\boldsymbol{\omega}}_d) + \mathbf{J}(\Lambda_{act}(t)\dot{\mathbf{q}}_{v,e}) + \mathbf{J}(\dot{\Lambda}_{act}\mathbf{q}_{v,e}) = -\mathbf{J}\mathbf{K}(t)\text{sat}\left(\frac{\mathbf{s}}{\Phi}\right) \tag{4.10}$$

and substituting the expression derived from Euler's equation in Eq. 4.7 into the left-hand side, the following is obtained:

$$\boldsymbol{\tau}_{cmd} - (\boldsymbol{\omega} \times (\mathbf{J}\boldsymbol{\omega})) - (\mathbf{J}\dot{\boldsymbol{\omega}}_d) + \mathbf{J}(\Lambda_{act}(t)\dot{\mathbf{q}}_{v,e}) + \mathbf{J}(\dot{\Lambda}_{act}\mathbf{q}_{v,e}) = -\mathbf{J}\mathbf{K}(t)\text{sat}\left(\frac{\mathbf{s}}{\Phi}\right) \tag{4.11}$$

Isolating the input $\boldsymbol{\tau}_{cmd}$ yields the command torque to be applied to the system:

$$\boxed{\boldsymbol{\tau}_{cmd} = \underbrace{\boldsymbol{\omega} \times (\mathbf{J}\boldsymbol{\omega})}_{\boldsymbol{\tau}_{gyro}} + \underbrace{\mathbf{J}(\dot{\boldsymbol{\omega}}_d - \Lambda_{act}(t)\dot{\mathbf{q}}_{v,e})}_{\boldsymbol{\tau}_{guide}} - \underbrace{\mathbf{J}\mathbf{K}(t)\text{sat}\left(\frac{\mathbf{s}}{\Phi}\right)}_{\boldsymbol{\tau}_{rob}} - (\mathbf{J}\dot{\Lambda}_{act}\mathbf{q}_{v,e})} \tag{4.12}$$

Assuming a constant step desired target, the terms related to the variation of the desired attitude $\dot{\mathbf{q}}_{v,d}$ and the desired angular velocity $\dot{\boldsymbol{\omega}}_d$ can be neglected, yielding:

$$\boldsymbol{\tau}_{cmd} = \underbrace{\boldsymbol{\omega} \times (\mathbf{J}\boldsymbol{\omega})}_{\boldsymbol{\tau}_{gyro}} - \underbrace{\mathbf{J}\Lambda_{act}(t)\dot{\mathbf{q}}_{v,e}}_{\boldsymbol{\tau}_{guide}} - \underbrace{\mathbf{J}\mathbf{K}(t)\text{sat}\left(\frac{\mathbf{s}}{\Phi}\right)}_{\boldsymbol{\tau}_{rob}} \tag{4.13}$$

However, the control law implemented in the *MATLAB* code presented in the Appendix is written as:

$$\boxed{\boldsymbol{\tau}_{cmd} = \underbrace{\boldsymbol{\omega} \times (\mathbf{J}\boldsymbol{\omega})}_{\boldsymbol{\tau}_{gyro}} + \underbrace{\mathbf{J}(\dot{\boldsymbol{\omega}}_d - \Lambda_{act}(t)\dot{\mathbf{q}}_{v,e})}_{\boldsymbol{\tau}_{guide}} - \underbrace{\mathbf{J}\mathbf{K}(t)\text{sat}\left(\frac{\mathbf{s}}{\Phi}\right)}_{\boldsymbol{\tau}_{rob}}} \tag{4.14}$$

In this way, the controller is capable of dynamic tracking, following predefined trajectories rather than working solely in pure regulation (LASM from point A to point B).

Note that in the implementation of the control law (Eq. 4.14), the term dependent on the derivative of the adaptive parameter ($\mathbf{J}\dot{\Lambda}_{act}\mathbf{q}_{v,e}$), which would be added with a negative sign to the right-hand side, has been deliberately omitted. Its compensation is delegated to the robust torque term. As will be seen in the subsequent section, the magnitude of this term

can be considered negligible during the most critical phase of the maneuver, namely in the initial instants of simulated time. During this phase, the flexible disturbance torque reaches its maximum value, and the proposed adaptive logic does not allow the parameter Λ to vary substantially. Once the amplitude of the flexible disturbance torque becomes negligible due to appropriate system damping, Λ will be allowed to vary over time; at that point, however, the robust torque margin will still be sufficient to ensure disturbance rejection.

4.2.4 Lyapunov Stability Analysis

Consider the following Lyapunov candidate functional $V(\mathbf{s})$, which is positive definite due to the fact that the inertia tensor $\mathbf{J}$ is positive definite:

$$V = \frac{1}{2}\mathbf{s}^T\mathbf{J}\mathbf{s} > 0 \quad \forall \mathbf{s} \neq \mathbf{0} \tag{4.15}$$

The sufficient condition for the surface $\mathbf{s} = \mathbf{0}$ to be reached in finite time requires that the time derivative of the functional be strictly negative definite, namely:

$$\dot{V} = \mathbf{s}^T\mathbf{J}\dot{\mathbf{s}} < 0 \tag{4.16}$$

To evaluate the actual Closed-Loop dynamics of the system outside the Boundary Layer (where the Reaching Phase must be guaranteed), the saturation function $\text{sat}(\cdot)$ is replaced with the ideal discontinuous function $\text{sgn}(\cdot)$. Substituting the expanded expression of $\dot{\mathbf{s}}$ derived in Eq. 4.8 into the time derivative of V yields:

$$\dot{V} = \mathbf{s}^T\left[\mathbf{J}\dot{\boldsymbol{\omega}} - \mathbf{J}\dot{\boldsymbol{\omega}}_d + \mathbf{J}\Lambda_{act}(t)\dot{\mathbf{q}}_{v,e} + \mathbf{J}\dot{\Lambda}_{act}\mathbf{q}_{v,e}\right] \tag{4.17}$$

Introducing Euler's equation (Eq. 4.7) to explicitly express the inertial term $\mathbf{J}\dot{\boldsymbol{\omega}}$:

$$\dot{V} = \mathbf{s}^T\left[-\boldsymbol{\omega}\times(\mathbf{J}\boldsymbol{\omega}) + \boldsymbol{\tau}_{cmd} + \boldsymbol{\tau}_{dist} - \mathbf{J}\dot{\boldsymbol{\omega}}_d + \mathbf{J}\Lambda_{act}(t)\dot{\mathbf{q}}_{v,e} + \mathbf{J}\dot{\Lambda}_{act}\mathbf{q}_{v,e}\right] \tag{4.18}$$

At this point, the expression of the actually implemented control law is added (Eq. 4.14, with $\dot{\boldsymbol{\omega}}_d = \mathbf{0}$ and the saturated term reverted to the sign function):

$$\boldsymbol{\tau}_{cmd} = \boldsymbol{\omega}\times(\mathbf{J}\boldsymbol{\omega}) - \mathbf{J}\Lambda_{act}(t)\dot{\mathbf{q}}_{v,e} - \mathbf{J}\mathbf{K}(t)\text{sgn}(\mathbf{s}) \tag{4.19}$$

By performing the substitutions, the nominal kinematic and gyroscopic terms exactly cancel out (dynamic cancelation), leading to the following compact formulation:

$$\dot{V} = \mathbf{s}^T\left[-\mathbf{J}\mathbf{K}(t)\text{sgn}(\mathbf{s}) + \boldsymbol{\tau}_{dist} + \mathbf{J}\dot{\Lambda}_{act}\mathbf{q}_{v,e}\right] \tag{4.20}$$

To guaranty the Lyapunov stability condition stated in Eq. 4.16, and considering the

previous assumptions regarding the $\dot{\Lambda}_{act}$ term, it can be shown that for each axis a minimum value must be guaranteed such that:

$$\boxed{(\mathbf{JK}(t))_{min} \geq |\boldsymbol{\tau}_{dist}|_{max} + \eta} \tag{4.21}$$

where η is a parameter with dimensions of Nm necessary to guaranty an appropriate convergence rate of the reference state to the Sliding Surface.

4.2.5 Budget Allocation Algorithm

The innovation proposed by the present control law lies in the instantaneous determination of the parameters $\Lambda_{act}(t)$ and $\mathbf{K}(t)$. This real-time computation makes it possible to optimize both phases of SMC (namely, the Reaching Phase and the Sliding Phase once the Sliding Surface is reached), aiming to reach the desired reference in the shortest possible time, obtaining a low steady-state error while simultaneously guaranteeing the stability of the method.

1. Definition of the available torque budget. From Equation 4.14, it is imposed that the commanded torque $\boldsymbol{\tau}_{cmd}$ must never exceed $T_{max} \cdot RF$, the maximum torque possibly reduced by a reduction factor $RF \leq 1$ for safety purposes. The following equation is written:

$$|\mathbf{J}\Lambda_{act}(t)\dot{\mathbf{q}}_{v,e}| + |\mathbf{JK}(t)| \leq |T_{max}RF| - |\boldsymbol{\omega} \times (\mathbf{J}\boldsymbol{\omega})| - |\mathbf{J}\dot{\boldsymbol{\omega}}_d| \tag{4.22}$$

A minimum guaranteed margin ($JK_{min} = \tau_{dist,max} + \eta$) is reserved for an effective rejection of baseline disturbances, and the torque components necessary to perform dynamic cancellation are subtracted. A free torque budget is defined as follows:

$$B_{free} = |T_{max}RF| - |\boldsymbol{\omega} \times (\mathbf{J}\boldsymbol{\omega})| - |\mathbf{J}\dot{\boldsymbol{\omega}}_d| - |\mathbf{JK}_{min}| \tag{4.23}$$

2. Adaptive Allocation of $\Lambda(t)$ and Rotating Surface. The rate at which the attitude error decays along the sliding surface is governed by the control parameter $\Lambda(t)$. A high value of Λ is necessary to ensure a rapid convergence of the error to zero once the Sliding Mode condition is reached, as derived in Equation 4.6. A high value of Λ also guaranties a lower steady-state error, which can be derived by calculating the dynamics of the Sliding Surface within the Boundary Layer in the presence of disturbance torques. The steady-state error reaches a maximum value that can be approximated by the following formula:

$$q_{err} = \frac{|\tau_{dist}|_{max}\Phi}{\Lambda JK_{min}} \tag{4.24}$$

Assuming that the system state is close to its steady-state value, the steady-state error can be approximated as a pointing angular error with the following formula:

$$\theta_{err} = \frac{2|\tau_{dist}|_{max}\Phi}{\Lambda JK_{min}} \tag{4.25}$$

However, a high value of Λ in the early stages of the maneuver prevents the state from approaching the Sliding Surface, hindering the control action provided by the robust torque from the term JK, which attempts to drive the state of the system toward the Sliding Surface. This assertion is clearly demonstrated by analyzing the system dynamics in the initial instants of the maneuver, assuming, for simplicity, the absence of external disturbances:

$$\mathbf{J}\dot{\boldsymbol{\omega}} = \underbrace{-\mathbf{J}\Lambda(t)\dot{\mathbf{q}}_{v,e}}_{<0} + \underbrace{(-\mathbf{J}\mathbf{K}\text{sgn}(s))}_{>0} \tag{4.26}$$

Assuming an initial value of the Sliding Variable $s < 0$ and a positive quaternion rate of change, Λ effectively damps the system's velocity increases.

Therefore, a dynamic target parameter, $\Lambda_{target}(t)$, is defined, that varies the surface inclination as a function of the equivalent absolute angular error $\theta_{err} \approx 2\|\mathbf{q}_{v,e}\|$ according to the following logic:

$$\Lambda_{target}(t) = \Lambda_{max} - (\Lambda_{max} - \Lambda_{min}) \cdot \min\left(1.0, \frac{\theta_{err}(t)}{\theta_{th}}\right) \tag{4.27}$$

In this case, Λ_{min} guaranties minimum damping to maximize acceleration during large-amplitude maneuvers, and Λ_{max} ensures maximum precision at convergence. The parameter θ_{th} represents the angular threshold within which the satellite begins to stiffen its kinematics for the final settle. Once the target value of Λ is established, the algorithm must guaranty the physical feasibility of the maneuver by preventing actuator saturation. The maximum value of Λ is calculated as a function of the maximum available torque budget in the following way:

$$\Lambda_{max}(t) = \frac{B_{free}}{|\mathbf{J}\dot{\mathbf{q}}_{v,e}|} \tag{4.28}$$

If Λ_{target} exceeds Λ_{max}, the maneuver is performed with the maximum allowable Λ, that is Λ_{max}. If, instead, the torque budget is sufficient, the system faithfully tracks the optimal target:

$$\Lambda_{act}(t) = \min\left(\frac{\Lambda_{max}(t)}{\Lambda_{target}(t)}, 1.0\right) \cdot \Lambda_{target}(t) \tag{4.29}$$

3. Assignment of $\mathbf{K}(t)$. Recalculating the budget spent on the guidance term with the new Λ_{act}, all the residual torque JK_{avail} is allocated to the robust term with the ultimate goal of maximizing the state's acceleration towards the Sliding Surface, fully exploiting the torque available from the actuators. However, the assignment of the JK term changes as soon as the state enters the Boundary Layer. Upon reaching the Boundary Layer, the gain scales proportionally to the magnitude of the error relative to the Boundary Layer in the following manner:

$$JK_{req} = JK_{min} + (JK_{avail} - JK_{min}) \cdot \min\left(\frac{|\mathbf{s}|}{\Phi}, 1.0\right) \tag{4.30}$$

The final value is strictly constrained between the vital minimum JK_{min} and the maximum available ceiling JK_{avail}. Thus, $JK_{min} \leq JK_{req} \leq JK_{avail}$ is obtained. This gain reduction

within the Boundary Layer was designed to limit possible destructive amplifications of vibrations induced by flexible modes and to ensure lower steady-state torque consumption to reject potential sudden disturbance torques; however, it theoretically entails a small increase in steady-state error, as indicated by the approximate Equation 4.25.

Finally, Figure 4.2 provides a qualitative graphical visualization that illustrates the adaptive allocation of the available torque budget over time, as described in the previous paragraphs.

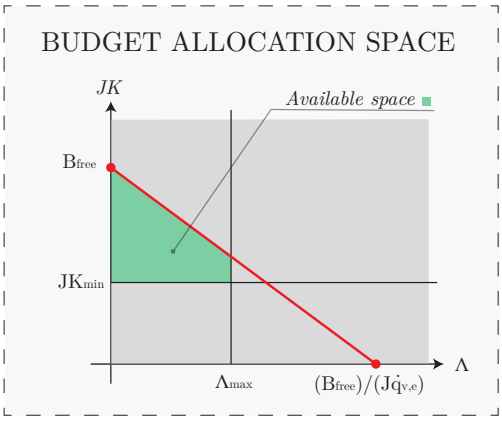

Figure 4.2: Admissible allocation space (green area) for the control parameters at a generic time instant t. The ordinate axis represents the allocated robust torque (**JK**), while the abscissa axis represents the kinematic parameter Λ. The space of valid solutions is lower-bounded by the disturbance robustness requirement ($\tau_{dist} + \eta$) and upper-bounded by the available residual budget line, beyond which the system would enter saturation.

The following chapter aims to validate the proposed control law for the nominal case study presented in Chapter 3. The requirements that the system must satisfy under maximum external disturbance conditions will be defined and after tuning the parameters of ASMC, the simulation results will be analyzed.

Chapter 5

Numerical Simulations and Results Analysis

Contents

5.1 Validation of the Control Law on the Nominal Case Study 63
5.1.1 Simulation Setup 63
5.1.2 Closed-Loop Model 66
5.1.3 Simulation Results Analysis 69
5.2 Robustness Validation against Parametric Uncertainties 82
5.2.1 Sensitivity Analysis on Individual Uncertain Parameters 83
5.2.2 Monte Carlo Analysis on All Uncertain Parameters 97
5.3 Robustness validation against changes in the operational scenario . . 102

This chapter is dedicated to the validation and performance analysis of the ASMC developed in the previous chapter.

To test the control law, the same model proposed in Chapter 3 is used; therefore, the mass and inertia parameters, and the natural frequencies of the solar panels remain as defined in Table 3.1. The following sections precisely define the intended LASM maneuver, the mission requirements that the satellite must satisfy, and the Closed-Loop architecture of the simulator.

5.1 Validation of the Control Law on the Nominal Case Study

5.1.1 Simulation Setup

Definition of the LASM maneuver. To dynamically excite the system and trigger mutual cross-axis couplings, a multi-axis rest-to-rest LASM maneuver is defined. The satellite, initially at rest, has an initial attitude described by the identity quaternion $\mathbf{q}_0 = [1, 0, 0, 0]^T$ and a null angular velocity $\boldsymbol{\omega}_0 = [0, 0, 0]^T$ rad/s, corresponding to perfect alignment with the inertial frame $\mathcal{F}_\mathcal{I}$. The maneuver target is a desired constant attitude profile described by the quaternion $\mathbf{q}_d = [0.8446, 0.1913, 0.4619, 0.1913]^T$, calculated to impose a simultaneous and severe rotation of 45° on the Roll, Pitch, and Yaw Euler angles ($\boldsymbol{\Theta}_{target} = [45°, 45°, 45°]^T$). The desired steady-state angular velocity is strictly zero ($\boldsymbol{\omega}_d = \mathbf{0}$).

Pointing and Safety Requirements. To validate the controller during LASM and in the subsequent attitude maintenance phase, the satellite is considered integrated into a simulated environment where the disturbance torques are at their maximum, and the following operational limits are imposed:

R1 Absolute Pointing Error (APE): The steady-state error must be strictly less than 0.05° to ensure correct payload pointing.

R2 Jitter (Rate Error): The residual angular velocity of the Hub, upon convergence, must remain below 10^{-3} deg/s. This ensures the necessary stability for potential optical operations and prevents persistent excitation and structural fatigue of the flexible modes.

R3 Actuator Hardware Limits: The commanded torque $\boldsymbol{\tau}_{cmd}$ must under no circumstances exceed the physical saturation capacity of the actuation system, set at a theoretical maximum limit of $T_{max} = 2.0$ Nm per axis (with a software safety limit imposed at 1.9 Nm).

In addition to these nominal requirements, the controller must demonstrate intrinsic robustness qualities, maintaining the same performance even if the real model deviates from the estimated one and is subject to parametric uncertainties.

Disturbance Modeling and Estimation of the Maximum Value (D_{max}). For the validation of robustness of ASMC, it is fundamental to formulate a mathematical model of the perturbations acting on the satellite that is both simple and realistic. Exogenous disturbance torques (of an environmental nature or related to internal fluid dynamics) and disturbance torques linked to endogenous uncertainties (related to the torque delivery by the hardware) are identified.

Within the simulator, these phenomena have been isolated into five main categories: uncertainties related to actuator performance, stationary environmental perturbations, propellant sloshing dynamics, flexible coupling, and unmodeled residual noise. For each of these components, an uncertainty distribution has been defined to allow for stochastic variations in future Monte Carlo campaigns. However, for the nominal validation simulation presented in this chapter, the disturbances have been deterministically forced to their absolute maximum values in order to subject the algorithm to the worst-case scenario. The modeling of each contribution is detailed below.

1. Actuator Uncertainty. In physical reality, the actuators (RW) do not instantaneously and exactly deliver the torque commanded by the software onboard. Internal friction, electronic tolerances, and magnetic delays generate a discrepancy between the ideal command and the mechanical action. This phenomenon is modeled as a purely multiplicative uncertainty applied to the control torque. A nominal actuation gain equal to 1.0 is assumed, affected by an independent $\pm 5\%$ uncertainty for each of the three axes (expressed through

the uncertain diagonal matrix $\mathbf{G}_{act}$). The maximum magnitude of the torque lost due to this inefficiency occurs when the controller requests the maximum effort from the actuators ($T_{max} = 2.0$ Nm). The maximum value associated with this type of disturbance is therefore the following:

$$D_{actuator,max} = T_{max} \cdot (1 - RF_{design}) = 2.0 \cdot 0.05 = 0.10 \text{ Nm} \tag{5.1}$$

In this case, the reduction factor designed to guaranty the maximum torque of the hardware to be delivered even in the presence of a torque delivered by the actuators greater than the nominal one assumes a value of $RF_{design} = 0.95$. To simulate the most severe operational condition within the numerical integration loop, the uncertainty matrix is set to the lower limit $\mathbf{G}_{act} = \text{diag}([0.95, 0.95, 0.95])$ throughout the duration of the simulation. In this way, at each time step, the physical Plant receives exactly 5% less torque than commanded by the algorithm ($\boldsymbol{\tau}_{eff} = \mathbf{G}_{act}\boldsymbol{\tau}_{cmd}$), forcing the robust term of the Sliding Mode to actively compensate for this constant lack of torque.

2. Environmental Disturbances. In Low Earth Orbit (LEO), the satellite is subject to the combined action of various environmental forces. In the simulator, the worst-case envelope of these perturbations is modeled in a highly conservative manner as an additive external forcing term with an estimated maximum amplitude of:

$$D_{env,max} = 0.005 \text{ Nm} \tag{5.2}$$

To guaranty rejection of this disturbance in the worst-case scenario, the vector $\boldsymbol{\tau}_{dist,env}$ is forced to its upper limit on all three axes simultaneously.

3. Propellant Sloshing Dynamics. The movement of fluids inside the tanks during impulsive maneuvers generates complex reaction torques, known as Propellant Sloshing. In the literature, this phenomenon is typically addressed by integrating equivalent mechanical models into the multi-body dynamics, such as mass-spring oscillators or models that associate sloshing dynamics with pendulum dynamics. However, the exact implementation of such models falls outside the scope of the present work, whose primary objective is the validation of the controller's robustness against disturbance torques of various natures.

Sloshing is modeled as an additive harmonic disturbance whose amplitude is proportional to the control effort. Assuming that the oscillation of the fluid mass can subtract or add up to a maximum of 2% of the torque delivered by the actuators operating at their physical limit (T_{max}), the following estimate of the maximum value is obtained:

$$D_{slosh,max} = T_{max} \cdot 0.02 = 0.04 \text{ Nm} \tag{5.3}$$

Within the numerical simulation loop, this perturbation is forced to oscillate with a constant frequency of 0.52 Hz. This value is not arbitrary, but derives from a specific engineering choice aimed at stressing the system, maximizing the risk of triggering CSI interaction cycles

with the flexible components of the structure.

4. Flexible Coupling CSI. The control algorithm calculates the dynamic cancellation terms and the commanded torque $\boldsymbol{\tau}_{cmd}$ by referring exclusively to the nominal rigid model, as extensively discussed in Chapter 4. The calculated commanded torque is delivered to the flexible Plant, which assumes a state different from the one predicted by the controller. From the controller's perspective, it is as if a disturbance torque component τ_{dist} were added to the commanded torque, accounting for the unexpected variation in the state received as feedback from the physical Plant (which, indeed, features flexible appendages). In addition to the components of the disturbance torque that have been discussed previously, it is necessary to define the maximum magnitude of the disturbance torques that are directly derived from the actual CSI. A maximum value for the flexible disturbance torque is estimated as a function of the maximum commanded torque in the following way:

$$D_{flex,max} = 0.35 \cdot T_{max} = 0.35 \cdot 2.0 = 0.70 \text{ Nm} \tag{5.4}$$

5. Residual Disturbances (Unmodeled Dynamics). To ensure statistical coverage of any micro-dynamics not explicitly modeled (such as local flexibility of antennas, small thermal deformations, or circuit noise), an additional, purely conservative additive term is introduced. This margin is estimated as follows:

$$D_{res,max} = 0.005 \text{ Nm} \tag{5.5}$$

This value can be subsequently increased if the controller fails to ensure a satisfactory degree of robustness during the analyzes that include parametric uncertainties.

5.1.2 Closed-Loop Model

The complete architecture of the model used in the simulator for the validation of the control law in a worst-case scenario, dominated by the maximum external disturbance torque component, relies on some fundamental assumptions. These are necessary to simplify the inherently complex problem, to begin obtaining important estimates related to compliance with the requirements and the dynamic response of the system, and to visualize the operation of the proposed adaptive logic.

1. **Ideal Actuators**. An instantaneous delivery of the torque commanded by RW is assumed. However, a physical amplitude saturation limit is applied at $T_{max} = 2.0$ Nm per axis, with the operating software limit set to 1.9 Nm. It is also assumed that the torque actually applied to the system differs from the purely commanded one to simulate an actuator performance different from the nominal one and to test the robustness of the algorithm.

2. **Ideal Sensors and Zero System Latency**. It is assumed that the states are instantaneously measurable or estimable and are not affected by any type of noise or error. Further delays in the system, related to data transmission times and processing and execution times of the onboard computer, are neglected.

The summary block diagram of the simulator is presented in Figure 5.1. The software architecture developed for the simulator validation is governed by the main script `N08_CL_FlexPlant_Disturbi_BASE.m`, which utilizes various auxiliary functions developed in the *MATLAB* environment, detailed in Appendix A.5.

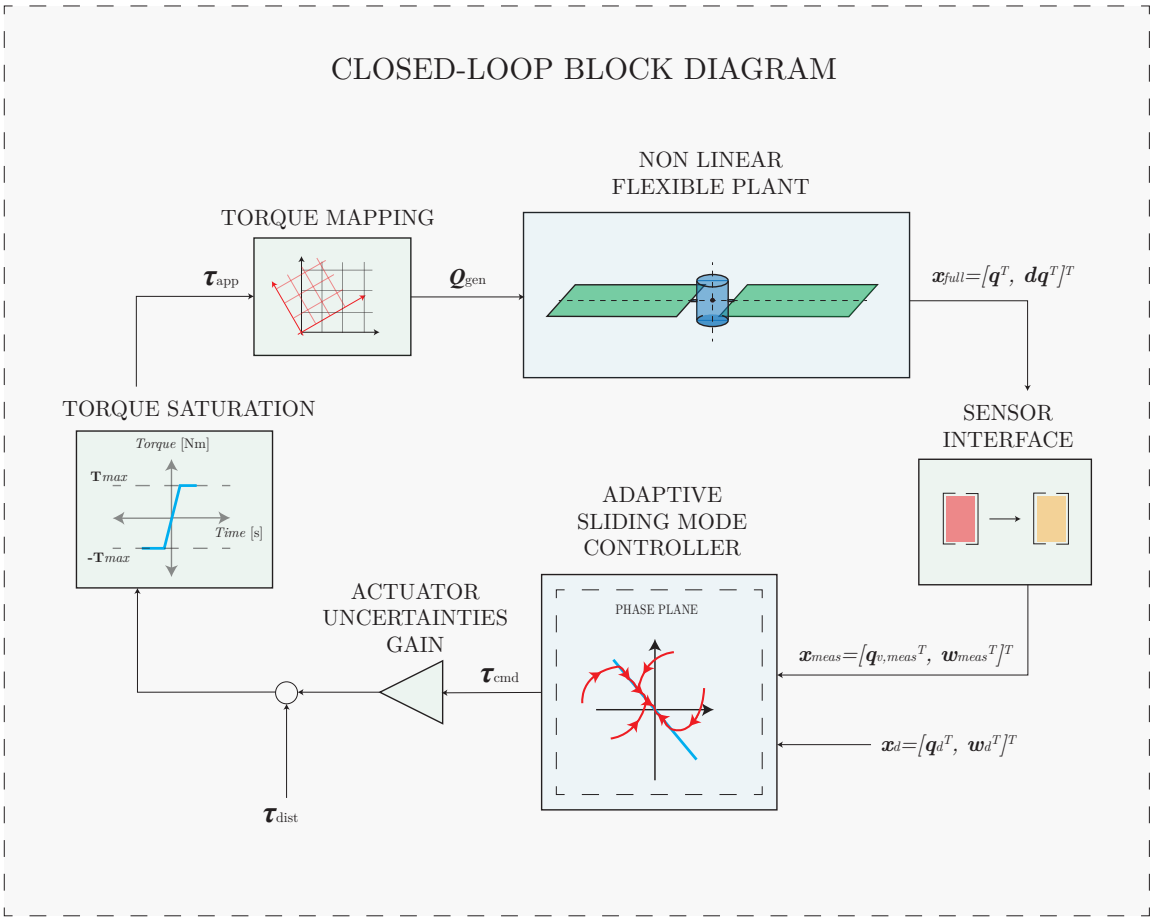

Figure 5.1: Logical architecture of the Closed-Loop simulator. The diagram illustrates the signal flow between the ASMC control algorithm, the disturbance modeling, the mapping of the forcing terms and the state vector, and the integration of the non-linear multi-body dynamics.

The main blocks and their relative signal nomenclature are defined below:

- **Adaptive SMC Controller**: It constitutes the algorithmic core of the Guidance, Navigation, and Control (GNC) system. It receives as input the desired state $\mathbf{x}_d =$

$[\mathbf{q}_{v,d}^T, \boldsymbol{\omega}_d^T]^T$ and the state measured by the ideal sensors $\mathbf{x}_{meas} = [\mathbf{q}_{v,meas}^T, \boldsymbol{\omega}_{meas}^T]^T$, where $\mathbf{q}_{v,meas}^T$ is the vector component of the reference quaternion and $\boldsymbol{\omega}_{meas}^T$ is the angular velocity measured in the body axis. By processing the kinematic error through the adaptive control logic described in the previous chapter, it outputs the ideal command torque vector $\boldsymbol{\tau}_{cmd} \in \mathbb{R}^3$.

- **Disturbance & Saturation Model**: The commanded torque is not ideally transferred to the Plant. First, it undergoes possible multiplicative alterations related to an actuator performance different from the nominal one, and is then vectorially added to the aggregated disturbance torques $\boldsymbol{\tau}_{dist}$. Subsequently, the resulting signal is filtered by the physical saturation block to ensure compliance with the actuator hardware limits, producing the torque actually applied in the body axes $\boldsymbol{\tau}_{app}$ (limited to $\pm T_{max}$).

- **Torque Mapping**: The differential equations of the flexible model are derived using a Lagrangian approach, which requires generalized forces as input. This block receives the applied torque on the body axes $\boldsymbol{\tau}_{app}$ and, using the kinematic transformation matrix and the Principle of Virtual Work, projects it onto the generalized forces vector $\mathbf{Q}_{gen} \in \mathbb{R}^{18}$ compatible with the rotational degrees of freedom of the system.

- **Non-Linear Flexible Plant**: It represents the satellite's dynamics. It receives the generalized forces $\mathbf{Q}_{gen}$ and, through the numerical solver, integrates the coupled Hub-Panel dynamics. The output identifies the complete and updated state of the multibody system $\mathbf{x}_{full} = [\mathbf{q}^T, \dot{\mathbf{q}}^T]^T \in \mathbb{R}^{36}$. The generalized coordinates vector $\mathbf{q} \in \mathbb{R}^{18}$ is defined as $\mathbf{q} = [\mathbf{r}^T, \boldsymbol{\Theta}^T, \boldsymbol{\eta}_{p1}^T, \boldsymbol{\eta}_{p2}^T]^T$, where $\mathbf{r}$ and $\boldsymbol{\Theta} = [\phi, \theta, \psi]^T$ represent, respectively, the translation coordinates and Euler angles of the central Hub in the inertial frame, while $\boldsymbol{\eta}_{p1}, \boldsymbol{\eta}_{p2} \in \mathbb{R}^6$ group the modal degrees of freedom associated with the flexible deformations of the two solar panels.

- **Sensor Interface (State Conversion)**: Since the attitude controller requires exclusively the kinematics of the rigid body (Hub), this block filters the complete state $\mathbf{x}_{full}$ by extracting the angular velocities and Euler angles of the Hub. Finally, it performs the kinematic conversion from Euler angles to quaternions to prevent singularities and implement the adaptive control law, instantaneously returning the measured state without noise and error $\mathbf{x}_{meas}$ to the controller.

Configuration of the Control Law Parameters. According to the guidelines defined in Chapter 4, in Section 4.2 which explains the operation of the adaptive control logic, the values to be assigned to the robust margin JK_{min} to ensure the system's ability to counteract external disturbance torques are derived, along with the other time-varying parameters. From the previous analysis of the disturbance torques applied to the system, the maximum magnitude of the total disturbance is derived:

$$D_{max} = D_{actuator} + D_{env} + D_{slosh} + D_{flex} + D_{res} \approx 0.85 \text{ Nm} \tag{5.6}$$

Based on this value, the parameter JK_{min} is defined as $D_{max} + \eta = 0.8925$ Nm, obtained by imposing a torque margin value η equal to 5% of the estimated maximum disturbance

value. An initial value of Λ equal to $\Lambda(0) = 0.2$ rad/s and a maximum value equal to $\Lambda_{max} = 5$ rad/s are imposed. Finally, a Boundary Layer thickness value of $\Phi = 0.01$ rad/s is estimated to satisfy a trade-off related to multiple requirements. On the one hand, it is essential to have a sufficiently low value of Φ to guaranty a minimum steady-state error, aiming to satisfy requirement **R1**; on the other hand, a Φ value that is too low risks exciting the CSI interaction in the event of unexpected steady-state disturbance torques.

5.1.3 Simulation Results Analysis

The dynamic analysis of the Closed-Loop system is presented. The simulation analysis begins with the observation of the macroscopic quantities of the system, namely the attitude variables.

Kinematic Validation and Pointing Requirements. The first fundamental aspect for the mission validation consists of verifying the Hub's kinematics, in order to guarantee compliance with the absolute pointing (**R1**) and pointing line stability (**R2**) requirements.

The attitude evolution is described in Figure 5.2, which shows the time evolution of the Euler angles during the maneuver, and the time evolution of the quaternion components in Figure 5.3. As can be seen from the graphs, the controller's action guides the satellite from the initial condition to the target attitude of 45°.

To quantify the steady-state precision and compliance with mission requirements **R1** and **R2**, Figure 5.4 illustrates the attitude error and the residual angular velocity jitter, represented on a logarithmic scale.

The top graph demonstrates that the total pointing error, rigorously calculated from the norm of the vector part of the error quaternion, decays rapidly and, starting from $t \approx 45$ s, is stably confined within the Safe Zone, shown in green in the Figure. The final steady-state value settles at $2.50 \cdot 10^{-3}$ degrees, satisfying the limit imposed by requirement **R1** ($< 0.05°$) by a wide margin, assuming the maximum value of the disturbance torque indicated previously. In parallel, the lower graph confirms compliance with requirement **R2** in steady state.

Sliding Dynamics and Phase Plane Analysis. To explain the operation and peculiarities of the proposed adaptive control law, reference can be made to two fundamental graphs characteristic of classical SMC.

Figure 5.5 illustrates the evolution of the state trajectory in the phase plane for the three principal axes. The abscissa axis represents the vector component of the quaternion error (q_{err}), while the ordinate axis represents the angular velocity error (ω_{err}).

The graph highlights the intrinsically time-varying nature of the designed sliding surface, caused by the variation of the parameter Λ. During the initial phase of the maneuver, the

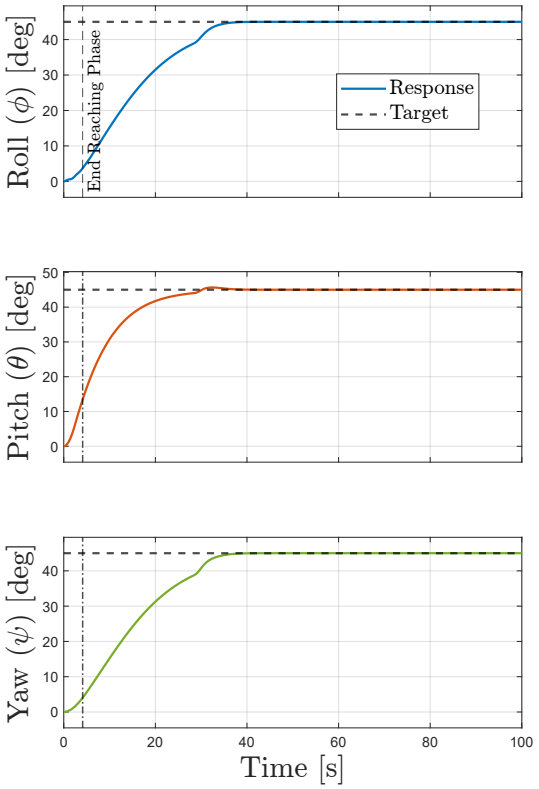

Figure 5.2: Time evolution of the Euler angles.

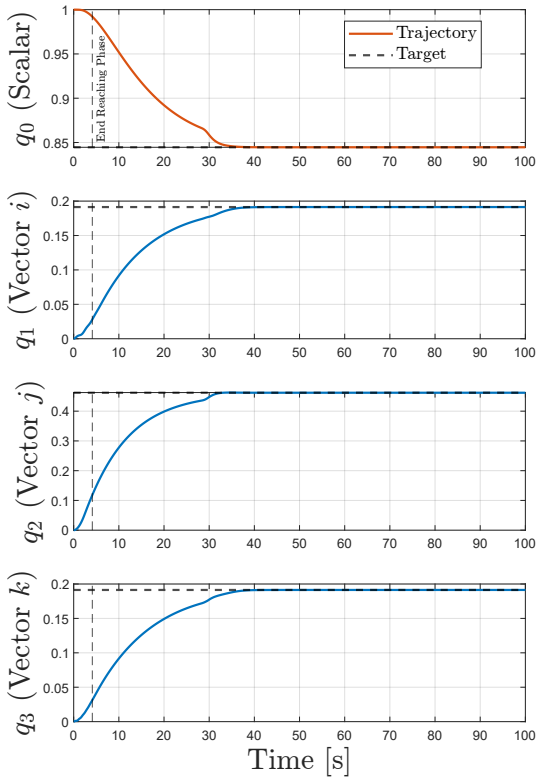

Figure 5.3: Time evolution of the quaternion.

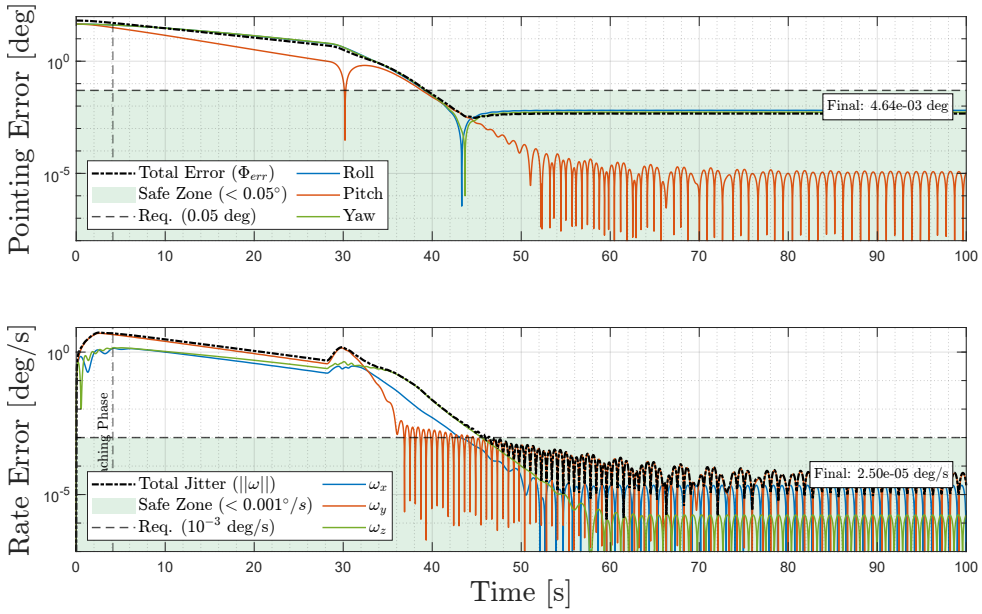

Figure 5.4: Accuracy and pointing stability analysis on a logarithmic scale. The upper graph shows the decay of the total attitude error with respect to the 45° target, while the lower graph illustrates the damping of the angular velocities (jitter). Both quantities settle stably below their respective tolerance thresholds (**R1** $< 0.05°$, **R2** $< 10^{-3}$ deg/s), highlighted by the green bands.

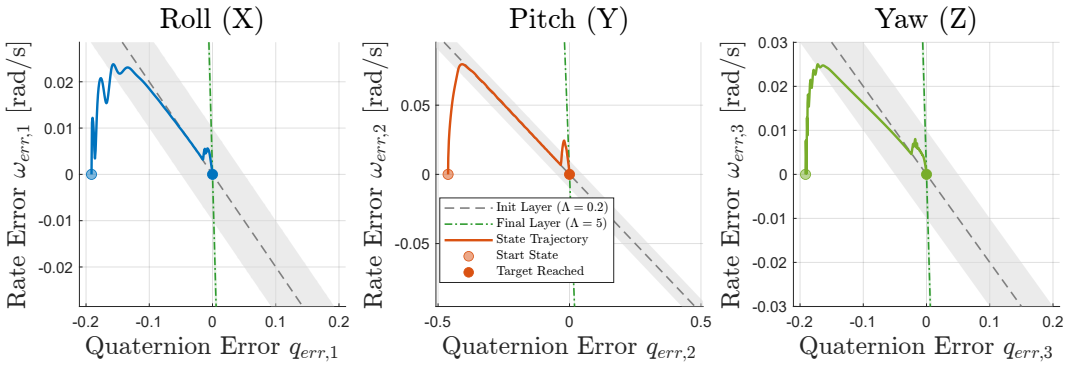

Figure 5.5: State trajectory in the phase plane. The initial and final trajectory of the Sliding Surface, the thickness of the Boundary Layer, the initial gray band ($\Lambda_{nom} = 0.2$), and the final green band ($\Lambda_{max} = 5.0$) are visible. The trajectory (colored line) is smoothly guided towards the origin (target reached).

trajectory is attracted within the gray band towards the Sliding Surface defined by the value $\Lambda_{nom} = 0.2$ rad/s. As soon as the decreasing attitude error crosses the 5° threshold, around 30 s into the maneuver, the kinematic adaptation gradually increases the slope of the surface up to $\Lambda_{max} = 5.0$ rad/s (green band) according to the torque budget allocation logic. At this point, it is as if the system initiates a second Reaching Phase, tracking a rotating and time-varying sliding surface (not shown in the figure) until it converges to the surface defined by Λ_{max}. This strategy allows the satellite's angular velocity to increase, as visible in Figure 5.6, temporarily increasing the error but allowing the state to reach a new, steeper Sliding Surface where the error dynamics evolve more quickly towards the target.

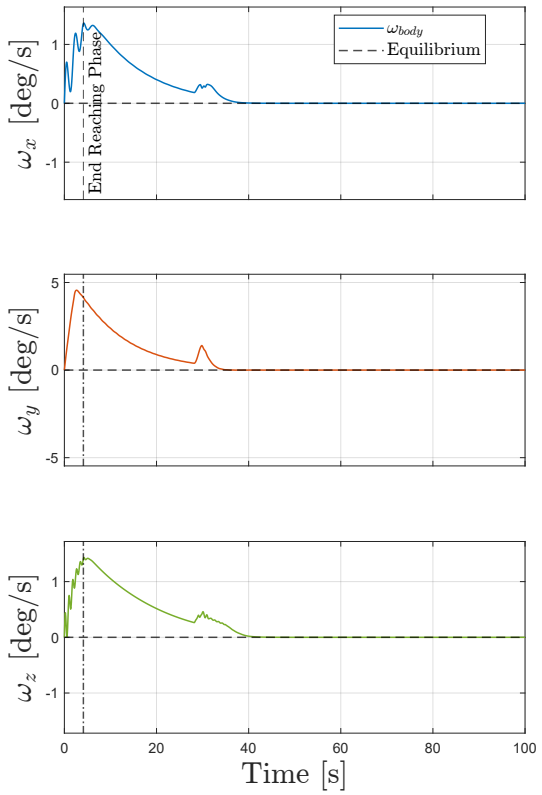

Figure 5.6: Time evolution of the angular velocities ($\boldsymbol{\omega}$).

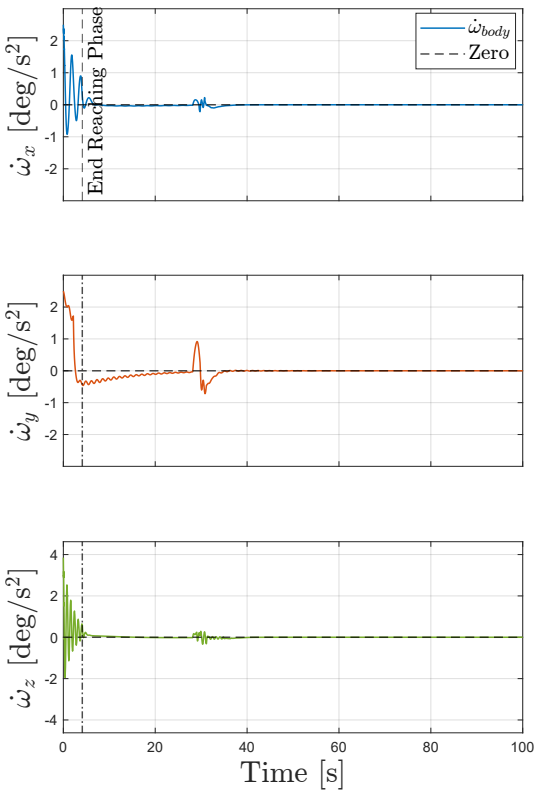

Figure 5.7: Time evolution of the angular accelerations ($\dot{\boldsymbol{\omega}}$).

The increase in angular velocity translates into an increase in the convergence speed of the Euler angles towards the target around 30 s of simulation, visible in Figure 5.2. A substantial difference is also noted by observing the time evolution of the Sliding Variable s in Figure 5.8.

Adaptive Logic and Disturbance Rejection. Figure 5.9 describes the time evolution of the control law gains.

The top graph confirms the correct implementation of the $\Lambda(t)$ transition and allows for a better interpretation of what was discussed in the previous paragraph. A smoother

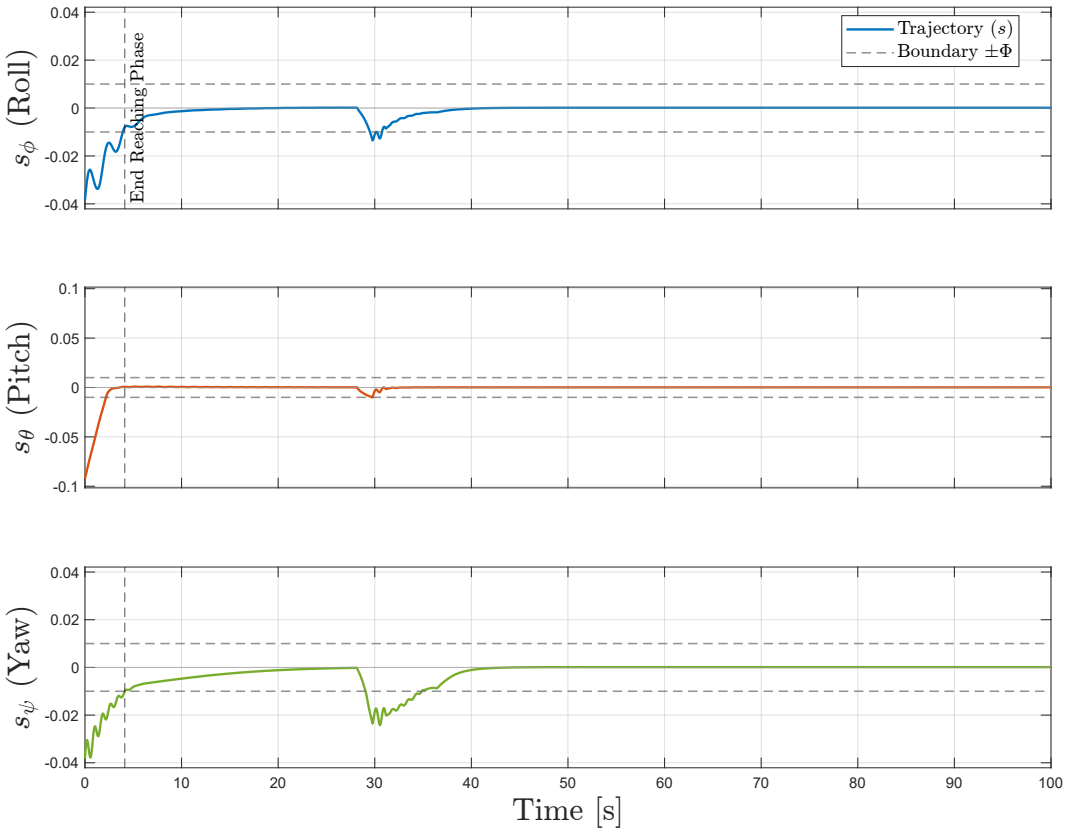

Figure 5.8: Time evolution of the Sliding Variables s. The trajectories cancel out the large initial misalignment, enter within the Boundary Layer $\pm\Phi$, and converge asymptotically. Around 30 s, a phenomenon related to a gradual change in the slope of the Sliding Surface towards the value Λ_{max} is observed. The faster convergence of the Sliding Variable to zero is noted.

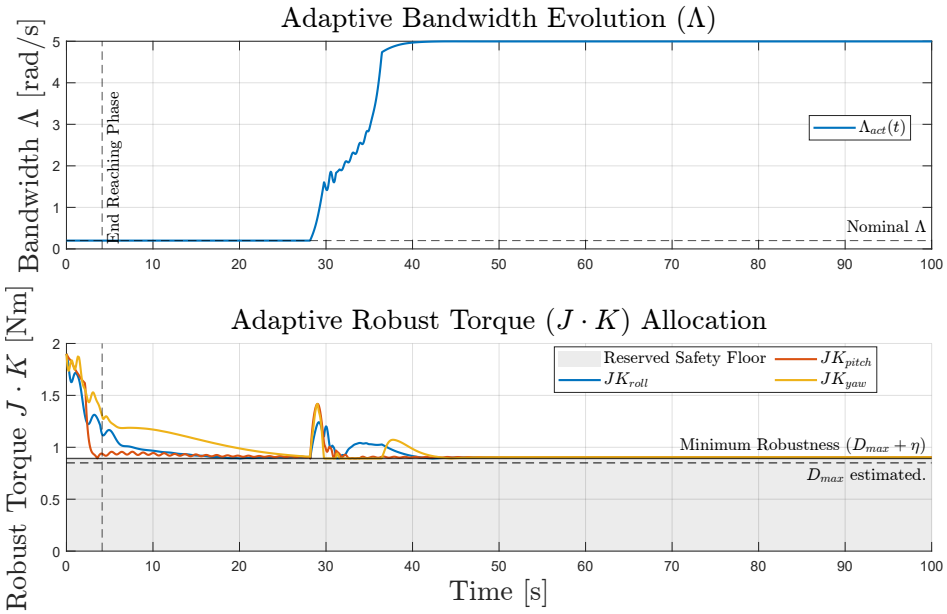

Figure 5.9: Evolution of the adaptive parameters: smooth transition of the parameter Λ_{act} (top) and directional allocation of the robust gain $J \cdot K$ (bottom). The shaded area represents the impassable operational safety limit below which the robustness and stability of the method are not guaranteed.

and more precise transition of Λ as a function of attitude error, starting from the initial time instants to ensure better performance, is deferred to subsequent detailed analyzes. The graph at the bottom describes the allocation of directional robust gain $J \cdot K$. The algorithm increases the control effort in a targeted manner solely during the acceleration transient and in conjunction with the change in the surface slope (at $t \approx 30$ s) to allow the system's velocity to increase and to effectively manage the resulting flexible disturbance torques. In steady state, the adaptation relaxes the gains to avoid triggering any dangerous oscillatory dynamics in response to unexpected disturbance torques, while respecting the robustness constraint. None of the curves ever falls below the allocated torque budget ($D_{max} + \eta$).

Figure 5.10 highlights the actual disturbances applied to the Plant during the maneuver.

The analysis reveals how, from the perspective of the controller, the dominant disturbance is represented by the actuator uncertainty ($\Delta T_{dist,gain}$), which, being proportional to the delivered command, presents maximum peaks during the acceleration phase and then vanishes at steady state. Less severe, but highly oscillatory, are the propellant Sloshing effects. At steady state, the commanded torque $\boldsymbol{\tau}_{cmd}$ is equal to the residual disturbance torque, while the torque actually delivered to the Plant is zero.

Control Effort Analysis. The control effort analysis serves to demonstrate the practical feasibility of the maneuver and the absence of saturation phenomena or premature hardware wear, as dictated by mission requirement **R3**.

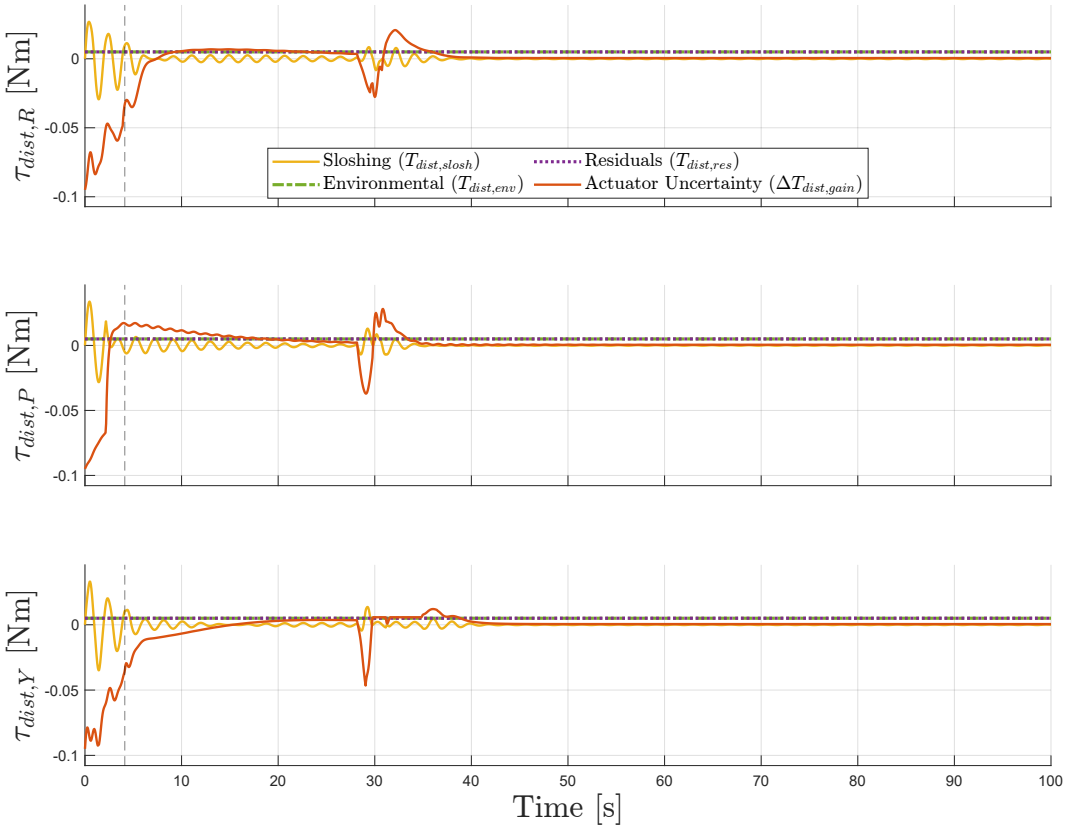

Figure 5.10: Analysis of the disturbance torques acting on the Hub: propellant Sloshing effects proportional to the applied torque, environmental disturbances, and proportional actuator gain uncertainties.

Figure 5.11 describes the time profile of the torque actually delivered along the three axes of the Body frame, compared with the physical saturation limit of the Reaction Wheels (T_{max} = 2.0 Nm), with the torque commanded by the controller, and with the operational safety margin set at 1.9 Nm (Buffer Zone) following an RF reduction factor value of 0.95.

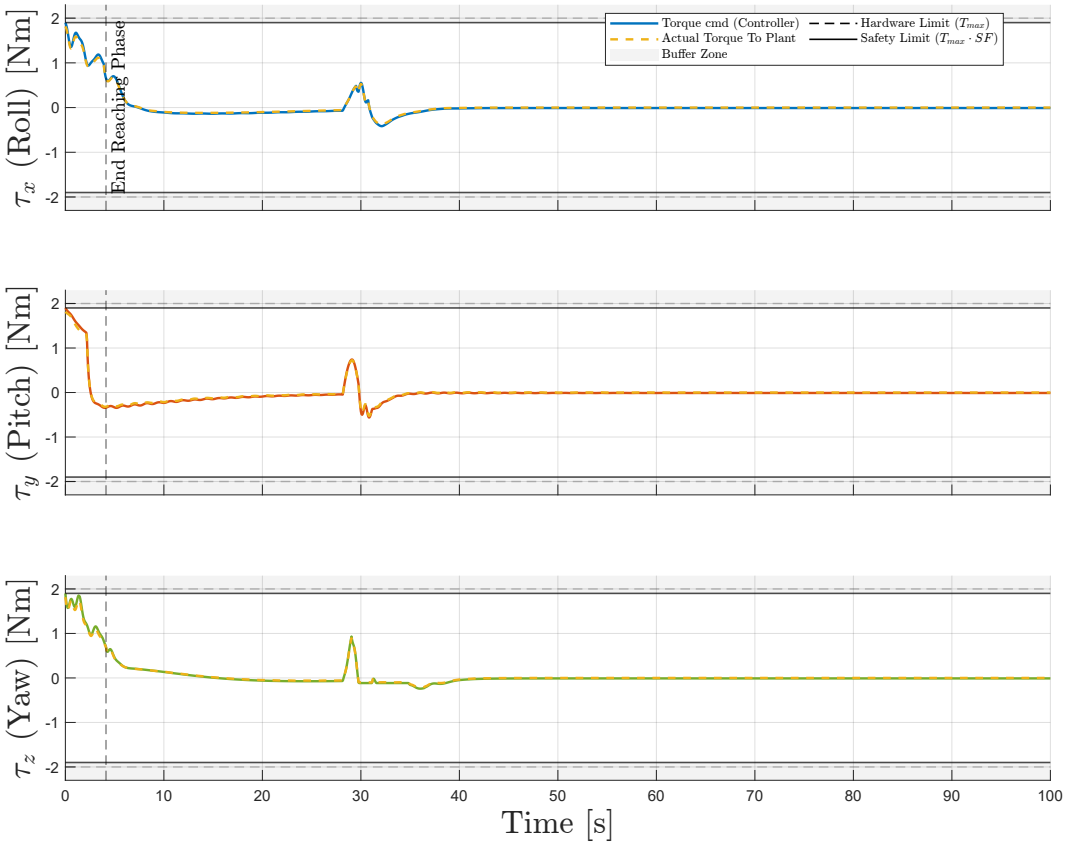

Figure 5.11: Time profile of the global control effort. The maneuver requires a high initial torque to overcome the system's inertia, which subsequently settles to a lower value without ever violating the physical or operational limits of the actuators. It is noted that the torque actually delivered to the Plant differs slightly from the commanded torque. The small difference is attributable to the disturbance torques, which are of a lower order of magnitude compared to the represented scale.

As is predictable for LASM, the starting phase requires a significant initial effort, bringing the torque close to the safety threshold along the Roll (X) and Yaw (Z) axes. The most qualifying aspect of this result is the extreme cleanliness of the signal. Despite the excitation of the flexible dynamics, the controller does not react by commanding a torque with high-frequency components but focuses exclusively on nullifying the attitude and velocity errors. The application of a torque with high-frequency components would have been a potential cause for triggering resonances with the flexible appendages due to CSI. Around 30 seconds, a secondary, lower-intensity torque peak is visible. This peak is the direct consequence of the adaptive increase of the Λ parameter analyzed in the previous section, which requires a temporary increase in the satellite's velocity to reach a steeper Sliding Surface.

To understand in detail how the algorithm build this commanded torque signal, Figure 5.12 presents the algebraic breakdown of the commanded torque into its three fundamental components: equivalent, gyroscopic, and robust.

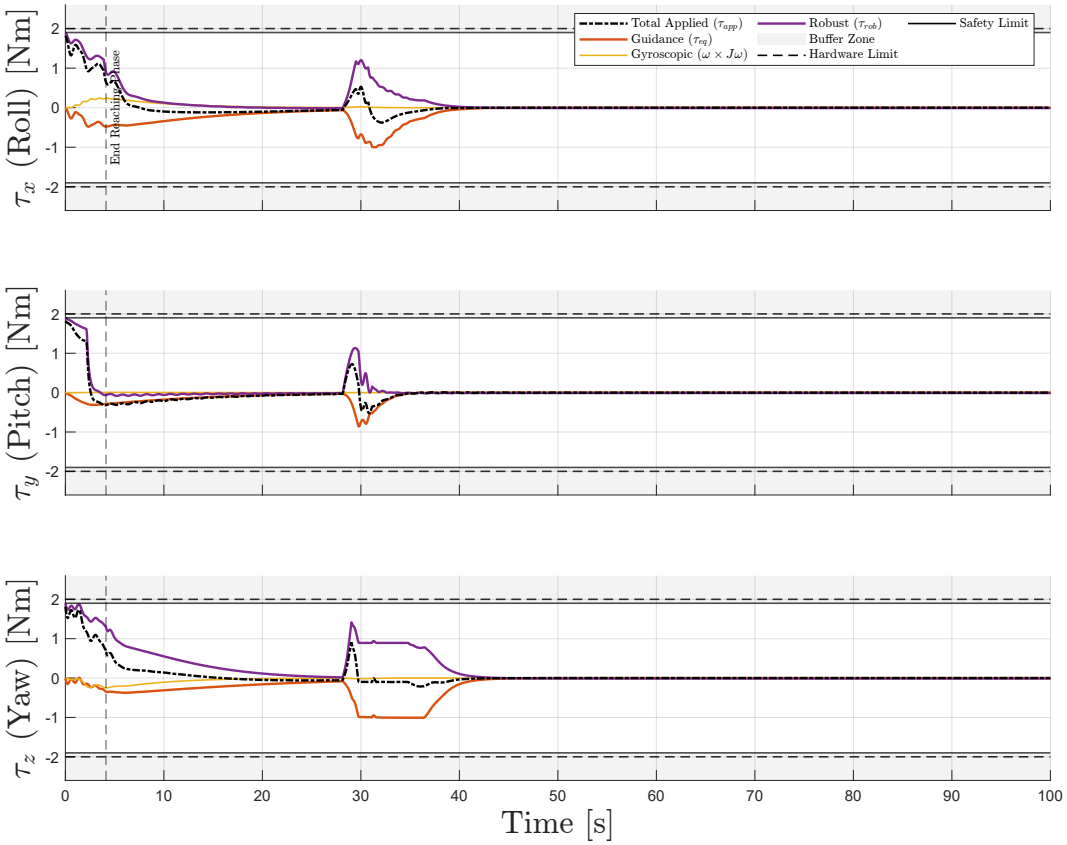

Figure 5.12: Analytical breakdown of the control law. It highlights the load distribution among the component related to dynamic cancellation, the gyroscopic compensation, and the robust action during transients.

The robust component allows counteracting any external disturbance torques and energetically pushing the system towards the Sliding Surface in the initial instants of the maneuver. Its behavior is analogous to that of the previously analyzed sliding variable (although with the opposite sign), as illustrated in Figure 5.8.

The equivalent component (τ_{eq}) intervenes in the early stages of the maneuver by damping any excessive increases in the satellite's velocity induced by the action of the robust torque, and has the task of driving the error asymptotically to zero once the Sliding Surface ($s = 0$) is reached.

The gyroscopic component ($\boldsymbol{\omega} \times \mathbf{J}\boldsymbol{\omega}$) is proportionally modest but essential for nullifying the strong non-linear couplings induced by the simultaneous maneuver, and it is the component responsible for dynamic cancellation. It is observed that the most pronounced gyroscopic couplings manifest along the Roll (X) and Yaw (Z) axes. On these axes, it is necessary to allocate a higher torque budget in order to counteract the disturbance torques induced by the

multi-axis LASM, due to a lower inertia around the Pitch rotation axis (Y).

Dynamic Interaction (CSI). Although the control signal is extremely clean, the real satellite is a multi-body system subject to complex internal dynamics.

Observing the components of angular velocity and angular acceleration on the three axes in Figure 5.7, the effects of CSI, not directly visible in the graph in Figure 5.2, can be noted. The violent vibrations highlight the direct exchange of reactive torques between the appendages and the Hub. To guide the satellite towards the target, it is necessary to avoid exciting the natural vibration modes of the coupled system, and therefore the injection of energy into the system, and to let the structural damping do its job of energy dissipation. Although these oscillatory dynamics are inevitably excited during the maneuver to ensure a rapid response, the controller does not amplify such oscillations, ensuring a stable convergence towards the target and demonstrating excellent management of the flexible disturbance torque τ_{flex}.

To justify the strong oscillations observed in the angular acceleration of the central body, it is necessary to analyze the local dynamics of the flexible appendages.

In the Lumped Parameter Approach (LPA), the deformation of each panel is described by a set of six degrees of freedom $\boldsymbol{\eta} \in \mathbb{R}^6$, defined with respect to the local reference frame $\mathcal{F}_m$ fixed to the root of the panel. Observing the evolution of the modal coordinates in Figure 5.13, it is noted that, as expected, the translational deformations are negligible, remaining in the order of 10^{-4} mm. The rotational deformations are dominated by the Flapping mode around the panel's local X axis, although the deformations related to Torsion on the local Y axis and to the In-Plane Bending mode on the local Z axis are not negligible, each with the frequency associated with the respective vibration mode of the coupled system. It is noted how the rotational deformations are limited and well damped over time.

To physically quantify the magnitude of these deformations, the modal coordinates η_i are mapped into the physical displacement corresponding to the ends of the panels (Tip Displacement), as previously done in the Open-Loop model validation in Chapter 3.

Figure 5.14 translates the modal coordinates into the actual physical displacement (in millimeters) measured at the tips of the solar panels.

The analysis of Figure 5.14 provides a clear interpretation of the multi-axis maneuver with respect to flexible deformations. While the Hub accelerates and begins to rotate under the action of the commanded torque, the panels lag behind due to inertia. Panel 1 exhibits a tip displacement along the Z axis in the downward direction within the reference frame $\mathcal{F}_m$, while Panel 2 shows an opposite deformation. The flexible deformation identifies the position of the reference frame anchored to the root of the panel $\mathcal{F}_p$ relative to the reference frame that rotates rigidly with the Hub, which is also anchored to the root of the panel in the undeformed configuration. This confirms that the antisymmetric Flap mode is excited during the maneuver, as expected for a multi-axis LASM. The same situation occurs on the other maneuver axes.

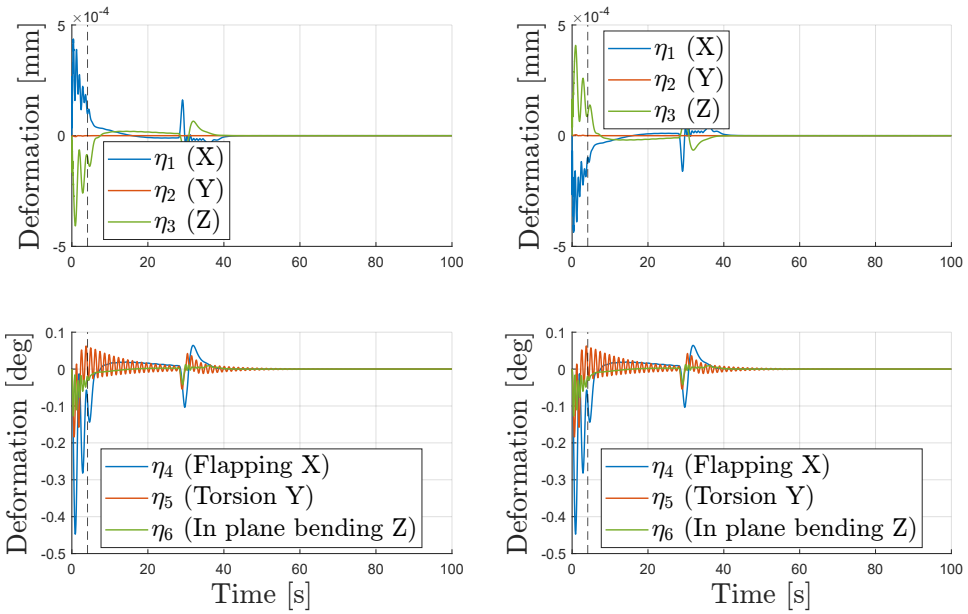

Figure 5.13: Evolution of the flexible modal coordinates (η). The translational deformations (top) are numerically negligible, while the rotational deformations (bottom) exhibit limited and well-damped transient oscillations. The graphs on the left represent the degrees of freedom of Panel 1. The graphs on the right represent the degrees of freedom of Panel 2.

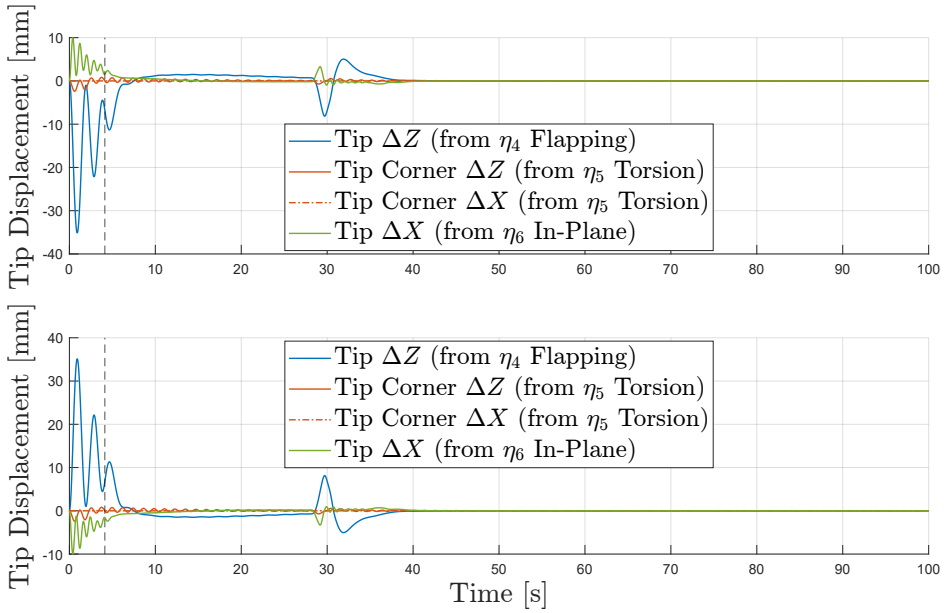

Figure 5.14: Linear displacement at the tips of the solar panels (Tip Displacement). The top graph refers to Panel 1, while the bottom graph refers to Panel 2.

Figure 5.15 illustrates the crucial difference between the commanded torque net of disturbance torques and the net torque that actually moves the Hub.

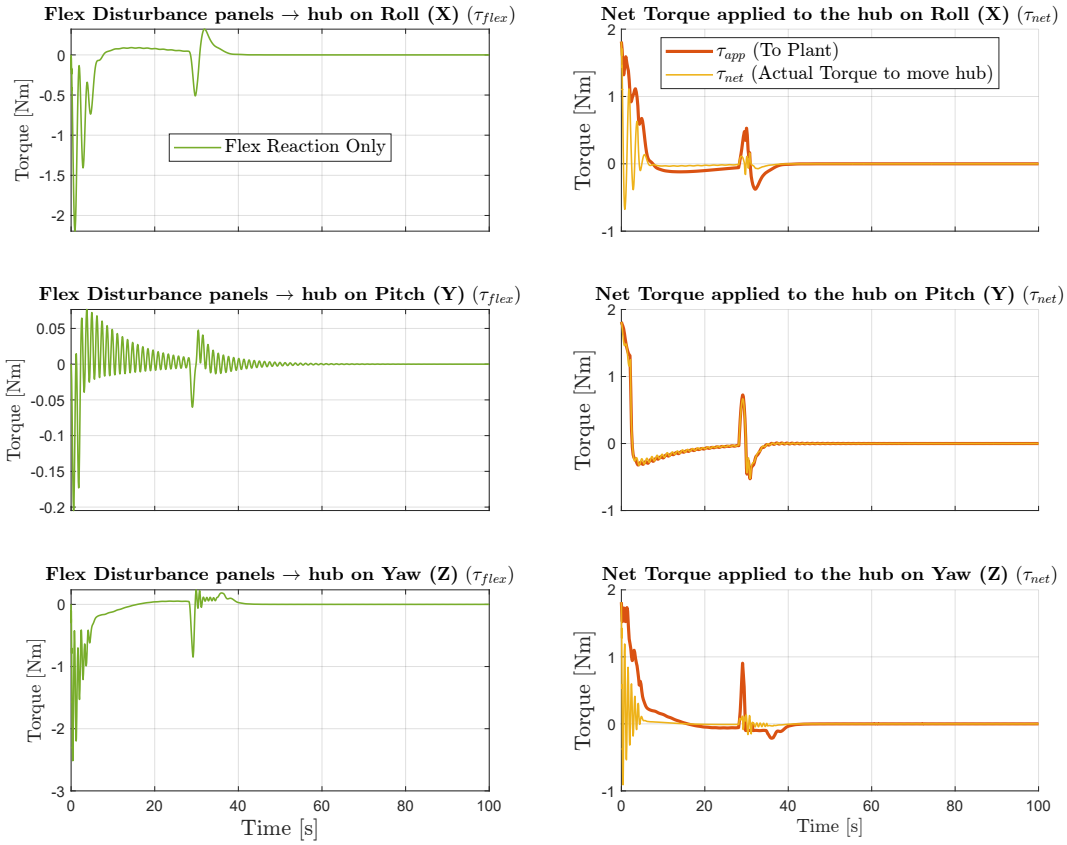

Figure 5.15: Control-Structure Interaction (CSI). On the left, the impulsive disturbance torques generated by the solar panels' flexion (τ_{flex}) are represented. On the right, a comparison is shown between the torque input to the flexible Plant (τ_{app}) and the actual net torque experienced by the Hub (τ_{net}).

The graphs on the left reveal the magnitude of the flexible disturbance ($\boldsymbol{\tau}_{flex}$) transferred from the solar panels to the Hub during the first two seconds of the simulation. These impulses reach peaks larger than 2.0 Nm in counter-phase, representing a disturbance that could destabilize any classical linear controller. The graphs on the right demonstrate the attitude robustness: although the net torque ($\boldsymbol{\tau}_{net}$) experiences the elastic drag of the oscillating panels, the control action remains predominant and sufficient to guide the Hub toward the target without amplifying these oscillations. The ability of the control law to absorb elastic disturbances guaranties the absolute stability of the rigid body.

Energy Stability Verification. To conclude the nominal case analysis, the time evolution of the system energy is reported. Figure 5.16 traces the time profile associated with the energy balance of the multi-body system.

At the macroscopic level (Subplot 1), the total mechanical energy ($E_{tot} = T + V$) exhibits

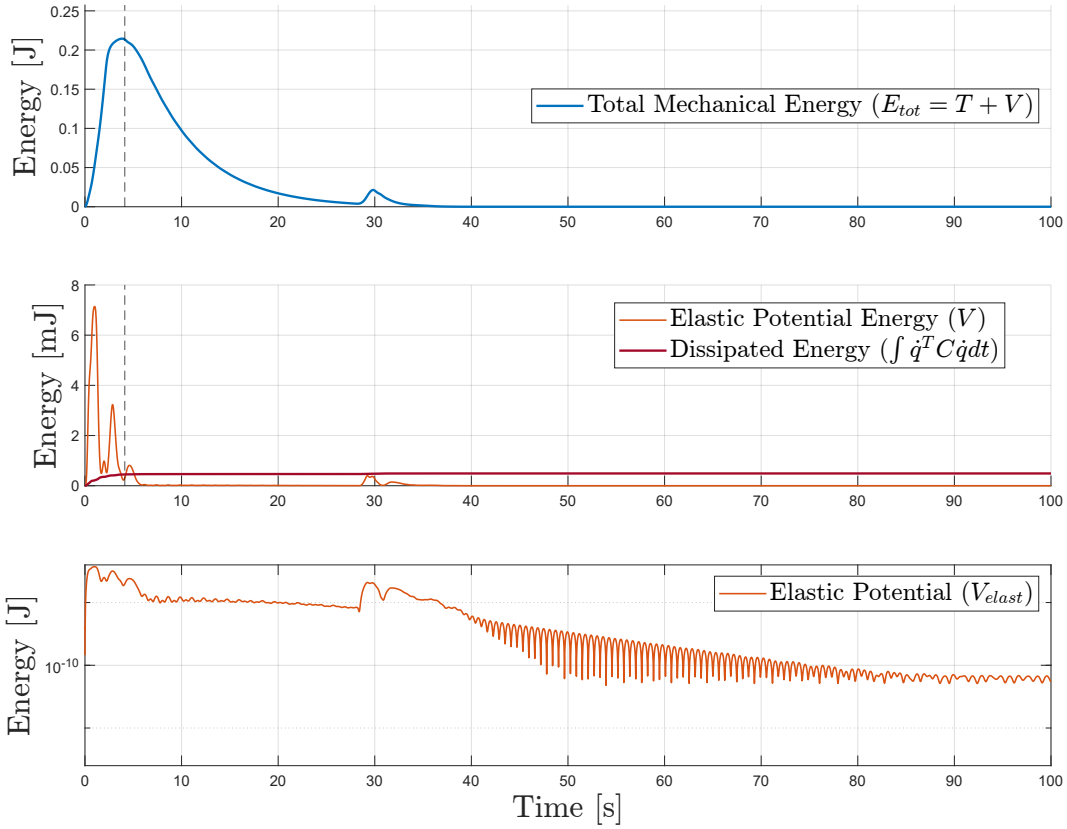

Figure 5.16: System energy balance. The total mechanical energy decays asymptotically (top). The elastic energy (middle and bottom on a logarithmic scale) is entirely dissipated.

the perfect asymptotic dissipative behavior required by non-linear control theory. After the physiological initial injection of kinetic energy by the reaction wheels to start the maneuver, the system progressively loses energy until it settles into a state of rest. The only secondary peak, of smaller magnitude than the first, is observed near the variation of the parameter Λ. The controller injects energy around 30 seconds of simulation to vary the slope of the Sliding Surface and accelerate the system toward the intended target.

At the microscopic level (Subplot 2), the internal dynamics of the elastic deformation can be isolated. The elastic potential energy of the panels accumulates during the first phase of the impulsive maneuver as the satellite accelerates, gaining velocity; its time evolution is obtained from the sum of the time profiles of the components related to flexible deformations. The trend of the potential energy mainly follows the time evolution of the rotational deformations related to the Flapping mode. This lower-frequency mode is the primary one excited during the maneuver and exhibits the highest intensity peaks. As imposed by the Rayleigh parameter $\zeta = 0.005$, the damping matrix $\mathbf{C}$ progressively converts this elastic energy into dissipated heat (burgundy curve). Once the control torques become negligible, the cumulative dissipative work ($\int \dot{\boldsymbol{q}}^T \mathbf{C} \dot{\boldsymbol{q}} dt$) grows globally in a monotonic fashion, perfectly matching the decay of the elastic potential energy and structural vibrations, eventually stabilizing at approximately 0.48 mJ. However, cumulative dissipative work alone is not enough to account for the entire energy dissipation. For the satellite to reach the target, the controller plays an active role in energy dissipation during the transient response phase by correctly applying torques to counteract those generated by CSI.

Finally, the logarithmic scale (Subplot 3) confirms that in the phases where the control torque does not assume significant values that actively perturb the vibratory dynamics related to CSI, the potential energy decays linearly on a logarithmic scale, i.e., exponentially over time.

Conclusions. To conclude this Closed-Loop analysis, it is fundamental to emphasize the significance of this balance: the controller actively compensate for the kinematic deviations of the Hub, and its interaction with the flexible appendages is energy-active. Once in the vicinity of the steady-state error, the algorithm allows natural damping to extinguish vibrations autonomously.

The analysis of the control law's response to the Plant's parametric uncertainties is investigated in the next section. This allows for verifying that the control law is capable of robustly guiding the satellite to the established mission target.

5.2 Robustness Validation against Parametric Uncertainties

In this section, the robustness of the proposed ASMC is evaluated with respect to parametric uncertainties. The mathematical model presented in Chapter 2, Section 2.1, is designed as a fully parametric non-linear model, allowing for rapid simulation campaigns by varying system

parameters and testing different operational scenarios.

Sensitivity analysis is initially conducted by varying a single parameter affected by uncertainty. Subsequently, a Monte Carlo campaign is performed by crossing the maximum uncertainty values associated with each individual parameter.

5.2.1 Sensitivity Analysis on Individual Uncertain Parameters

The first investigation conducted is a parametric sensitivity analysis performed by evaluating the variation of a single parameter at a time. The aim is to evaluate the robustness of the control law and the tuning of ASMC under non-nominal operating conditions. In a real space application, it is indeed of fundamental importance to properly quantify and manage the impact of uncertainties and external disturbances. These represent inherent modeling errors, unmodeled dynamics (such as the excitation of higher-order flexible modes or complex Sloshing phenomena), as well as the natural variation of physical parameters due to the wear of mechanical components and the thermal excursions in orbit.

A set of uncertain parameters is defined, associating a plausible range of variation with each. Through simulation, the impact of each individual altered parameter on the dynamic response of the system will be evaluated. The purpose of this analysis is to verify the controller's ability to ensure rapid and stable convergence toward the target, in strict compliance with the pointing requirements defined in Section **??**. During these tests, the disturbance torques are forced to their maximum allowable values; conversely, parameters whose variation is not under study maintain the nominal values reported in Table 3.1.

Particular attention is paid to (CSI). Parametric uncertainties cause a mismatch between the model used by the controller and the physical reality (flexible Plant), leading the controller to generate commands characterized by an oscillatory component. If not properly managed, the interaction between these commands and the flexible appendages could cause energy injection into the structure's vibration modes, triggering dangerous resonances and instabilities.

From the perspective of ASMC, parametric uncertainties translate into external disturbance torques. Indeed, the controller expects feedback behavior consistent with the nominal rigid model used to calculate $\boldsymbol{\tau}_{cmd}$, which is characterized by Euler's dynamics (Eq. 4.7) and a constant inertia tensor J_{tot}. Any deviation of the real state from this nominal dynamics is interpreted by the algorithm as a generalized disturbance torque.

The task of counteracting such deviations is assigned to robust torque component. To ensure convergence to the target in uncertain scenarios, it may be necessary to increase the estimate of the maximum disturbance amplitude $|D_{max}|$ and, consequently, raise the minimum safety budget guaranteed by the robust term (JK_{min}). It is essential to ensure that the increase in the robust margin never leads to the saturation of RW, constantly preserving the control authority necessary to reject external stresses.

In this discussion, the minimum robust torque budget JK_{min} previously employed is used, increasing it only if required. A rigorous analytical derivation of the optimal minimum value of JK_{min} suitable for guaranteeing stability as a function of each individual uncertain parameter is beyond the scope of this work and is deferred to future analyzes.

It is noted that the strength of ASMC designed in Chapter 4 theoretically allows to ensure robustness and stability by varying only the parameter JK_{min}, without intervening in other parameters that will adapt in turn, avoiding actuator saturation.

To perform the simulation and evaluate the impact of each individual parameter, a new *MATLAB* script is executed, which leverages two scripts already defined in Appendix A.2 and Appendix A.5. In this case, the new values related to the flexible Plant are calculated automatically for each iteration and stored in an ordered structure. The simulation code A.5 is executed for each configuration, and the results are plotted on the same graphs during the Post-Processing phase. In this way is performed a direct comparison between the dynamic responses under study.

1. Uncertainty in Damping ζ. An uncertainty is applied to the damping value. This parameter is the most critical to estimate and yet remains one of the most important, as it plays a fundamental role in the energy dissipation within the system. To simulate a critical scenario, the value of ζ is set to zero, in contrast to the nominal value of $\zeta_{nom} = 0.005$.

Damping governs the exponential decay rate of the potential energy. In a system without damping, it could be assumed that the oscillations-inevitably arising from the application of a torque commanded by the controller to guide the satellite toward the target—would remain undamped. In such a case, the flexible disturbance $\boldsymbol{\tau}_{flex}$ would persist over time. If the structure continued to vibrate, the angular rate $\boldsymbol{\omega}$ would struggle to enter the established Safe Zone, and requirements **R1** and **R2** might not be met.

This test is theoretically the most interesting, as it allows for an understanding of whether and how the controller contributes to energy dissipation to guide the satellite toward the target.

Results Analysis. The analysis of the results highlights the value of ASMC. Initially, as previously mentioned, one might assume that the sole dissipative contribution in the system was attributable to the presence of the structural damping coefficient ζ. Instead, it is observed that the energy dissipation and the time decay of flexible vibrations are not entrusted solely to the material properties but are largely determined by the control system, which plays a fundamental role. From this new perspective, it is demonstrated that the controller does not act merely as a Passive Damper—guiding the satellite toward the target while avoiding energy injection into the oscillatory components generated by the commanded torque $\boldsymbol{\tau}_{cmd}$—but effectively functions as an Active Damper (Active Damping phenomenon).

Every time the panel oscillates, it exerts a reaction force on the Hub. The ASMC law

senses a small kinematic error and instantaneously commands an equal and opposite torque to the motors to guide the Hub back to the reference, without triggering dangerous resonances. In this way, the motors contribute to the dissipation of the elastic energy trapped within the appendages.

The damping value $\zeta = 0$ does not significantly alter the system response compared to the nominal case ($\zeta = 0.5\%$). The controller successfully steers the satellite to the target, and only minor differences can be appreciated by observing Figure 5.17 and Figure 5.18.

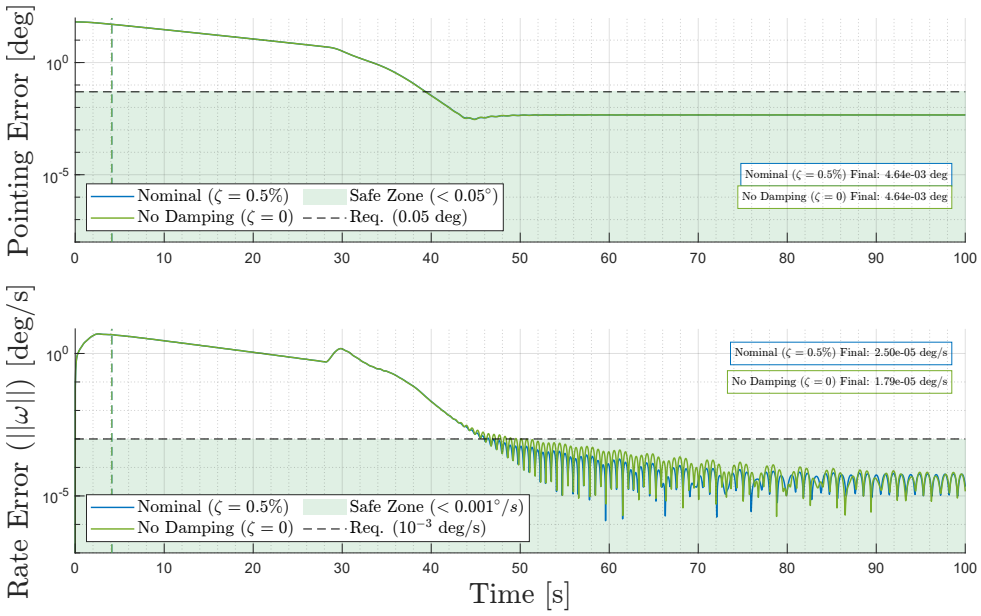

Figure 5.17: Pointing accuracy and stability analysis on a logarithmic scale. The upper graph shows the decay of the total attitude error relative to the 45° target, while the lower graph illustrates the damping of angular velocities (jitter). Both quantities settle stably below their respective tolerance thresholds (**R1** $< 0.05°$, **R2** $< 10^{-3}$ deg/s) highlighted by the green bands. A small difference is noted between the blue curve (Nominal Case) and the green one (Undamped Case).

From Subplot 2 in Figure 5.18, it is noted that the cumulative energy dissipated in the system through structural damping is not sufficient to account for the total magnitude of energy dissipation over time.

The bottom graph (Subplot 3) highlights the role of the structural damping coefficient ζ. When set to the nominal value $\zeta = 0.5\%$, it ensures that energy is dissipated more rapidly over time, especially where the control action is negligible.

However, it must be emphasized that the presence of system delays related to sensor and actuator dynamics, as well as latencies associated with data transmission and processing by the on-board computer—not modeled in this design phase—could trigger dangerous CSI and subsequent instabilities. More detailed evaluations will certainly need to be conducted in a subsequent design phase.

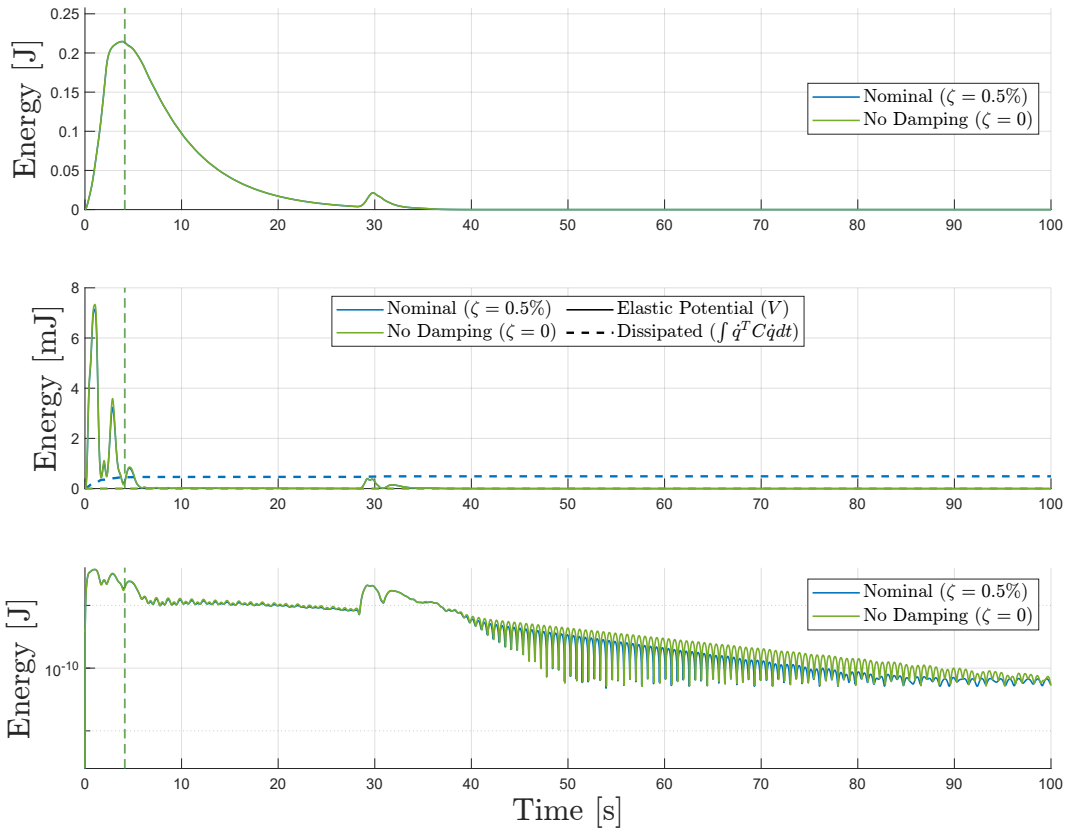

Figure 5.18: System energy balance. Total mechanical energy decays asymptotically (top). Elastic energy (middle and bottom on a logarithmic scale) dissipates over time without excitation of flexible dynamics. The blue curve represents the nominal case, while the green curve represents the undamped case.

2. Uncertainty in the Natural Frequency of the Panels. The natural frequency of the panels' vibration modes represents one of the most uncertain parameters. Natural frequencies measured on the ground are never identical to the actual ones in orbit within a 0-g environment; furthermore, the extreme thermal gradients in space change the stiffness of the materials, thereby altering the frequencies. The panels are constrained by hinges and rotary joints. Manufacturing tolerances, mechanical backlash, and unmodeled dynamics in the connection between the central Hub and the flexible appendages represent an additional source of uncertainty in the transmission of the flexible torque $\boldsymbol{\tau}_{flex}$ and the natural frequencies.

A conservative uncertainty of $\pm 20\%$ is applied to the nominal value of the natural frequencies of the modes associated with rotational deformations η_r. The analysis is set up by simulating the system's dynamic response using natural frequency values at the lower limit ($\Delta\omega_n = -20\%$) and the upper limit ($\Delta\omega_n = +20\%$) of the allowable range. The natural frequencies associated with the nominal case are:

$$[f_{n,\text{Flapping}};\ f_{n,\text{In-Plane Bending}};\ f_{n,\text{Torsional}}] = [0.25\text{ Hz};\ 0.50\text{ Hz};\ 0.80\text{ Hz}]$$

The lower limit is [0.20 Hz; 0.40 Hz; 0.64 Hz]. The upper limit is [0.30 Hz; 0.60 Hz; 0.96 Hz].

The variation of the natural frequency associated with the isolated flexible appendages significantly modifies the natural vibration frequencies of the coupled system and, consequently, CSI, which can become potentially critical. The controller might interact with the flexible appendages, amplifying the flexible disturbance torque $\boldsymbol{\tau}_{flex}$ and causing dangerous resonances.

To evaluate the impact of such uncertainty, the system response is simulated using the currently available robust torque budget JK_{min}, potentially increasing the budget allocation until robustness is restored.

Results Analysis. The analysis of the results shows that the natural frequency of the panels effectively modifies the transient response of the system due to the change of CSI. A 20% decrease in the natural frequency of the panel directly translates into a more severe excitation of the flexible dynamics, clearly visible in Figure 5.19. The Tip displacement of Panel 1 reaches a greater amplitude at lower frequencies and, furthermore, these oscillations persist for a longer duration.

The controller commands control torques of different magnitudes and with different frequency content to ensure rapid error convergence to zero in the presence of the flexible disturbance torque $\boldsymbol{\tau}_{flex}$, as visible in the graph in Figure 5.20. From an energetic perspective, it is noted once again in Figure 5.21 that although no major differences emerge from a macroscopic point of view, the system characterized by lower natural frequencies accumulates more potential energy over time and engages the structure more significantly in energy dissipation. Once the control system exerts negligible torques and the error is near zero, the potential energy is dissipated linearly on a logarithmic scale (Subplot 3).

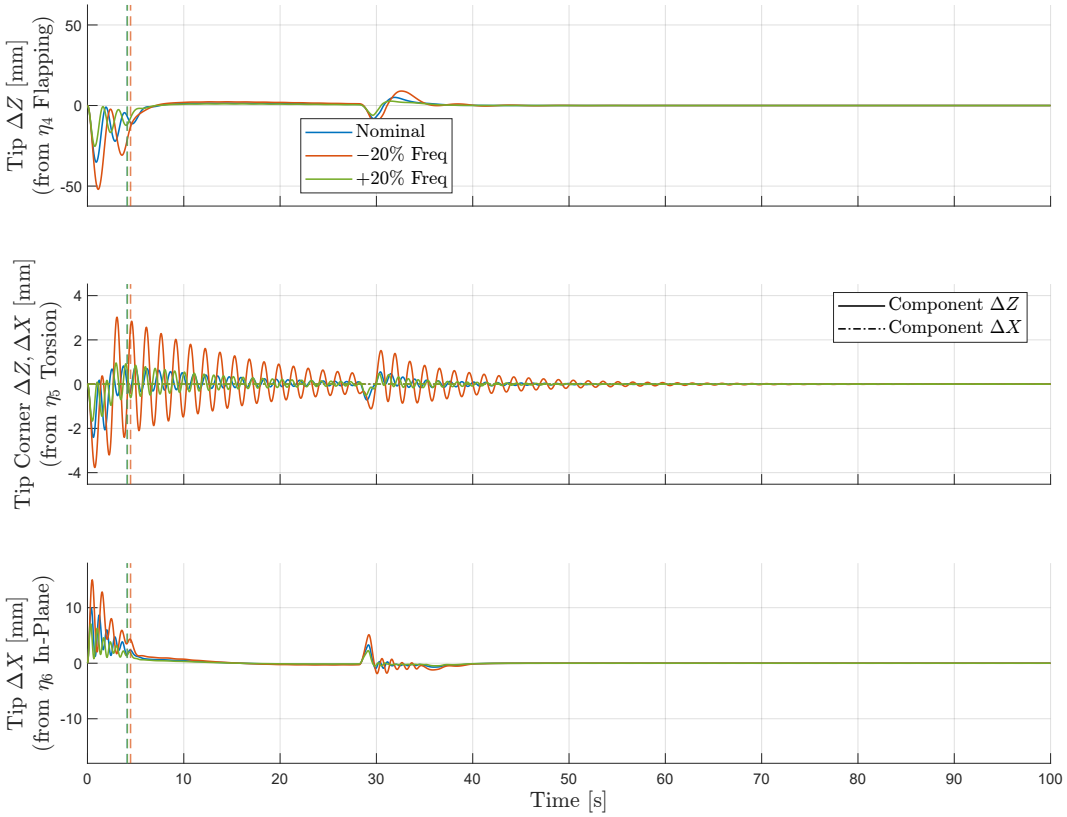

Figure 5.19: Linear displacement at the ends of the solar panels (Tip Displacement). The graph refers to Panel 1.

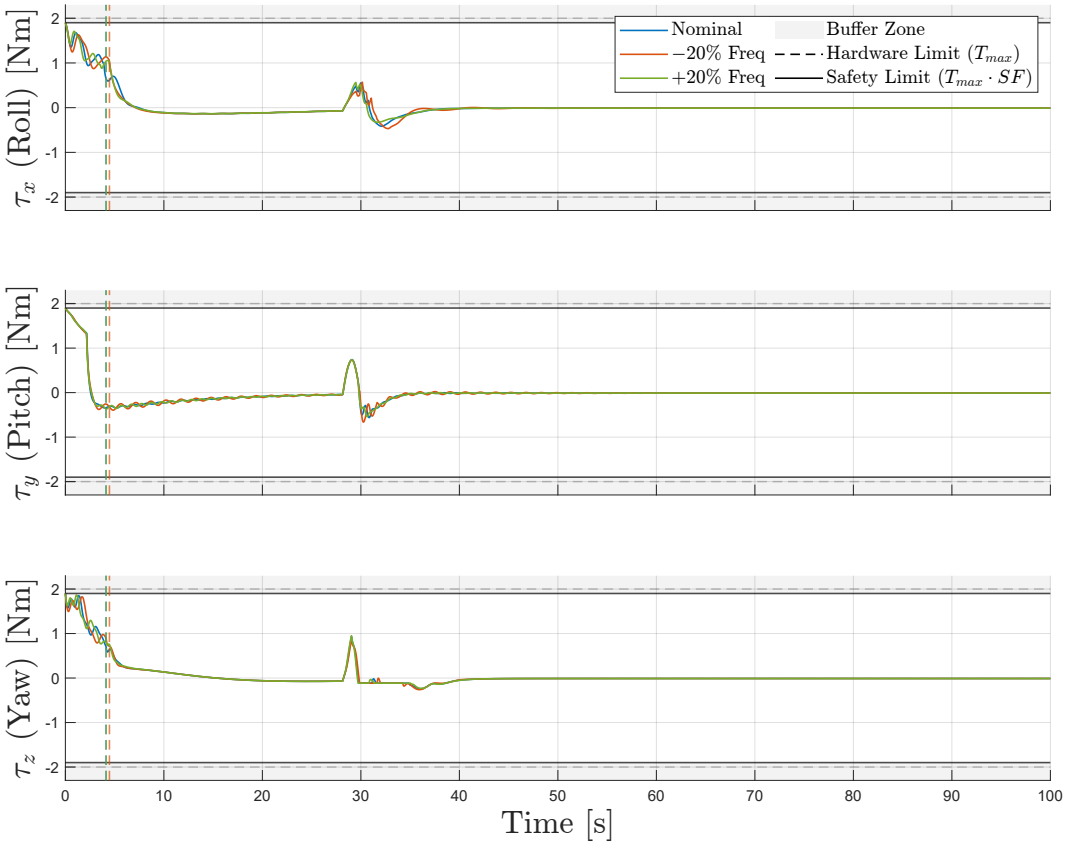

Figure 5.20: Time profile of the global control effort. The maneuver requires a high initial torque to overcome the system's inertia. Subsequently, it settles to a lower value without ever violating the physical or operational limits of the actuators. The control torques exhibit different frequency content.

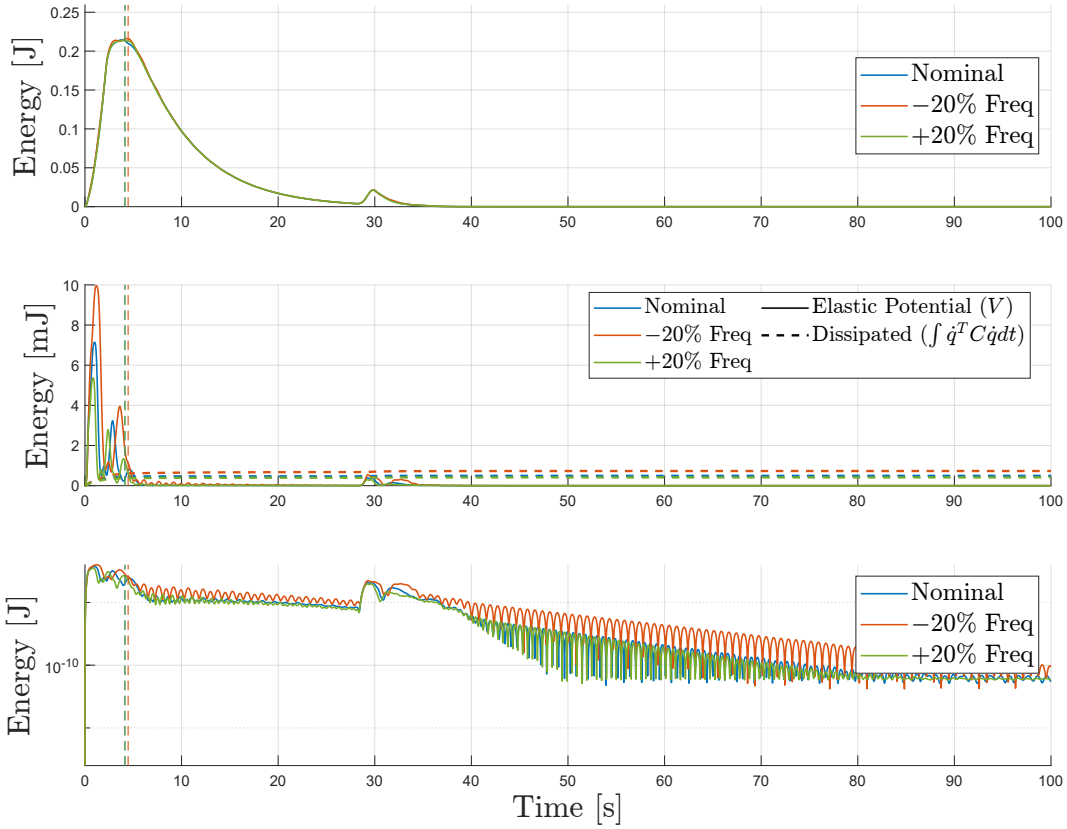

Figure 5.21: System energy balance. Total mechanical energy decays asymptotically (top). Elastic energy (middle and bottom on a logarithmic scale) dissipates over time without excitation of flexible dynamics.

The robust margin JK_{min} is sufficient to guarantee a stable response and compliance with requirements **R1** and **R2**, as shown in Figure 5.22.

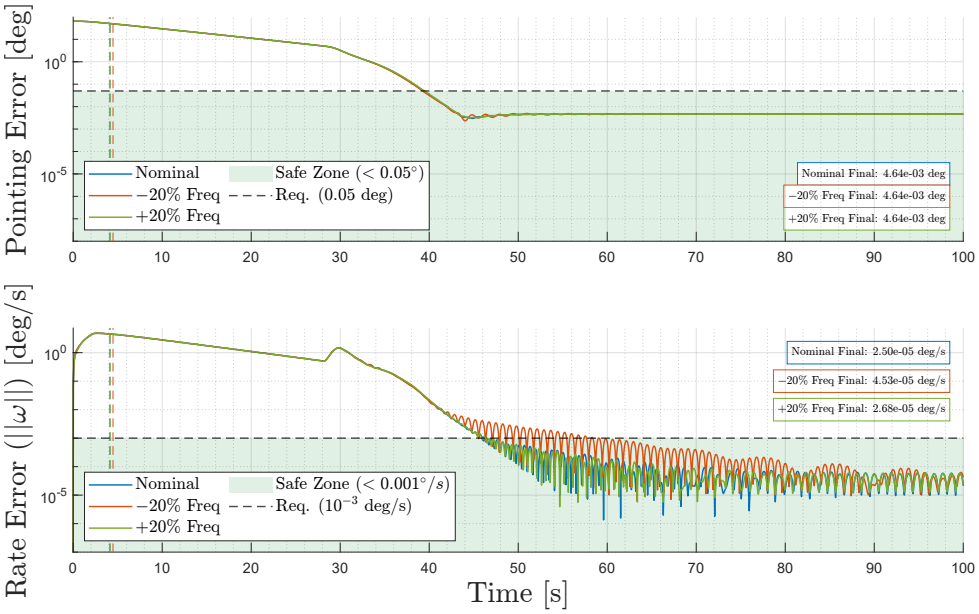

Figure 5.22: Pointing accuracy and stability analysis on a logarithmic scale. The upper graph shows the decay of the total attitude error relative to the 45° target, while the lower graph illustrates the damping of the angular velocities (jitter).

3. Uncertainty in the Hub Inertia. The Hub inertia is a parameter potentially affected by uncertainty. During the operational life, the satellite consumes propellant, which significantly alters the inertia tensor and the system mass. Phenomena such as propellant sloshing in the tanks cause small shifts in the center of mass, which also translate into variations in the moments of inertia relative to the principal axes. To account for these primary effects, as well as a possible erroneous estimation of the mass and its distribution within the central Hub, it is necessary to estimate an uncertainty range.

A conservative uncertainty of ±20% is applied to the nominal value of the diagonal terms of the Hub inertia matrix. The simulation is performed exclusively for the two limiting cases: upper ($\Delta\mathbf{J} = +20\%$) and lower ($\Delta\mathbf{J} = -20\%$). The inertia tensor evaluated in the nominal configuration with $\alpha_{sadm} = 0°$ takes the following values:

$$J_{nom} = \begin{bmatrix} 41.6 & 0 & 0 \\ 0 & 41.6 & 0 \\ 0 & 0 & 27.0 \end{bmatrix} \text{ kg m}^2 \tag{5.7}$$

The inertia tensor for the upper and lower limit configurations takes the following values:

$$J_{low} = \begin{bmatrix} 33.28 & 0 & 0 \\ 0 & 33.28 & 0 \\ 0 & 0 & 21.60 \end{bmatrix} \text{ kg m}^2, \qquad J_{upp} = \begin{bmatrix} 49.92 & 0 & 0 \\ 0 & 49.92 & 0 \\ 0 & 0 & 32.40 \end{bmatrix} \text{ kg m}^2 \tag{5.8}$$

The controller commands a control torque $\boldsymbol{\tau}_{cmd}$ based on the Euler equation for a rigid body, considering the nominal inertia tensor of the coupled system from Equation 5.9. The variation of the inertia tensor is mathematically interpreted by ASMC as a disturbance torque $\boldsymbol{\tau}_{dist}$ that is algebraically added to the commanded torque $\boldsymbol{\tau}_{cmd}$. Modifying the Hub's inertia tensor inevitably changes the natural vibration modes of the coupled system as well. Consequently, CSI is altered, and the panels will exert flexible disturbance torques of different magnitudes on the central body. The controller must counteract both the inertia variation and a more or less severe CSI. It will be the exclusive task of the robust torque component to manage this gap, pushing the satellite toward the Sliding Surface in any case.

Although inertial uncertainty lends itself well to rigorous analytical estimation, the variation in the flexible torque reaction $\boldsymbol{\tau}_{flex}$ related to CSI is highly unpredictable.

Given the difficulty of analytically estimating the margin related to the change in CSI, the system response is simulated using the currently available robust torque budget JK_{min}, potentially increasing the budget allocation until robustness is restored.

Results Analysis. As expected, as the Hub inertia varies, the magnitude of the flexible disturbance torque $\boldsymbol{\tau}_{flex}$ changes. A Hub with lower inertia is subject to flexible disturbance actions of greater amplitude. Furthermore, the lower inertia causes more severe accelerations $\dot{\boldsymbol{\omega}}$ and modifies the time evolution of the Sliding variable. From an energetic perspective, by observing the graph in Figure 5.23, the impact of the Hub inertia variation $\boldsymbol{\Delta J}$ on the dynamics of the coupled system can be appreciated.

A heavier Hub accumulates greater kinetic energy in its motion to quickly reach the Boundary Layer, energy that is dissipated just as quickly during the braking phase (Subplot 1). A lighter Hub results in the flexible appendages accumulating more elastic energy over time, requiring the structure to engage more significantly in damping that energy (Subplot 2).

Once again, the robust margin JK_{min} is sufficient to guaranty a stable response and compliance with requirements **R1** and **R2**, as shown in Figure 5.24.

4. Uncertainty in the Mass/Inertia of the Solar Panels. The uncertainty regarding the mass and inertia properties of the solar panels is the next parameter evaluated. In this case as well, it is difficult to analytically or via *CAD* estimate the exact mass. Furthermore, during the actual testing and construction phases, the mass of the flexible appendages is often modified without the dynamic model of the software being promptly updated. In light

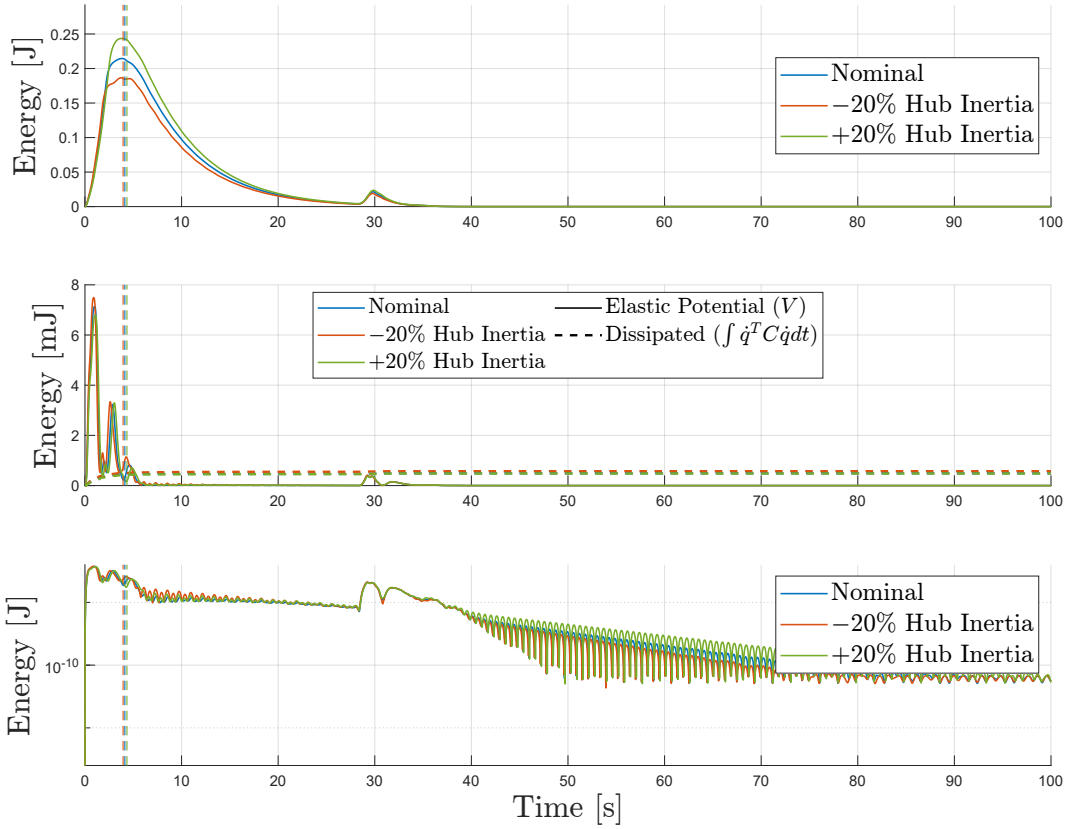

Figure 5.23: System energy balance. Total mechanical energy decays asymptotically (top). Elastic energy (middle and bottom on a logarithmic scale) dissipates over time without excitation of flexible dynamics. Note the different magnitude of the total mechanical energy peak.

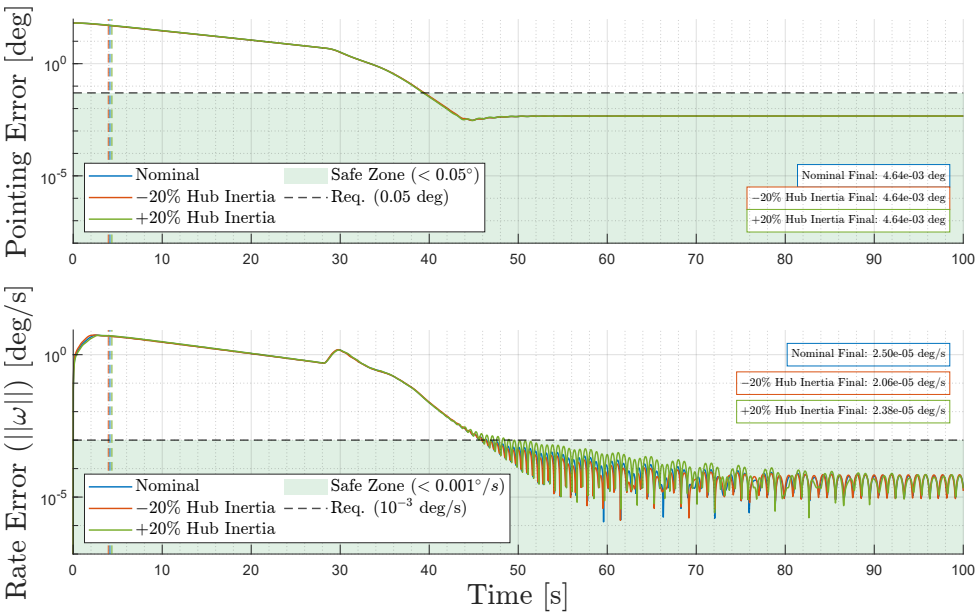

Figure 5.24: Pointing accuracy and stability analysis on a logarithmic scale. The upper graph shows the decay of the total attitude error relative to the 45° target, while the lower graph illustrates the damping of angular velocities (jitter).

of these evaluation, and aware of the approximation introduced by the approach LPA, it is necessary to establish an uncertainty range within which these parameters are varied.

A conservative uncertainty of ±20% is applied to the nominal values of the diagonal terms of the Panels' inertia matrix. The simulation is performed exclusively for the two limiting cases: upper ($\Delta\mathbf{J} = +20\%$) and lower ($\Delta\mathbf{J} = -20\%$). The inertia tensor evaluated in the nominal configuration with $\alpha_{sadm} = 0°$ takes the following values:

$$J_{nom} = \begin{bmatrix} 11.4 & 0 & 0 \\ 0 & 1.3 & 0 \\ 0 & 0 & 12.7 \end{bmatrix} \text{ kg m}^2 \tag{5.9}$$

The inertia tensor for the upper and lower limit configurations takes the following values:

$$J_{low} = \begin{bmatrix} 9.12 & 0 & 0 \\ 0 & 1.04 & 0 \\ 0 & 0 & 10.16 \end{bmatrix} \text{ kg m}^2, \qquad J_{upp} = \begin{bmatrix} 13.68 & 0 & 0 \\ 0 & 1.25 & 0 \\ 0 & 0 & 15.24 \end{bmatrix} \text{ kg m}^2 \tag{5.10}$$

The most significant effect expected on the dynamics is the variation in the maximum amplitude of the flexible disturbance $\boldsymbol{\tau}_{flex}$. The variation in the inertia of the panels modifies the flexible torque $\boldsymbol{\tau}_{flex}$ exchanged with the rigid Hub at the root attachment point. The stiffness k will also change, as it is designed to maintain the natural frequencies of the isolated panel at the target value. Finally, the natural frequencies of the coupled system will also differ, translating into a variation in CSI. In this case as well, the controller must counteract the

presence of disturbance torques $\boldsymbol{\tau}_{dist}$ caused by variations of a different nature.

To evaluate the impact of such uncertainty, the system response is simulated using the currently available robust torque budget JK_{min}, potentially increasing the budget allocation until robustness is restored.

Results Analysis. Similarly to what was observed when varying the Hub inertia, in this case as well, the variation in the response is attributed to the change in CSI. The flexible disturbance torque $\boldsymbol{\tau}_{flex}$ exhibits higher intensity peaks when the panels have higher inertia values, as shown in Figure 5.25, and this is naturally reflected in the magnitude of the control torques.

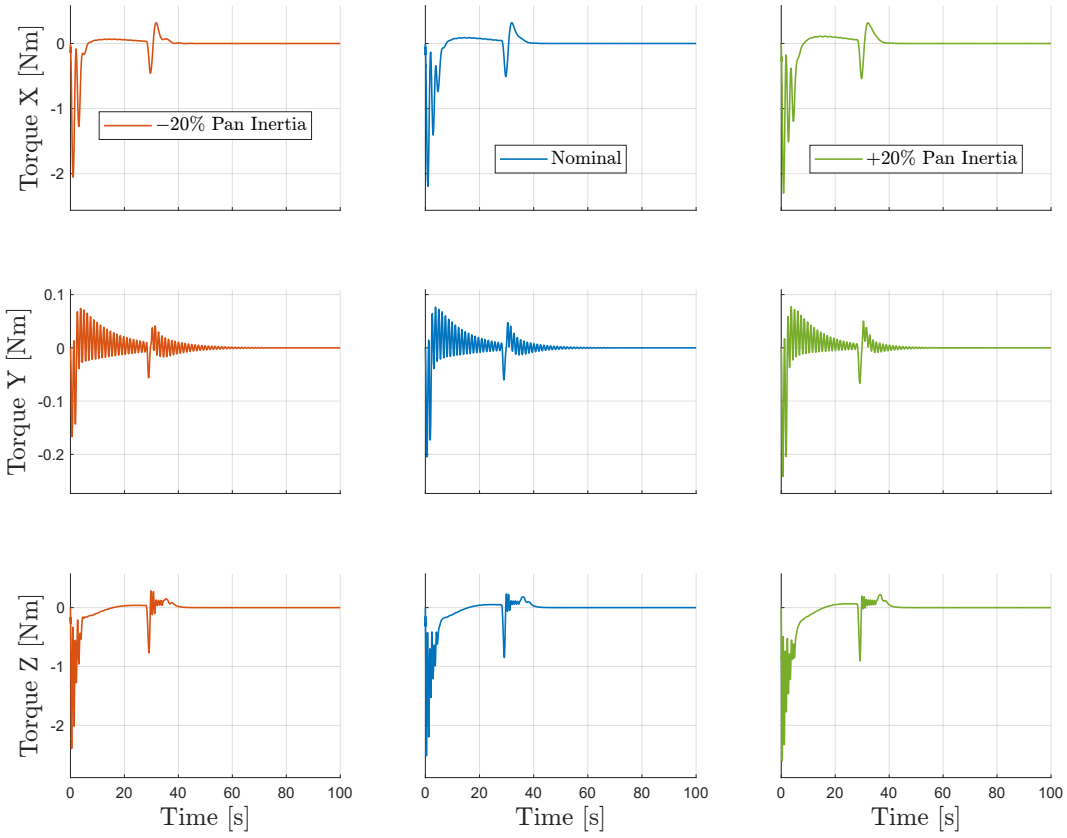

Figure 5.25: Control-Structure Interaction (CSI). The impulsive disturbance torque (τ_{flex}) generated by the deflection of the solar panel is represented for different panel inertia values.

However, the uncertainty in the inertia of the solar panels also modifies the stiffness of the system, which adapts to keep natural frequencies of the panels unchanged. The system is less stiff when the inertia of the panels is lower, and the tip displacements reach slightly higher values, as can be seen in Figure 5.26.

The control system is nonetheless capable of guaranteeing compliance with the requirements, as shown in Figure 5.27.

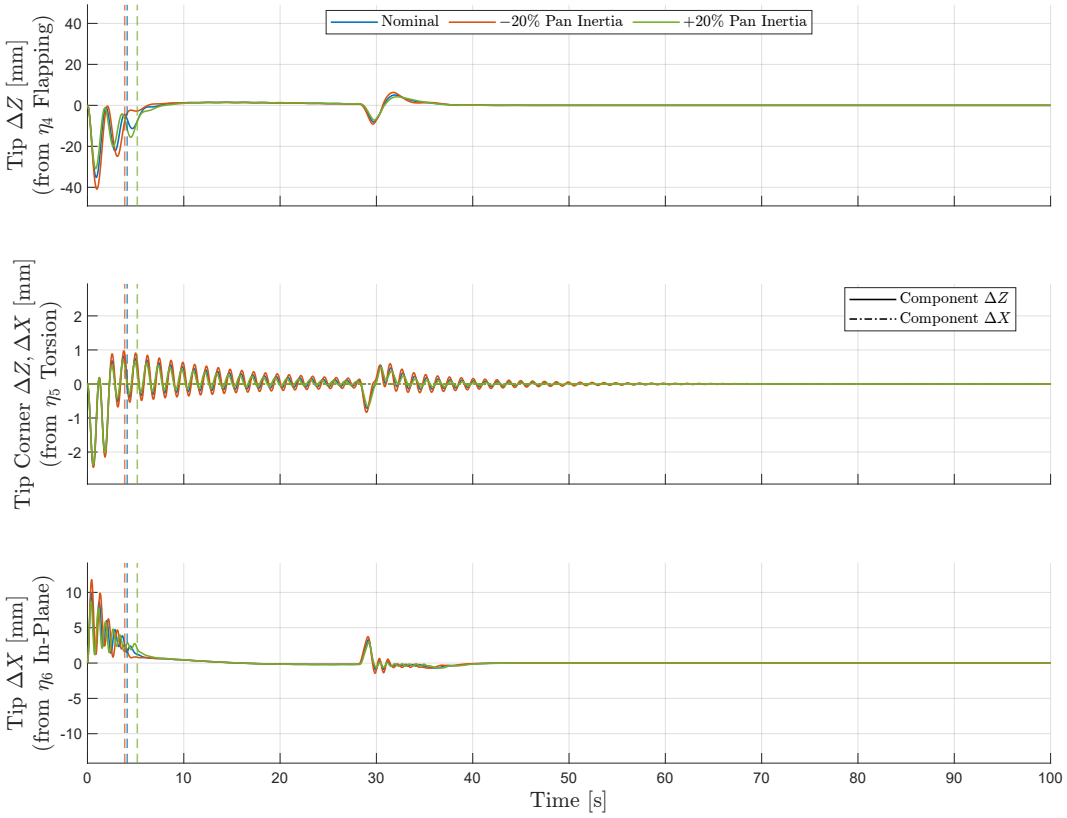

Figure 5.26: Linear displacement at the ends of the solar panels (Tip Displacement). The graph refers to Panel 1.

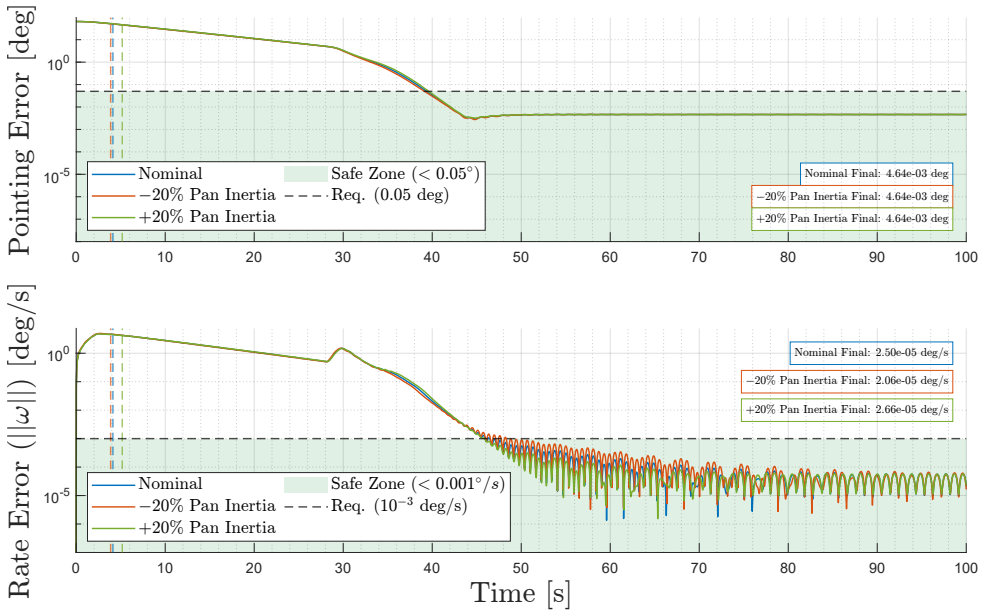

Figure 5.27: Pointing accuracy and stability analysis on a logarithmic scale. The top graph shows the decay of the total attitude error relative to the 45° target, while the graph at the bottom illustrates the damping of the angular velocities (jitter).

5. Uncertainty in the Rotation Angle α_{sadm}. The final analysis aims to evaluate the dynamic response of the coupled system in the presence of different initial rotation configurations of the solar panels relative to the root, defined by the parameter α_{sadm}. Instead of indirectly modifying the intensity of the disturbance (frequency, mass, inertia) or its duration (damping), varying α_{sadm} changes the direction of the disturbance and the distribution of the torque budget over time. This is because the appearance of products of inertia and inertial coupling between the axes will also alter the magnitude of the gyroscopic torque and, consequently, the available free budget.

This exploratory campaign will once again validate the ability of ASMC to follow a reference, its robustness in managing a coupled disturbance, and the impact on mission requirements **R1** and **R2**.

The following values for α_{sadm} are chosen in addition to the classic nominal case:

$$\alpha_{sadm} = [30°; 45°; 60°; 90°]$$

To evaluate the impact of such uncertainty, the system response is simulated once again using the currently available robust torque budget JK_{min}, potentially increasing the budget allocation until robustness is restored.

Results Analysis. The analysis shows that the system complies with the mission requirements **R1** and **R2** for different orientations of the rotation angle of the panels, as shown in Figure 5.28.

The different transient responses are stably damped by the control system.

5.2.2 Monte Carlo Analysis on All Uncertain Parameters

In this section, a simulation campaign is conducted to evaluate the control law's ability to follow the desired reference while ensuring an adequate level of robustness. This time, the maximum uncertainty values associated with each individual parameter are crossed, with the exception of the damping coefficient, which is set to the critical value $\zeta = 0$. A total of 24 different critical cases plus a single nominal case are evaluated, and the simulation results are analyzed.

Again, the developed code is not reported in the Appendix as it follows the exact same logic as the code in Appendix A.2 and the code in Appendix A.5. Once all the flexible Plant configurations are defined, the values are saved in an ordered structure, and a simulation is performed for each different configuration. The results are then saved in an ordered structure to proceed with the Post-Processing phase.

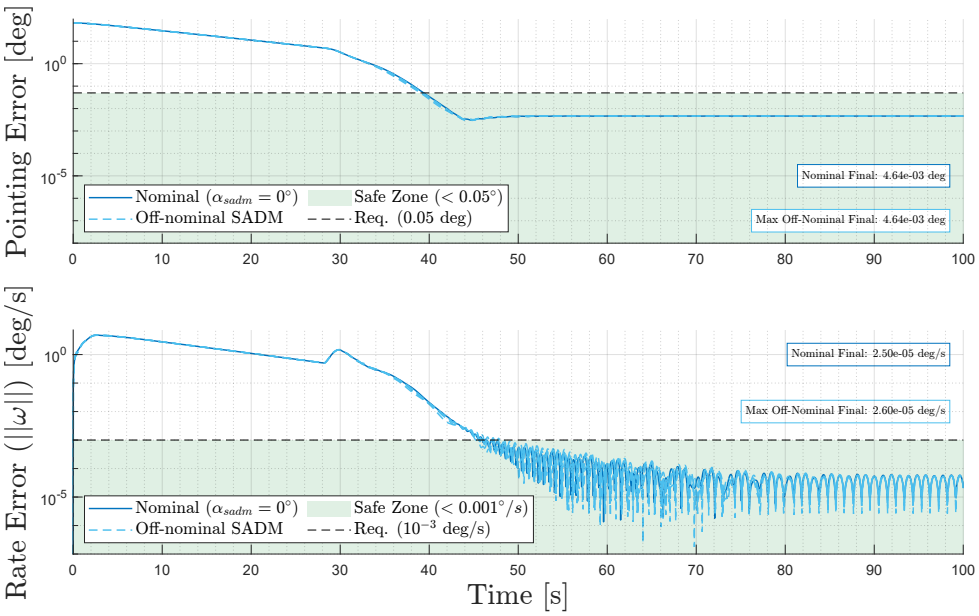

Figure 5.28: Pointing accuracy and stability analysis on a logarithmic scale. The top graph shows the decay of the total attitude error relative to the 45° target, while the graph at the bottom illustrates the damping of the angular velocities (jitter).

Results Analysis. The analysis demonstrates the robustness of the control law across all scenarios considered to be the most critical for simulation. Figure 5.29 shows compliance with requirements **R1** and **R2**, which take on different values within a band of the same color as the nominal simulation case, set in transparency, representing the envelope of the 25 curves obtained from the simulation.

CSI changes depending on the critical configuration simulated, and the maximum amplitude associated with the Tip of Panel 1 falls within an uncertainty band visible in Figure 5.30. The intensity of the commanded control torques is modified to ensure compliance with the requirements, as shown in Figure 5.31. The kinetic energy of the system also varies according to the inertia values assumed by the Hub and the panels within a limited band. Due to the different values of the flexible disturbance torque $\boldsymbol{\tau}_{flex}$ applied to the system and as a function of the different natural vibration frequencies, the accumulation of elastic potential energy also changes, as visible in Subplot 2 in Figure 5.32.

Finally, Figure 5.33 shows the uncertainty band within which the adaptive parameters of the control law, Λ and JK_{min}, vary. The controller modifies the command action on the system to effectively modulate the dynamic response according to the different uncertain values of the parameters, ensuring that the torque margin JK_{min} is maintained and mission requirements are met.

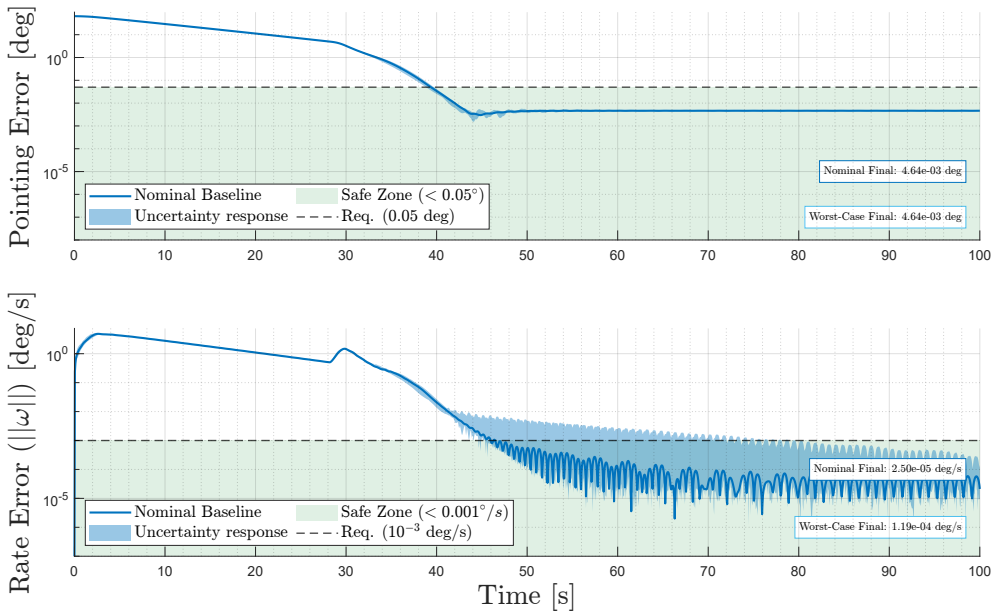

Figure 5.29: Pointing accuracy and stability analysis on a logarithmic scale. The upper graph shows the decay of the total attitude error relative to the 45° target, while the lower graph illustrates the damping of the angular velocities (jitter).

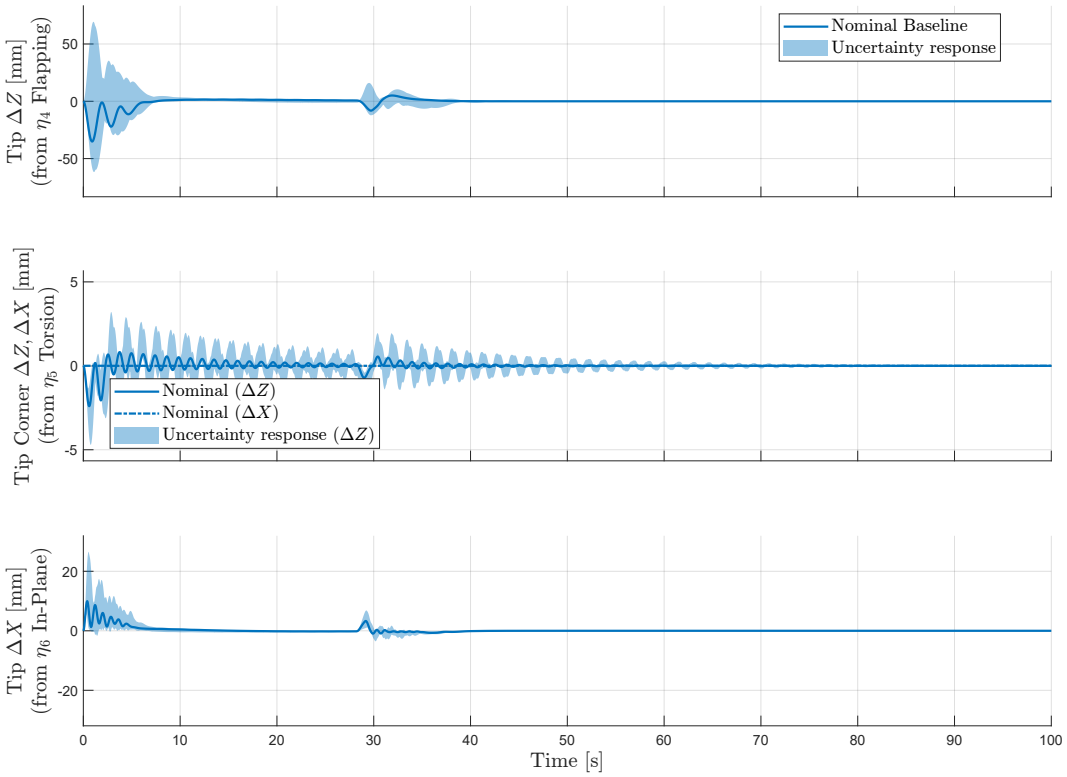

Figure 5.30: Linear displacement at the ends of the solar panels (Tip Displacement). The graph refers to Panel 1.

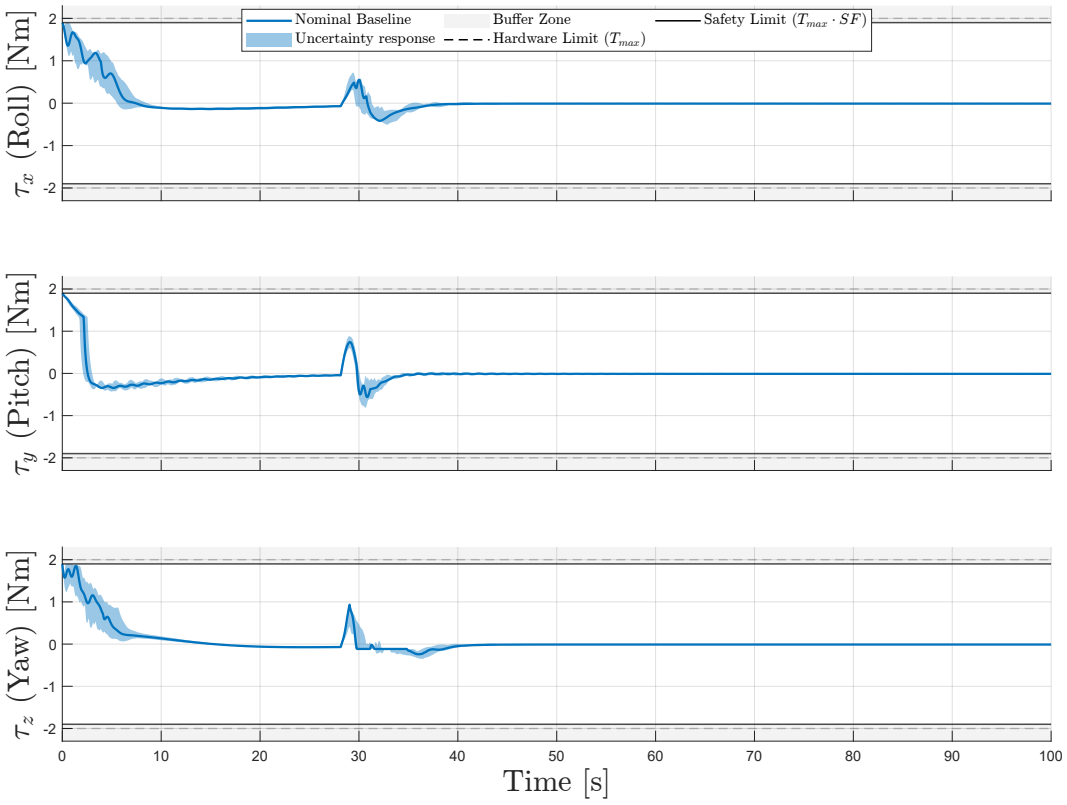

Figure 5.31: Time profile of the global control effort.

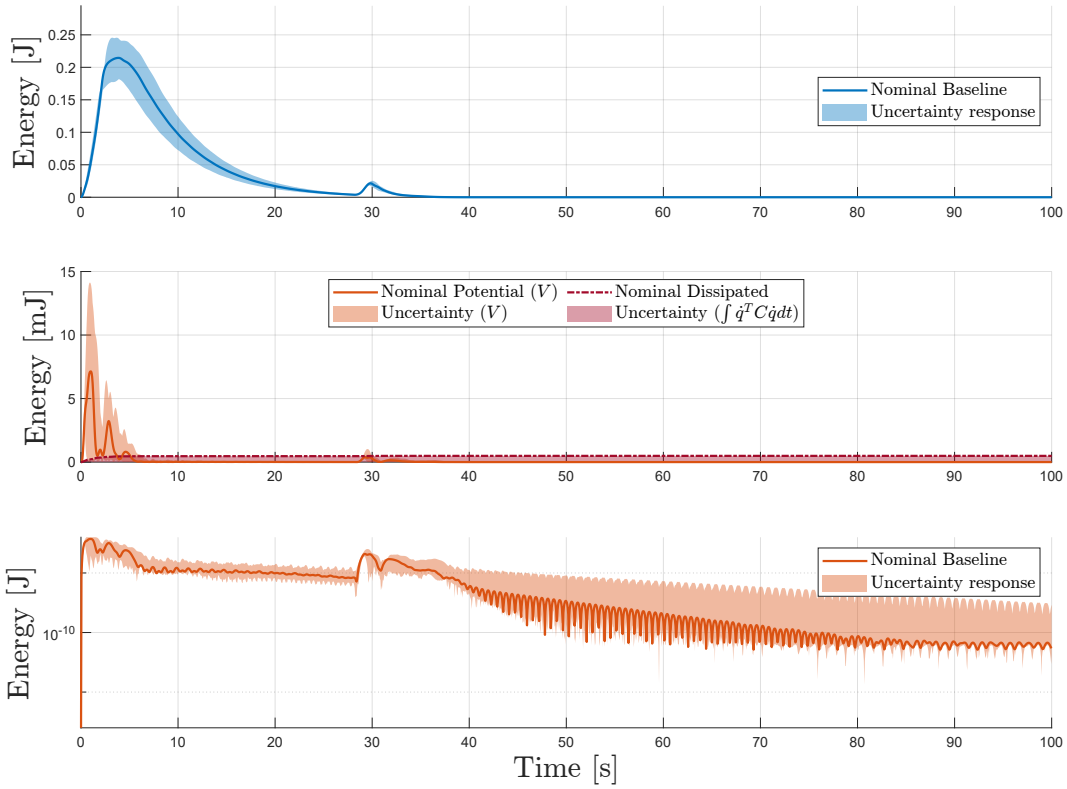

Figure 5.32: System energy balance. Total mechanical energy decays asymptotically (top). Elastic energy (middle and bottom on a logarithmic scale) dissipates over time without critical excitation of flexible dynamics.

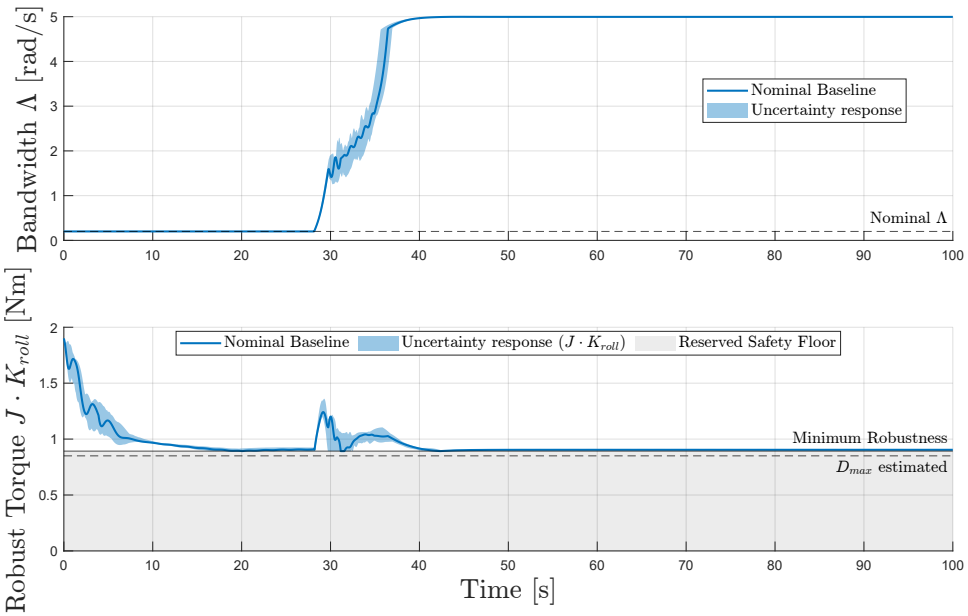

Figure 5.33: Evolution of adaptive parameters: smooth transition of the parameter Λ_{act} (top) and directional allocation of the robust gain $J \cdot K$ (bottom). The shaded area represents the impassable operational safety limit, below which the robustness and stability of the method are no longer guaranteed.

5.3 Robustness validation against changes in the operational scenario

Finally, a last analysis is performed by varying the simulated scenario to stress the control system and verify that the satellite reaches the established target. In this case, the goal is to represent the **Deployment Shock** phenomenon. Following separation from the launcher and an initial coarse stabilization, the solar panels are deployed. This impulsive operation introduces a different set of initial conditions. The satellite acquires a residual angular velocity of $\boldsymbol{\omega} = \pm 1°/\text{s}$, and the appendages begin to vibrate with an estimated maximum amplitude of up to 1° at the root, generating a maximum tip displacement of approximately 8 mm. At this point, at time $t = 0$, ASMC is activated to execute the rotation maneuver LASM.

Once the nominal configuration of the satellite is fixed, 8 different initial states are generated by combining the maximum and minimum angular velocity values at time $t = 0$ across the different rotation axes. For each case, 4 independent deformed configurations for each of the two solar panels are extracted in an absolutely random and reproducible manner. The total number of simulated initial states amounts to 32.

In this case, the possible excitation of different mode shapes compared to those studied in the nominal case could cause a significant CSI, taking on a completely different form and amplitude depending on the initial conditions. By performing this analysis, it will be evaluated whether ASMC is capable of driving the error to zero in times comparable to the

nominal case, in compliance with mission requirements **R1**, **R2** and **R3**, without amplifying the flexible oscillations and, in contrast, actively damping them. Furthermore, it will be possible to qualitatively analyze how the exchange of flexible torques between the Hub and the appendages changes as a result of different initial conditions.

Results Analysis. From the analysis of the results, several very interesting aspects emerge, which once again allow for an interpretation of the control law's performance and highlight both its strengths and weaknesses.

The graph in Figure 5.34 highlights the satellite's attitude behavior over time; the graph in Figure 5.35 shows the time profile of the angular velocities. The transparent band, highlighting the envelope within which the kinematic variables vary, settles at the target value.

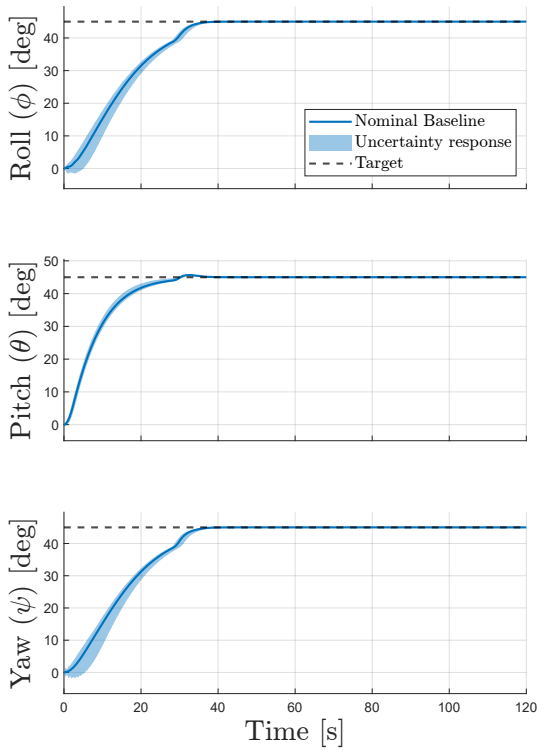

Figure 5.34: Time evolution of the Euler angles.

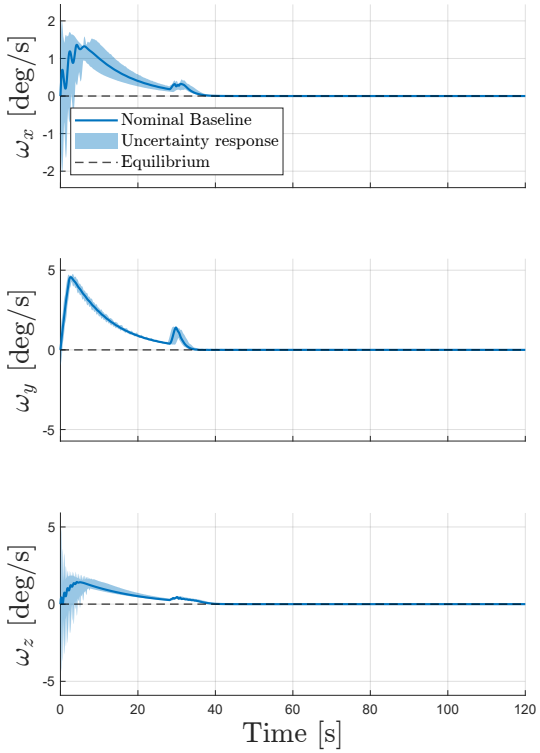

Figure 5.35: Time evolution of the angular velocities $\boldsymbol{\omega}$.

ASMC system manages to simultaneously handle the rejection of the initial disturbance caused by $\boldsymbol{\omega} \neq 0$ and the maneuver tracking, without ever becoming unstable in any of the 32 simulated cases. The pointing requirement **R1** is met and falls within the Safe Zone (the green area in Figure 5.36). However, requirement **R2** regarding jitter is not satisfied during the first 120 seconds of the maneuver.

From the analysis of the flexible torques exchanged by the appendages with the central Hub in Figure 5.37, the limitations of the control law clearly emerge. Depending on the initial condition, ASMC acts on the Hub by attempting to nullify the angular velocity error

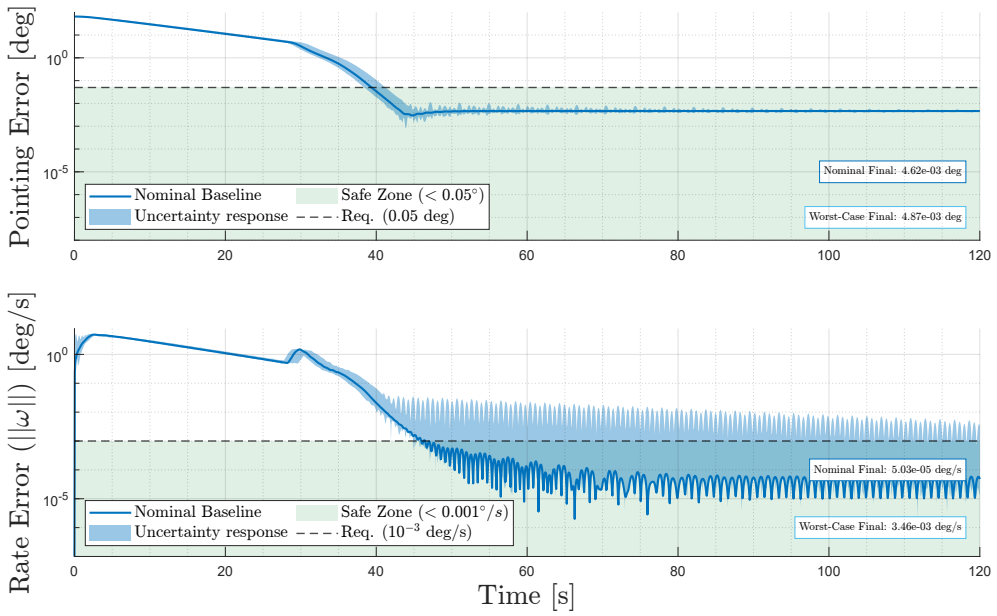

Figure 5.36: Pointing accuracy and stability analysis on a logarithmic scale. The upper graph shows the decay of the total attitude error relative to the 45° target, while the lower graph illustrates the damping of the angular velocities (jitter).

$\boldsymbol{\omega}$ by commanding a specific torque $\boldsymbol{\tau}_{cmd}$. This torque may add in-phase with the reaction torque $\boldsymbol{\tau}_{flex}$ exchanged with the flexible appendages, which are in a generic deformed state, consequently increasing the deflection of the flexible appendages. This can create violent disturbance torques on the satellite's motion, causing it to diverge from the target, which must then be counteracted at full power by ASMC. ASMC is programmed to deliver a maximum of $T_{max} = 2.0$ Nm; however, to effectively damp the magnitude of the exchanged flexible torques, it might require commanded torques greater than the maximum deliverable torque. This phenomenon leads to severe CSI, potential actuator saturation, and a reduced capacity of the controller to handle the active damping of the accumulated potential energy.

Kinetic energy is asymptotically damped over time, as seen in Subplot 1 of Figure 5.38, while Subplot 2 highlights the criticality related to the potential energy. Compared to the nominal case, the potential energy reaches significantly higher values and persists for almost the entire duration of the simulation, as can be appreciated by observing the envelope of the work done by the Rayleigh damping coefficient to dissipate the accumulated energy.

In Figure 5.39, the magnitude of the torques applied to the flexible Plant by the control system is shown, compared to the nominal case, in order to overcome the CSI and stabilize the satellite around the desired target.

The uncertain envelope of this torque exhibits high-frequency components, especially in the initial phase and during the stage where the parameter Λ begins its transition toward the Λ_{max} value. The Sliding variable in Figure 5.40 is also subject to strong oscillations due to CSI; in its uncertain envelope, it can be observed how the Boundary Layer is reached at dif-

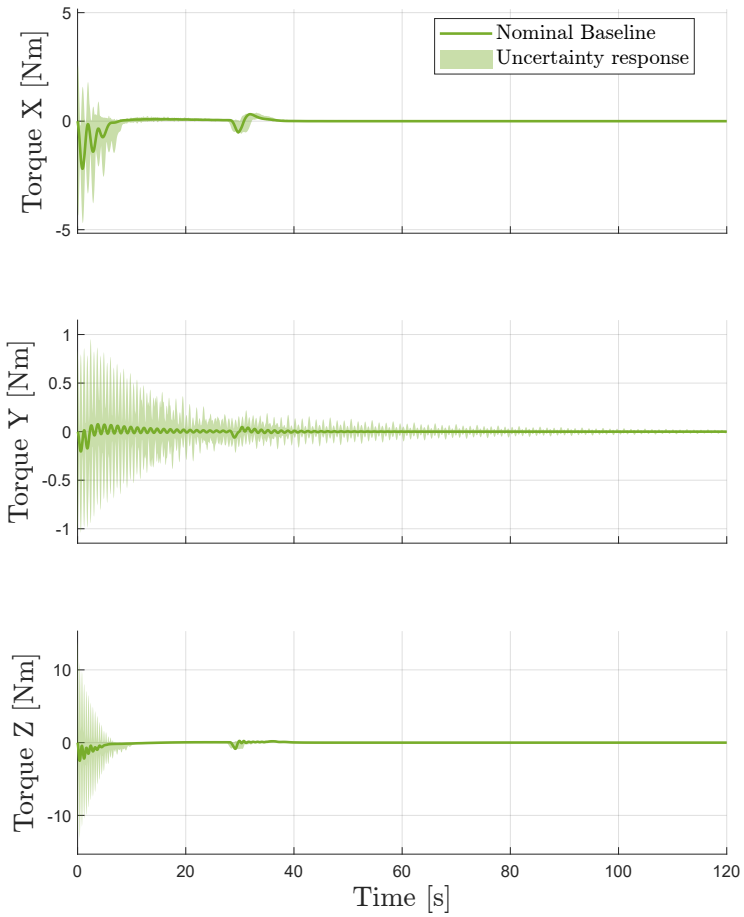

Figure 5.37: Flexible torques $\boldsymbol{\tau}_{flex}$ exchanged between the Hub and the flexible appendages over time.

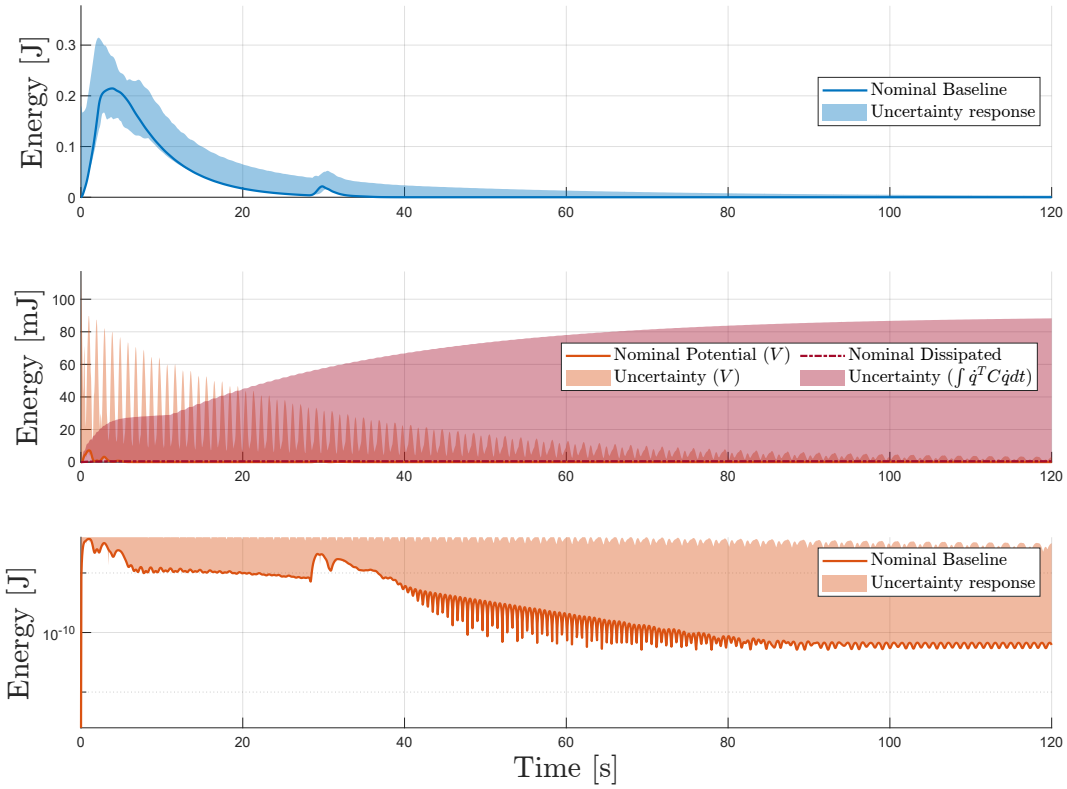

Figure 5.38: System energy balance. Total mechanical energy decays asymptotically (top). Elastic energy (middle and bottom on a logarithmic scale) persists over time due to the strong CSI interaction.

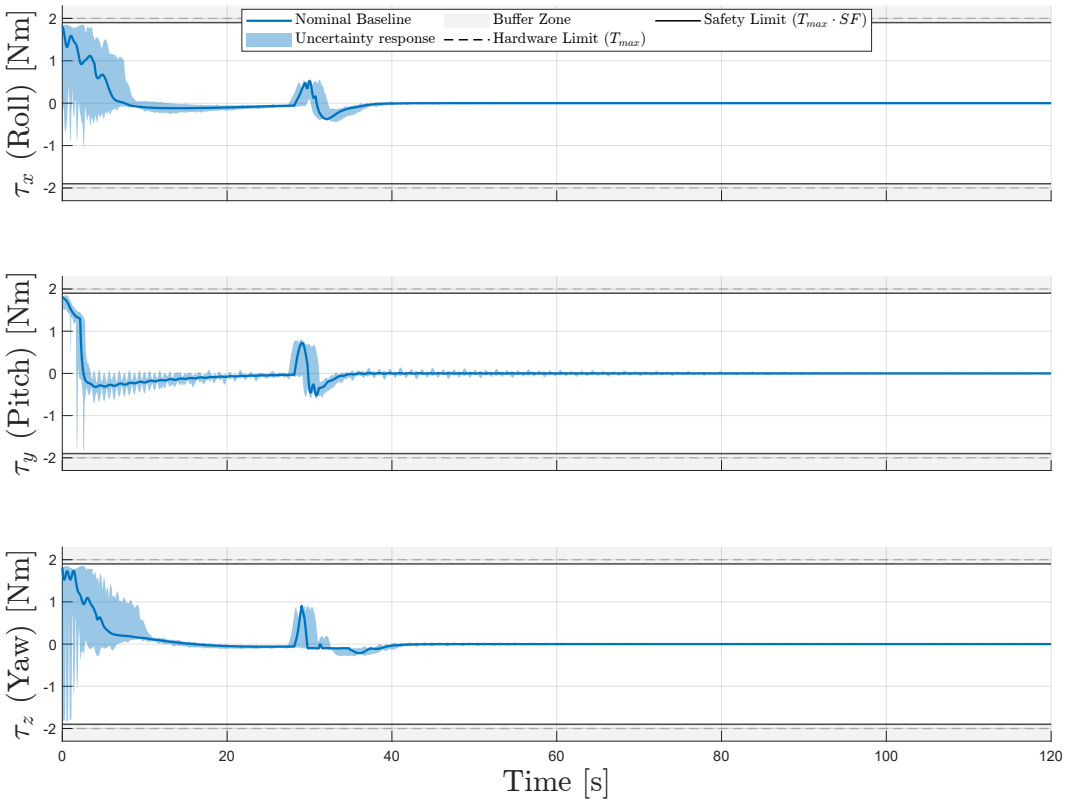

Figure 5.39: Time profile of the torque $\boldsymbol{\tau}_{app}$ applied to the flexible Plant.

ferent times and through different dynamics. Despite this observation, the controller remains capable of bringing the system into Sliding Mode, thanks to the time-varying allocation of the parameters. These take on values within the envelope described in Figure 5.41, depending on the instant the threshold angle θ_{th} is reached and the torque budget available to counteract the disturbance torques.

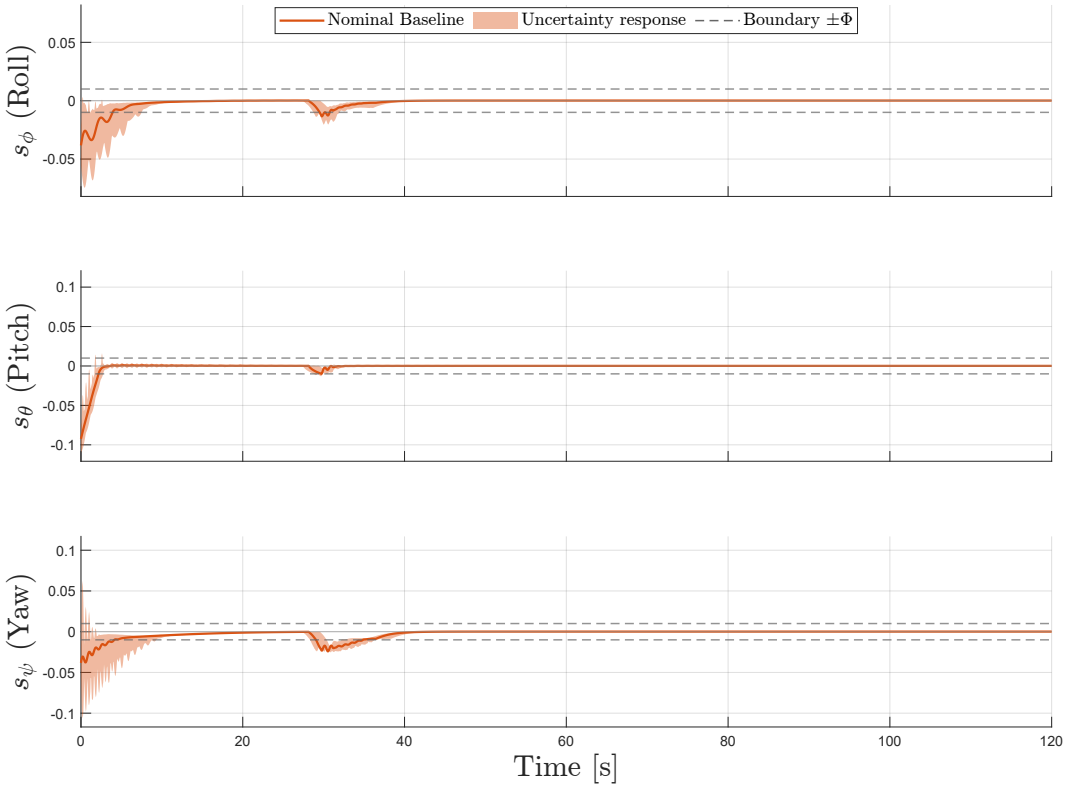

Figure 5.40: Time evolution of the sliding variables s. The trajectories nullify the large initial misalignment but enter the Boundary Layer $\pm\Phi$ at different times and following different trajectories.

To conclude the analysis, the graph that most clearly highlights the limitations of the current control law is presented in Figure 5.42. The initial flexible vibrations are inevitably excited during LASM and reach critical values within the uncertain envelope. This not only delays the satellite's response toward the reference target but also increases the energy consumed by the actuators to counteract the disturbance torques. A situation arises where the Hub reaches the desired attitude, but the flexible deformations have not been effectively damped by the control system during the motion.

As shown again in Figure 5.36, requirement **R1** is met; however, these strong residual vibrations around the equilibrium condition are only perceived by the control system as small perturbations on the Hub's angular velocity. The bulk of the dissipative work is left to the structural damping, which, having a very low value, does not contribute effectively to energy dissipation within the simulation timeframe (120 seconds).

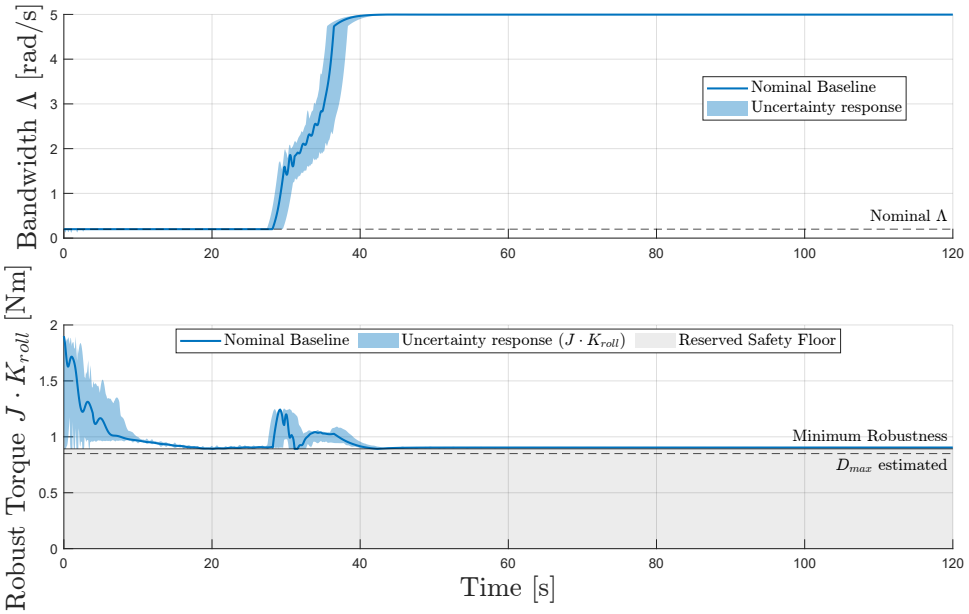

Figure 5.41: Evolution of adaptive parameters: smooth transition of the parameter Λ_{act} (top) and directional allocation of the robust gain $J \cdot K$ (bottom). The shaded area represents the impassable operational safety limit below which the robustness and stability of the method are not guaranteed.

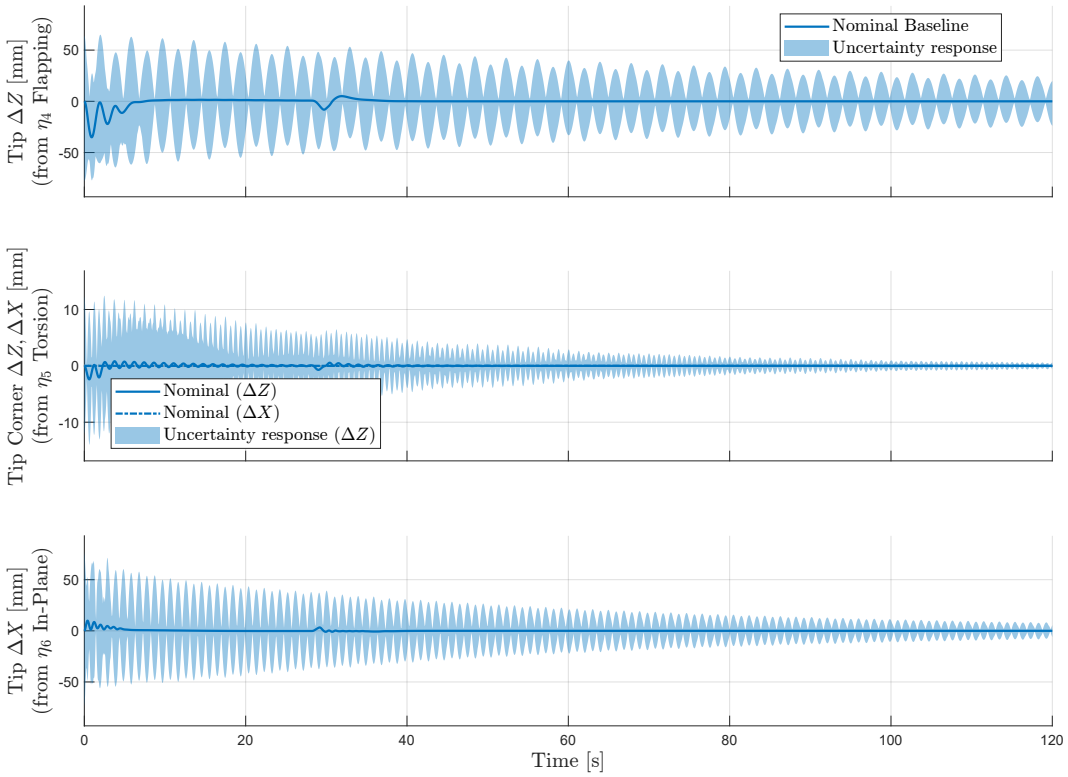

Figure 5.42: Linear displacement at the ends of the solar panels (Tip Displacement). The graph refers to Panel 1.

The system is an **under-actuated system**. ASMC acts only on the central Hub by absorbing the elastic energy that is transferred to it, but it cannot act directly on the panels. Consequently, energy takes time to be dissipated, especially when starting from non-zero initial conditions.

The results show that for missions characterized by stringent requirements, attitude-only control has physical limits when dealing with large initial deformations. Future developments could integrate piezoelectric materials on the panels (*Strain Rate Feedback*) to be coupled with ASMC on the Hub for a hybrid control approach.

Chapter 6

Conclusions and Future Perspectives

Contents

6.1 Critical review of the work and results obtained 111
6.2 Recommendations for future research 113

6.1 Critical review of the work and results obtained

This thesis was developed with the objective of investigating the dynamic interaction between the attitude control system and structural flexibility (Control-Structure Interaction, CSI) in modern space platforms, focusing specifically on the execution of Large Angle Slew Maneuvers (LASM).

The fundamental first step in addressing this problem was the development of a multi-body non-linear mathematical model, capable of representing a rigid central body (Hub) coupled with two large flexible appendages. The fully parametric nature of this model proved to be a key strategic choice: it allowed not only for the agile definition of the satellite's geometric and inertial configuration but also for the creation of a structured simulation environment for subsequent analyses. The Open-Loop validations, supported by modal analysis and energy balances, demonstrated the physical consistency of the simulator. Despite its relative simplicity, the model proved capable of faithfully capturing the phenomenon of Dynamic Coupling, specifically, the way in which appendage vibrations affect the Hub's attitude and vice versa.

Once the simulation environment was validated, the focus shifted to the controller synthesis. Meeting stringent mission requirements—such as a final pointing error of less than 0.05° and a residual jitter below 10^{-3} deg/s—while executing a 45° multi-axis maneuver under strict physical constraints on the maximum torque deliverable by the Reaction Wheels, requires an advanced strategy.

For this reason, an Adaptive Sliding Mode Control (ASMC) law was implemented. The main contribution of this architecture lies in its adaptive Budget Allocation logic: the controller dynamically adjusts the time-varying control parameter Λ and the robustness gains

based on the kinematic error and the estimated disturbances. This ensures fast reference tracking without incurring harmful, prolonged actuator saturation.

The Closed-Loop validation confirms the effectiveness of the proposed architecture. In the nominal case study, even in the presence of maximum environmental and internal disturbance torques (such as propellant sloshing effects or non-nominal actuator performance), the controller proved robust, completing the maneuver within a short timeframe. However, the most compelling results emerged during the sensitivity analysis campaigns. Varying the parametric uncertainty (masses and inertias, natural frequencies, structural damping, and panel rotation angles)—culminating in the simulation of a combined set of extreme worst-case scenarios—highlighted the true role of the control law in managing the CSI interaction.

During the maneuver, the ASMC does not merely compensate for disturbance torques but acts as a true **Active Damper**. To keep the Hub on the ideal trajectory, the controller reacts to the flexible torques $\boldsymbol{\tau}_{flex}$ exerted by the panels by generating equal and opposite torques. In doing so, the control system performs mechanical work that dissipates elastic energy from the system, effectively dampening vibrations within reasonable times even when assuming a material with zero structural damping ($\zeta = 0$).

The final phase of the work pushed the system to its physical limits by simulating a severe operational scenario: the **Deployment Shock**. In this scenario, the satellite does not start from rest but possesses uncontrolled residual initial angular velocities, and the appendages already exhibit large deflections. This investigation, while demonstrating the absolute global asymptotic stability of the controller (capable of recovering the satellite in all tested cases), brought to light the primary physical limitation of this control architecture.

This limitation lies in the under-actuated nature of the system: the actuators are located exclusively on the central Hub. Since the controller reacts only to the Hub's kinematic error, once the Hub has reached the target and remains stationary within the pointing tolerance, the control action is drastically reduced. If, at that moment, the panels still possess high elastic energy (due to large initial deformations and complex CSI developed during the maneuver), the magnitude of the vibration is not sufficient to generate a Hub error large enough to trigger an aggressive control response. Consequently, the problem becomes "transparent" to the controller: unable to act directly on the appendages, it must passively wait for the vibrational energy to slowly transfer to the central body before it can be damped, resulting in very long vibration decay times. This phenomenon leads to high energy consumption due to continuous actuation effort and causes large oscillations that can result in excessive and critical structural stress on the panels.

This evidence demonstrates that, no matter how robust and adaptive an attitude control law is made, it cannot entirely replace the need for direct dissipation on the structures when dealing with large flexible appendages.

6.2 Recommendations for future research

The critical issues identified and the strong simplifying assumptions adopted to isolate the physical phenomena in this work provide a solid foundation for future research developments. Potential advancements can be grouped into four main macro-areas:

1. Refinement of the dynamic model and simulation environment. The Lumped Parameter Model LPA used in this study proved excellent for preliminary analysis. However, to simulate high-fidelity scenarios, it is necessary to transition to Finite Element Modeling (FEM). This would allow for the inclusion of a larger number of vibration modes, precise definition of the natural frequencies of the panel, and the capture of complex non-linear behaviors typical of large rotating structures, such as Centrifugal Stiffening or the Spin Softening phenomenon. Furthermore, the assumption of fixed solar panels during the maneuver should be removed: simulating the active rotation of the panels (SADM dynamics) concurrently with the LASM would add a further level of realism. Finally, to bridge the gap between simulation and reality, the Closed-Loop simulation architecture should be enhanced by incorporating sensor measurement noise, processing and computational latencies, and, most importantly, the actual dynamics of the actuators, coupled with a more sophisticated modeling for the simulation of disturbance torques.

2. Evolution of the control architecture. The proposed adaptive law yields excellent results but possesses significant margins for optimization. A primary improvement could involve the adaptation law of the Λ parameter, making the transition from the nominal to the maximum value even smoother to soften the control action and optimize the various maneuver phases. Additionally, obtaining an analytical estimate of the minimum robustness gain JK_{min} would be of great interest. Looking forward, the technique used in this thesis could be replaced by or compared with frontier variants of Sliding Mode Control SMC, such as Integral Sliding Mode Control (ISMC) or Super-Twisting Sliding Mode Control (STSMC).

3. Hybrid control and sensing for under-actuated structures. As evidenced by the simulations, the physical limit of a standard attitude controller is the impossibility of acting directly on the appendages. For missions requiring ow structural fatigue and absolute pointing stability even in the face of large initial shocks, Hub-only actuation is insufficient. An extremely promising development consists of combining the ASMC technique developed in this thesis with linear robust control algorithms (such as H_∞ synthesis or μ-synthesis). The idea is to create a hybrid controller: the ASMC controller would manage the aggressive and non-linear reorientation maneuver, while the H_∞ controller, leveraging frequency-domain design, could act near the target to ensure maximum disturbance rejection and actively dampening residual micro-vibrations. From a hardware perspective, to ensure effective disturbance rejection and manage these complex scenarios, this would translate into the integration of piezoelectric actuators bonded directly to the panels (Strain Rate Feedback), coupled with state-of-the-art strain sensors, such as fiber optic sensor networks. The use of optical fibers, a

field where much of today's aerospace research is concentrated, would allow the exact deformation state of the structure to be sent to the controller in real-time, solving the under-actuation problem at its root.

4. Experimental validation. The final and fundamental step consists of migrating the codes developed in this work from a purely numerical environment (Software-in-the-Loop, SITL) to a physical testbed (Hardware-in-the-Loop, HITL). Testing the control law on physical attitude simulators would represent the definitive proof to validate the effectiveness and robustness of the algorithm in the real world.

Appendix A

Explanation and Execution Guide for MATLAB Scripts

This appendix serves as a guide to understanding and executing the software architecture developed in the *MATLAB* environment for the simulation and control of the flexible satellite. The main scripts are presented in chronological and logical execution order. For each module, a flow chart is provided that describes the operations performed by the script and the functions upon which the script depends.

A.1 Symbolic Derivation of the Equations of Motion

The script `N01_Derive_Satellite_Equations.m` represents the first module in the chronological execution order of the entire software architecture. This code derives the equations of motion for the 18-degree-of-freedom flexible satellite using symbolic computation, based on the Euler-Lagrange energy approach described in Chapter 2. This script only needs to be executed once for a given topological configuration of the satellite. The generated output consists of a set of *MATLAB* functions ready to be called at each integration step by the subsequent numerical simulation scripts.

As illustrated in the flow chart in Figure A.1, the logical sequence of operations performed by the code is structured into the following steps:

1. Setup and State Definition: The code initializes the symbolic computation environment (using the `syms` command) by defining the time t, the constant geometric and inertial parameters of the system (mass, dimensions, offsets, and static SADM angles), and the stiffness/damping parameters. The state vector $\mathbf{q}(t) \in \mathbb{R}^{18}$ is constructed, divided into the rigid coordinates of the Hub ($\mathbf{q}_{hub}$) and the relative deformation coordinates for the two appendages ($\mathbf{q}_{flex,1}, \mathbf{q}_{flex,2}$), and its time derivatives $\dot{\mathbf{q}}(t)$ are calculated.
2. Kinematics chain: In this phase, the elementary rotation matrices are constructed, and the kinematic chains are defined. For the central Hub, the linear and angular velocities projected into the Body Frame are extracted. For flexible appendages, the code rigorously defines the position vectors of the centers of mass, taking into account the radial rigid offset, the static rotation of the joint, and the local deformation coordinates. Finally, the absolute translational and rotational velocities of the solar panels are derived.

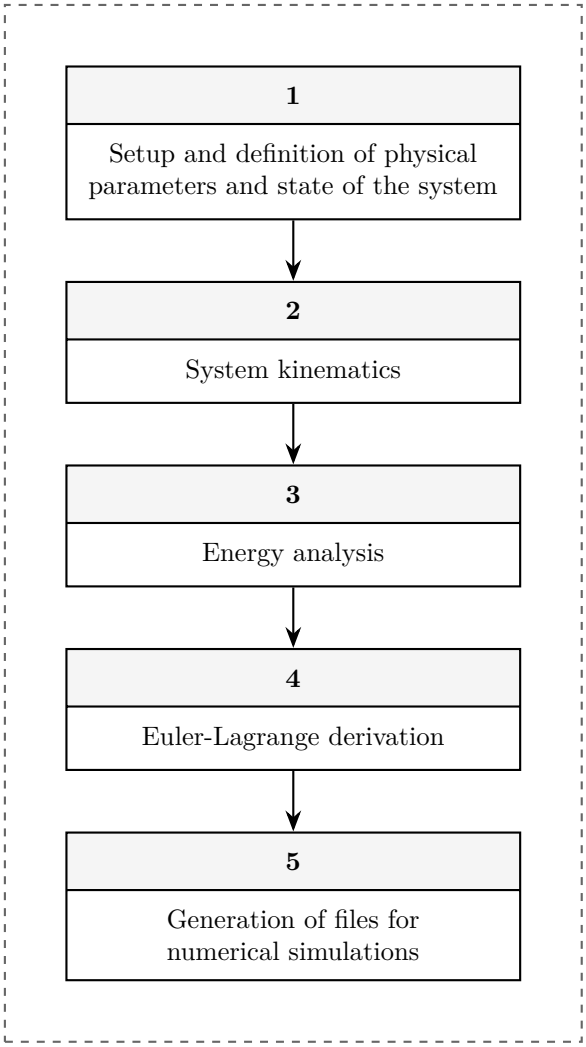

Figure A.1: Logical flowchart of the `N01_Derive_Satellite_Equations.m` script for the symbolic generation of the dynamic model.

3. Energy Analysis: Leveraging the kinematic quantities calculated in the previous step, the script formulates the scalar state functions: the total Kinetic Energy of the system (T_{tot}), the Elastic Potential Energy concentrated at the joints (U_{tot}), and the Rayleigh Dissipation Function (D_{tot}). The combination of these terms allows for the formal definition of the Lagrangian function $\mathcal{L}$.

4. Euler-Lagrange Derivation: This constitutes the algebraic core of the script. The code extracts the individual matrix blocks using the *MATLAB* Jacobian operator:

   - The mass matrix $\mathbf{M}(\mathbf{q})$ is extracted as the Hessian of the kinetic energy with respect to the generalized velocities.
   - The Coriolis and centrifugal vector $\mathbf{h}(\mathbf{q}, \dot{\mathbf{q}})$ is isolated by calculating the time derivative of the mass matrix (using the spatial chain rule for computational efficiency) multiplied by $\dot{\mathbf{q}}$, subtracting the spatial gradient of the kinetic energy.
   - The elastic vector $\mathbf{k}_{el}$ and the damping matrix $\mathbf{C}_{damp}$ are derived from the gradient of the potential energy and the dissipation function, respectively.

5. Generation of numerical simulation files: Once the symbolic extraction is complete, using the `matlabFunction` command, the code automatically generates four external files: `get_MassMatrix.m`, `get_CoriolisVector.m`, `get_ElasticVector.m`, and `get_DampingMatrix.m`. These functions are optimized to take the instantaneous numerical state as input and return the matrix structures required for numerical integration and the calculation of accelerations.

A.2 Model Setup, Tuning, and Modal Analysis

The `N02_Step1_CompleteModel_Setup.m` script constitutes the second operational module. This code numerically initializes the nominal case study, performs the tuning of the elastic parameters, and derives the modal shapes of the system. This script must be executed prior to any dynamic simulation, as it generates the fundamental data structures required by the numerical integrator.

As illustrated in the global flow chart in Figure A.2, the logical sequence of operations and the respective calls to external functions are structured into the following points:

1. Initialization of Geometric and Inertial Parameters: The code acquires the panel orientation angle α_{sadm} (user-configurable) and numerically defines the masses, geometric dimensions, and isolated inertia tensors for the Hub and flexible appendages.

2. Inverse Tuning (Stiffnesses and Dampings): Having defined the target natural frequencies of the flexible modes (Translational, Flapping, In-Plane, and Twist), the script queries the `get_MassMatrix.m` function (generated previously), evaluating it in the undeformed configuration ($\mathbf{q} = \mathbf{0}$). By extracting the equivalent mass/inertia from the diagonal matrix, the code analytically calculates stiffness $\mathbf{K}$ damping $\mathbf{C}$ necessary to

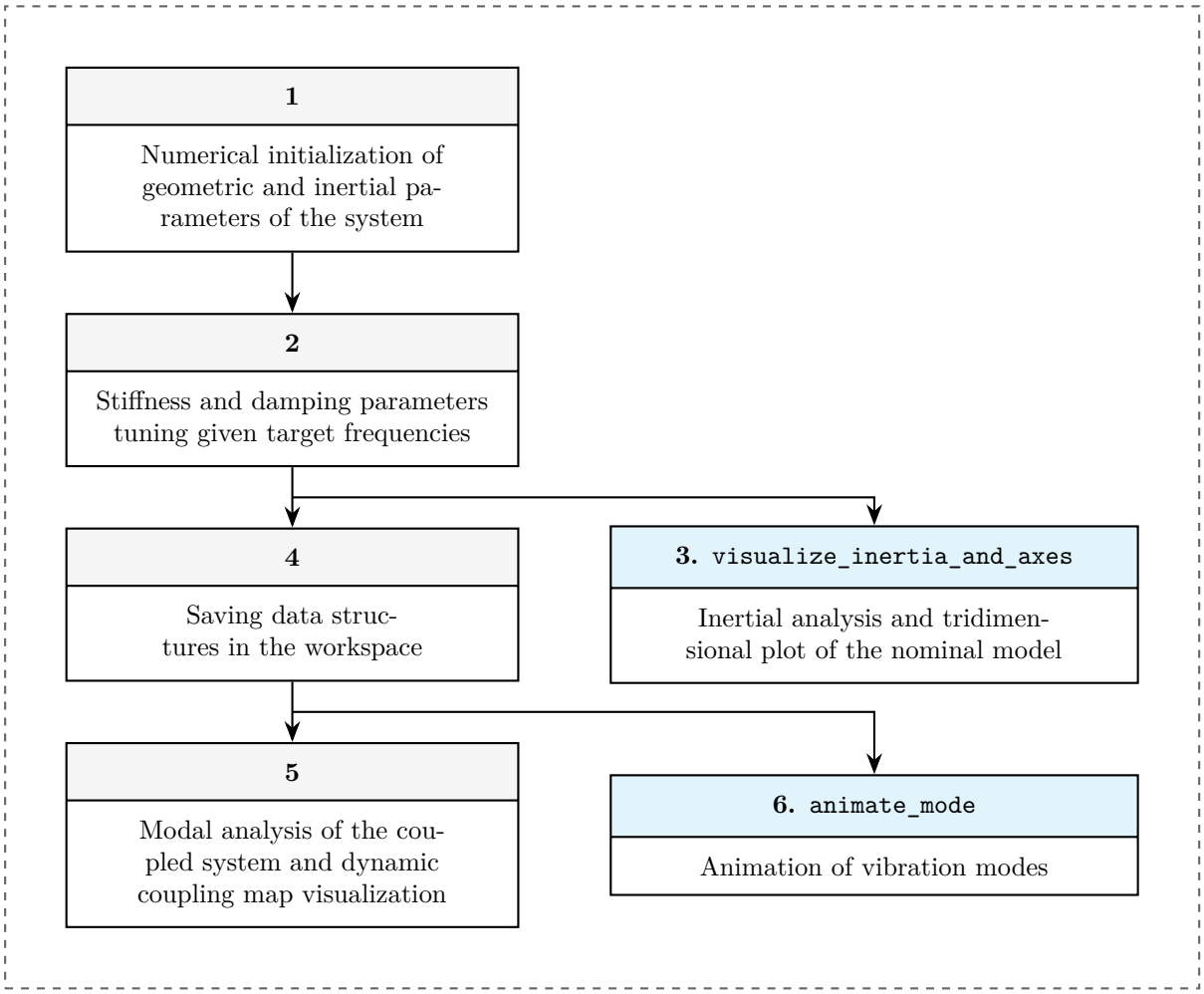

Figure A.2: Logical flowchart of the `N02_Step1_CompleteModel_Setup.m` script for the symbolic generation of the dynamic model.

guarantee the design frequencies. Finally, all parameters are packed into the ordered vectors `p_vals_RigidModel` and `p_vals_FlexModel`.

3. Call to the `visualize_inertia_and_axes.m` function: This accessory function specifically performs several important tasks:
   - Calculates the dynamic coupling ratios along the three axes.
   - Extracts the principal axes of inertia by solving the eigenvalue problem on the total tensor.
   - Generates a textual report in the Command Window and a three-dimensional figure of the un-deformed satellite with superimposed reference frames.
4. Saving to Workspace: The parameter vectors are saved in the `Satellite_Data` structure and made globally available for subsequent *MATLAB* simulations.
5. Modal Analysis and Coupling Map: Having constructed the mass ($\mathbf{M}_0$) and stiffness ($\mathbf{K}_0$) matrices at rest, the generalized eigenvalue problem is solved. The script sorts the extracted natural frequencies and automatically generates the modal coupling graphical map.
6. Call to the `animate_mode.m` function: Based on the modal analysis, this second accessory function allows the visual inspection of the vibration modes. Given the mode index chosen by the user as input, the function normalizes the corresponding eigenvector and propagates a purely harmonic oscillation (without damping). By calling a local plotter, a three-dimensional animation is generated, allowing for the qualitative identification of the geometric deformations (e.g., symmetric, antisymmetric) associated with that specific resonance.

A.3 Open-Loop Non-Linear Simulation

The script `N05_OpenLoop_FlexModel.m` serves as the dynamic simulation engine of the system. This code calculates the time evolution of the state of the satellite (rigid attitude and flexible vibrations) in response to a predetermined Open-Loop torque profile. The execution of this script is dependent on the module `N02_Step1_CompleteModel_Setup.m`, from which it imports the structure `Satellite_Data` containing the masses, geometries, and stiffness extracted for the flexible model of the satellite.

As outlined in the flow chart in Figure A.3, the simulation process unfolds through an initialization phase, a time integration loop (Main Loop), and a final post-processing phase of the results.

1. Maneuver Configuration and Initialization: The code sets the basic simulation parameters: time step (`dt = 0.001 s`), total duration, and initial conditions at rest. It also generates the time profile of the external torque $\boldsymbol{\tau}_{cmd}$.

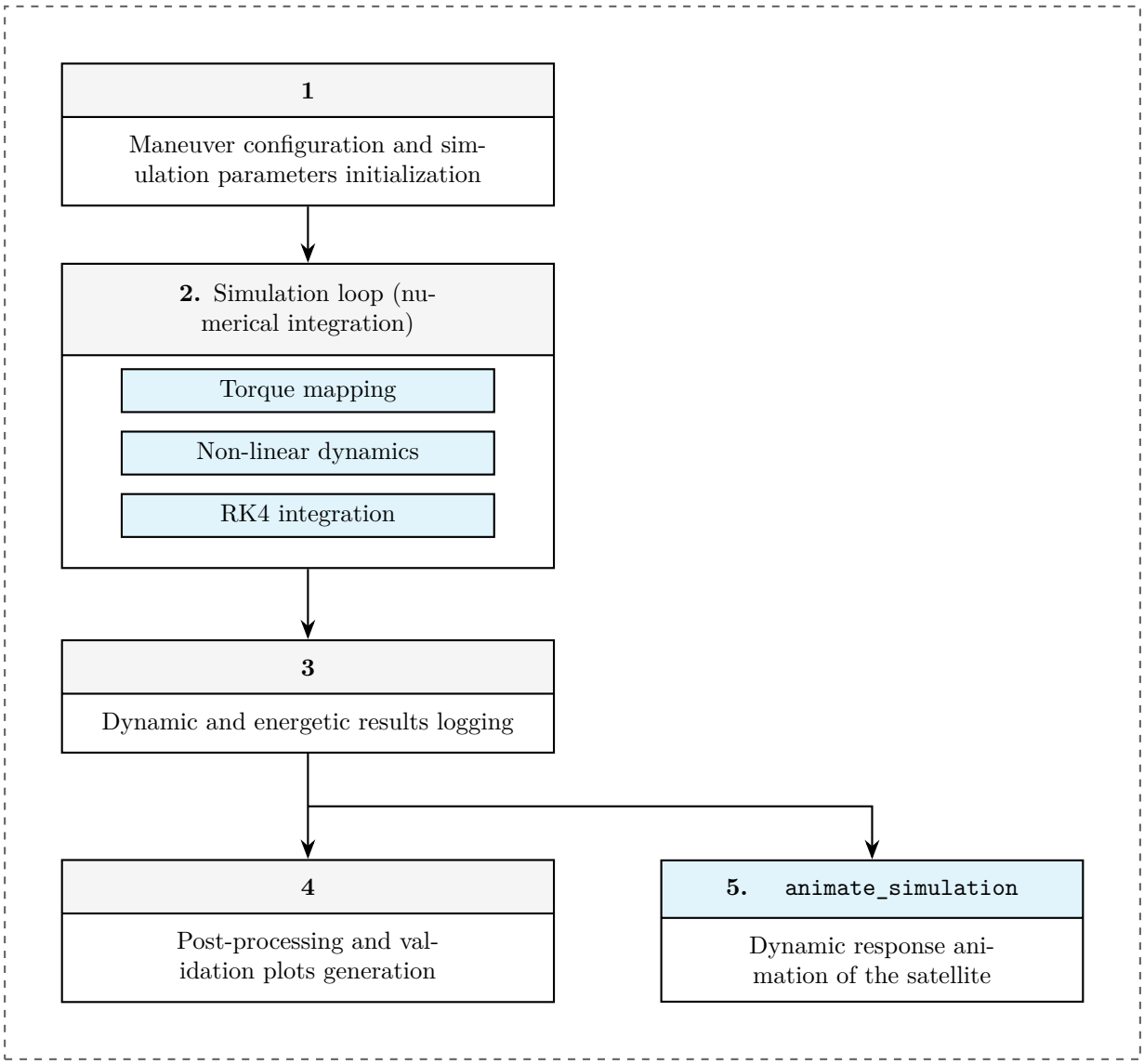

Figure A.3: Logical flowchart of the `N05_OpenLoop_FlexModel.m` script for the dynamic simulation.

2. Simulation Loop (Numerical Integration): At each time instant t_k, the simulator propagates the state $\mathbf{x} \in \mathbb{R}^{36}$ (composed of coordinates $\mathbf{q}$ and velocities $\dot{\mathbf{q}}$) by sequentially calling two fundamental local functions:

   - Torque Mapping (`Torque_Mapping_Local`): Since the dynamic are based on Euler angles, the torque vector $\boldsymbol{\tau}_{cmd}$ applied in the Body Frame is converted into the Lagrangian Generalized Force vector $\mathbf{Q}_{gen}$ by applying the Principle of Virtual Work.
   - RK4 Integration (`RK4_step_flexible` and `non_linear_dynamics`): A wrapper function that implements the fourth-order Runge-Kutta method. Inside, the state derivative is evaluated by calculating the system matrices $(\mathbf{M}, \mathbf{h}, \mathbf{C}, \mathbf{k}_{el})$ at each instant and solving the linear system to compute the accelerations $(\ddot{\mathbf{q}} = \mathbf{M} \setminus \text{RHS})$.

3. Dynamic and Energetic Logging: Parallel to the state advancement, the for-loop records the simulation data for subsequent analysis.

4. Post-Processing and Plot Generation: Once the time cycle is completed, the recorded data is processed to generate validation plots for the model. The script produces numerous figures: plots representing the evolution of the attitude, modal deformations, macro and microscopic energy balances, and a plot representing the Spectrogram (STFT) of the angular accelerations to confirm the frequency shift identified in the previous modal analysis.

5. Call to the `animate_simulation.m` function: Upon user request, the script passes the entire integrated time-state matrix to the tridimensional animation graphical routine. Unlike the modal visualizer, this function executes a realistic simulation of the satellite's dynamic response in Open-Loop.

A.4 Symbolic Derivation of the Rigid Synthesis Model

The script illustrated in this section represents the module dedicated to the derivation of the equations of motion for the rigid model of the satellite, which is used by the controller to generate the torque command $\boldsymbol{\tau}_{cmd}$. From this logical perspective, the flexible dynamics not modeled by the controller are formally treated as exogenous perturbations with respect to this nominal model. This script is executed immediately after `N05_OpenLoop_FlexModel.m` and is fundamental for the subsequent full Closed-Loop simulation performed using the `N08_CL_FlexPlant_Disturbi_BASE.m` script.

The calculation takes place purely in the symbolic algebra domain. The objective is to derive the total inertia matrix of the satellite (Hub and solar panels assumed as rigid and undeformed bodies) evaluated with respect to the center of mass of the Hub, as a function of the panel orientation angle (SADM).

As illustrated in the flowchart in Figure A.4, the logical sequence of operations is structured into the following steps:

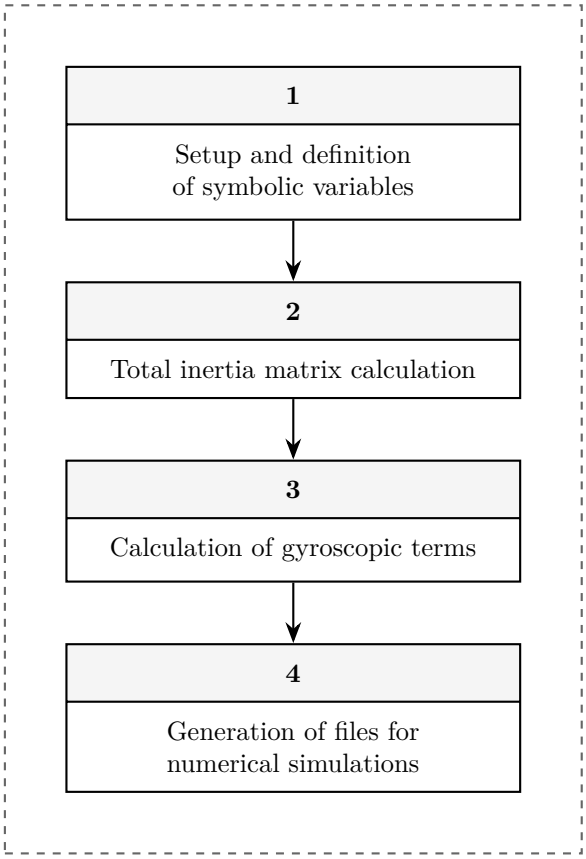

Figure A.4: Logical flowchart of the `N04_Derive_Rigid_Design_Model.m` script for the symbolic generation of the rigid body dynamic model.

1. Setup and Variable Definition: The code initializes the computing environment by defining the mass and geometry parameters of the Hub and the individual panels in symbolic form. Furthermore, the kinematic panel orientation variable α_{sadm} and the rigid body angular velocity vector with respect to the Body Frame, $\boldsymbol{\omega}_{body} = [\omega_x, \omega_y, \omega_z]^T$, are defined.

2. Total Inertia Matrix Calculation: The total inertia $\mathbf{J}_{tot}$ is constructed by assembling the contributions of the individual bodies:

   - The local inertia tensor of each solar panel is first rotated using the elementary rotation matrix associated with the angle α_{sadm}.
   - The Huygens-Steiner (Parallel Axis) Theorem is applied in its matrix formulation to transport the panels' inertia from their respective local centers of mass to the Hub's center of mass.
   - The translated contributions are summed with the Hub's own inertia to obtain the total inertia tensor of the coupled satellite $\mathbf{J}_{tot}(\alpha_{sadm})$.

3. Calculation of Gyroscopic Terms (Coriolis): Once the coupled inertia tensor is obtained, the code analytically derives the non-linear gyroscopic torque vector $\boldsymbol{\tau}_{gyro} = \boldsymbol{\omega}_{body} \times (\mathbf{J}_{tot}\boldsymbol{\omega}_{body})$. Precise knowledge of this term is fundamental for the control architecture, which must provide for its cancellation through the delivery of the commanded torque.

4. Generation of Files for Numerical Simulations: At the end of the algebraic operations, the code utilizes the `matlabFunction` to export the simplified symbolic expressions into two standalone *MATLAB* files: `get_RigidInertia.m` and `get_RigidGyros.m`. The exported functions are structured to accept the same physical parameter array (*raw_params*) used by the flexible model as input, neutralizing unnecessary structural parameters (stiffness and damping) via dummy variables.

A.5 Closed-Loop Non-Linear Simulation

The `N08_CL_FlexPlant_Disturbi_BASE.m` script constitutes the main module for the time-domain validation of the control architecture. This code simulates LASM of the 18-degree-of-freedom flexible non-linear model. As illustrated in the flowchart in Figure A.5, the logical sequence of operations is structured into the following main steps:

1. Maneuver Setup, Disturbances initialization, and tuning of the control law parameters: The code acquires the user-defined target Euler angles as input and performs the conversion into the desired quaternion. Subsequently, it defines the hardware limits (Reduction Factor and T_{max}) and quantifies the maximum magnitude of the expected perturbations (sloshing, external disturbances, uncertainty related to actuator performance deviating from the nominal one). These estimates are aggregated into the upper bound D_{max} used to perform the automatic tuning of the control parameters (e.g., JK_{min}, Λ_{nom}, Φ, η).

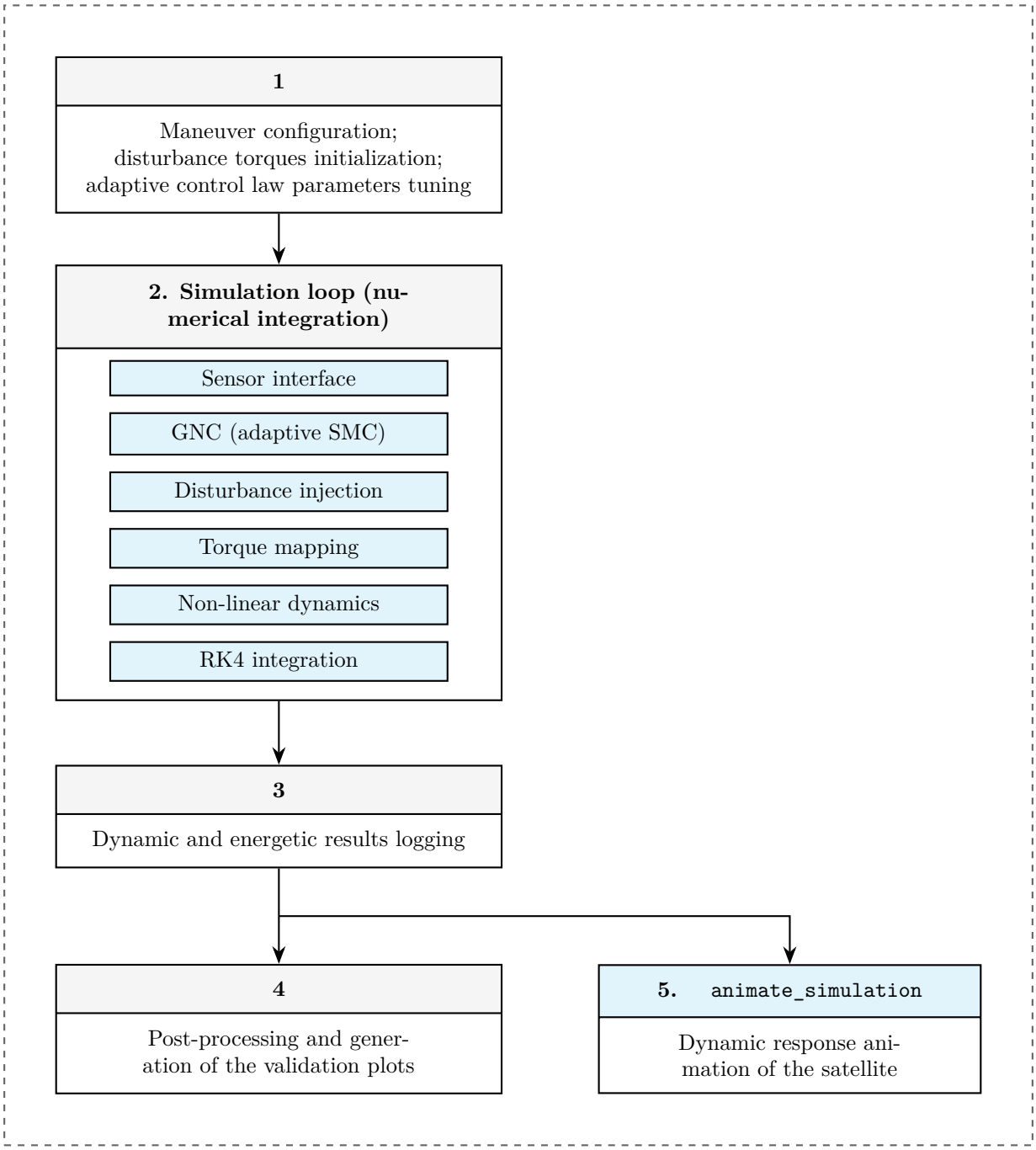

Figure A.5: Logical flowchart of the `N08_CL_FlexPlant_Disturbi_BASE.m` script for the dynamic simulation.

2. Simulation Loop (Time Integration): This constitutes the core of the script. At each time step Δt, the `for` loop sequentially executes the following submodules:

   - Sensor Interface: Calls a local function that extracts the full system state $\mathbf{x}_{full}$. The full state vector is converted into a state vector suitable for estimating the commanded torque, which is fed as input to the ASMC law.
   - GNC (Adaptive Controller): Processes the measured attitude error by calling the ASMC controller function, which returns the ideal commanded torque $\boldsymbol{\tau}_{cmd}$ and updates the adaptive allocation history.
     The reference function is `Smc_Controller_Adaptive_BASE2.m`.
   - Disturbance Injection & Saturation: The commanded torque is multiplied by the actuation uncertainty. Constant environmental disturbances and the harmonic sloshing disturbance are vectorially added to it. The resulting signal is filtered by the physical hardware limit to produce the actually applied torque $\boldsymbol{\tau}_{app}$.
   - Torque Mapping and RK4 Integration: The applied torque is transformed into the generalized force vector $\mathbf{Q}_{gen}$. The coupled dynamics are propagated forward by one time step using a fourth-order Runge-Kutta scheme (`RK4_step_flexible`), which iteratively calls the Lagrangian model generated in Step 1 (A.1).

3. Dynamic and Energetic Logging: Inside the loop, the script saves the time evolution of key variables. In addition to kinematics, sliding surfaces, and control parameters, a rigorous energy balance is performed, paying attention to the amount of elastic potential energy stored in the panels and the energy dissipated through structural damping. Furthermore, the reaction torques exchanged between the panels and the Hub are isolated to evaluate the impact of the CSI.

4. Post-Processing: Once the integration is complete, the code saves the raw data within a structure into a `.mat` file. The script produces a large number of diagnostic plots: from the evolution of Euler angles and quaternions to torque budget monitoring.

5. Call to the `animate_simulation.m` function: Upon user request, the script passes the entire integrated time-state matrix to the tridimensional maneuver animation graphical routine. This function executes a realistic simulation of the dynamic response of the satellite in Closed-Loop.

Appendix B

Complete matrices

B.1 Mass matrix of the nominal case study

As introduced in Chapter 3, the mass matrix of the nominal case study, evaluated in the undeformed configuration ($\mathbf{q} = \mathbf{0}$), can be usefully partitioned into 6×6 sub-matrices that highlight its structure and inertial couplings.

$$\mathbf{M}(\mathbf{0}) = \left[\begin{array}{c|c|c} \mathbf{M}_{hub}^{agg} & \mathbf{M}_{hub,p_1} & \mathbf{M}_{hub,p_2} \\ \hline \mathbf{M}_{hub,p_1}^{T} & \mathbf{M}_{p_1} & \mathbf{0} \\ \hline \mathbf{M}_{hub,p_2}^{T} & \mathbf{0} & \mathbf{M}_{p_2} \end{array}\right] \tag{B.1}$$

The exact numerical values of the individual constituent blocks are reported below.

Aggregated Hub block:

$$\mathbf{M}_{hub}^{agg} = \mathbf{M}_{(1:6,1:6)} = \begin{bmatrix} 163.50 & 0 & 0 & 0 & 0 & 0 \\ 0 & 163.50 & 0 & 0 & 0 & 0 \\ 0 & 0 & 163.50 & 0 & 0 & 0 \\ 0 & 0 & 0 & 189.99 & 0 & 0 \\ 0 & 0 & 0 & 0 & 44.16 & 0 \\ 0 & 0 & 0 & 0 & 0 & 177.90 \end{bmatrix} \tag{B.2}$$

Hub-Panels coupling blocks:

$$\mathbf{M}_{hub,p_1} = \mathbf{M}_{(1:6,7:12)} = \begin{bmatrix} 6.75 & 0 & 0 & 0 & 0 & -15.19 \\ 0 & 6.75 & 0 & 0 & 0 & 0 \\ 0 & 0 & 6.75 & 15.19 & 0 & 0 \\ 0 & 0 & 20.59 & 57.71 & 0 & 0 \\ 0 & 0 & 0 & 0 & 1.27 & 0 \\ -20.59 & 0 & 0 & 0 & 0 & 58.98 \end{bmatrix} \tag{B.3}$$

$$\mathbf{M}_{hub,p_2} = \mathbf{M}_{(1:6,13:18)} = \begin{bmatrix} 6.75 & 0 & 0 & 0 & 0 & 15.19 \\ 0 & 6.75 & 0 & 0 & 0 & 0 \\ 0 & 0 & 6.75 & -15.19 & 0 & 0 \\ 0 & 0 & -20.59 & 57.71 & 0 & 0 \\ 0 & 0 & 0 & 0 & 1.27 & 0 \\ 20.59 & 0 & 0 & 0 & 0 & 58.98 \end{bmatrix} \tag{B.4}$$

Local Panel blocks (P1 and P2):

$$\mathbf{M}_{p_1} = \mathbf{M}_{(7:12,7:12)} = \begin{bmatrix} 6.75 & 0 & 0 & 0 & 0 & -15.19 \\ 0 & 6.75 & 0 & 0 & 0 & 0 \\ 0 & 0 & 6.75 & 15.19 & 0 & 0 \\ 0 & 0 & 15.19 & 45.56 & 0 & 0 \\ 0 & 0 & 0 & 0 & 1.27 & 0 \\ -15.19 & 0 & 0 & 0 & 0 & 46.83 \end{bmatrix} \tag{B.5}$$

$$\mathbf{M}_{p_2} = \mathbf{M}_{(13:18,13:18)} = \begin{bmatrix} 6.75 & 0 & 0 & 0 & 0 & 15.19 \\ 0 & 6.75 & 0 & 0 & 0 & 0 \\ 0 & 0 & 6.75 & -15.19 & 0 & 0 \\ 0 & 0 & -15.19 & 45.56 & 0 & 0 \\ 0 & 0 & 0 & 0 & 1.27 & 0 \\ 15.19 & 0 & 0 & 0 & 0 & 46.83 \end{bmatrix} \tag{B.6}$$

Bibliography

[Gao+21] Shan Gao et al. “Dynamic Sliding Mode Controller with Variable Structure for Fast Satellite Attitude Maneuver”. In: (2021) (cit. on p. 2).

[JyJ05] Liu Jin-yang and Hong Jiazhen. “Geometric nonlinear formulation and discretization method for a rectangular plate undergoing large overall motions”. In: *Mechanics Research Communications* (2005) (cit. on pp. 14, 15).

[KJ17] Rincy Koshy and P R Jayasree. “Comparative study of H-infinity and sliding mode control for a manipulator with oscillatory-base”. In: *2017 International Conference on Circuit ,Power and Computing Technologies (ICCPCT)* (2017) (cit. on p. 2).

[KM20] Behrouz Kharabian and Hossein Mirinejad. “Hybrid Sliding Mode/H-Infinity Control Approach for Uncertain Flexible Manipulators”. In: *IEEE Access* (2020) (cit. on p. 2).

[Lah+23] Yoni Lahana et al. “Comparison of Adaptive Control Laws on a Satellite Attitude Control Benchmark”. In: (2023) (cit. on p. 2).

[LH03] Jin-yang Liu and Jia-zhen Hong. “Geometric stiffening of flexible link system with large overall motion”. In: *Computers Structures* (2003) (cit. on p. 14).

[Nad+19] Reza Nadafi et al. “Super-twisting sliding mode control design based on Lyapunov criteria for attitude tracking control and vibration suppression of a flexible spacecraft”. In: *Measurement and control (London. 1968)* (2019) (cit. on pp. 2, 55, 56).

[Pas+] F Passarin et al. “DEVELOPMENT OF A ROBUST GNC ARCHITECTURE FOR A FLEXIBLE SPINNING SPACECRAFT WITH LONG WIRE BOOMS”. In: () (cit. on p. 2).

[Rod+24] Ricardo Rodrigues et al. “Modeling and analysis of a flexible spinning Euler-Bernoulli beam with centrifugal stiffening and softening: A Linear Fractional Representation approach with application to spinning spacecraft”. In: *arXiv.org* (2024) (cit. on p. 2).